DOI:10.14753/SE.2015.2055

Dendritic Ca^{2+} Spikes and Interneuronal Ripple Oscillations in Fast Spiking Parvalbumin Containing Interneurons during Hippocampal Sharp Wave-Ripple activities

PhD thesis

Balázs Chiovini

Semmelweis University

János Szentágothai Doctoral School of Neurosciences

Functional Neuroscience Program

Supervisor:	Balázs J. Rózsa PhD
Official referees:	Zita Puskár PhD Árpád Mike PhD
Chairman of the final examination board:	László Tretter DSc
Members of the final examination board:	István Ulbert PhD Árpád Dobolyi PhD

Budapest

2015

DOI:10.14753/SE.2015.2055

Table of Contents

DOI:10.14753/SE.2015.2055

DOI:10.14753/SE.2015.2055

List of Abbrevations

2D – two dimension

3D – three dimension

ACSF – artificial cerebrospinal fluid

AMPA – α-amino-3-hydroxy-5-methyl-4-isoxazolepropionic acid

AO – acuosto optical

AP – Action potential

BC – basket cell

CA – cornu ammonis

Ca^{2+} – calcium ion

CCK – cholecystokinin

CNQX – 6-cyano-2,3-dihydroxy-7-nitro-quinoxaline

DL-AP5 – D,L-2-amino-5-phosphonopentanoic acid

DNI-Glu•TFA – dinitro-indolin-glutamate trifluor acetate

EC – entorhinal cortex

eGFP – enhanced Green Fluorescence Protein

EPSC – excitatory postsynaptic current

EPSP – excitatory postsynaptic potential

FS-PV IN – fast spiking parvalbumin containing interneuron

GD – gyrus dentatus

IPSC – inhibitory postsynaptic current

IPSP – inhibitory postsynaptic potential

K^+ – potassium ion

LFP – local field potential

LTD – long-term depression

LTP – long-term potentiation

LUT – look-up table

MNI-Glu – mono-nitro-indolin-glutamate

NA – numeric aperture

Na^+ – sodium ion

NMDA – N-methyl-D-aspartate

O-LM cell – oriens-lacunosum molecular cell

PC – pyramidal neuron

PV – parvalbumin

RC – roller coaster

R_{in} – input resistance

SPW – Sharp wave

SPW-R – sharp wave-ripple comlex

TTX – tetrodotoxin

VGCC – voltage-gated calcium channel

τ – membrane time constant

DOI:10.14753/SE.2015.2055

“This wonderful harmony and beauty, as I see this created world, awakens me to the thought, that this evidently could not have developed by itself or by pure chance, but behind this there must be an idea of a Creator, there must be a Creator.”

János Szentágothai

DOI:10.14753/SE.2015.2055

Foreword

János Szentágothai, in the course of his life focused on the operation of physiological systems. He always said that the most beautiful part of the structure was functioning. He taught functional anatomy instead of morphology as did his predecessors and his colleagues. To understand the machinery of the brain, it is not enough to know the morphological background of the cells. Networks formed by neurons do not only have a structure but dynamically changing functions as well, which are determined mainly by the spatio-temporal behavioural states of living entities. The spatio-temporal changes alter the functional phenotype of cells or networks. Although science has supported descriptive, morphological paradigms, modern conceptions clearly advocate functionality again. After the experimental *in vitro* results neuroscience focuses on these details re-interpreted in the "real", dynamically changing environment which is currently in progress. Our main aim is to study the increasingly more realistic, complex and functioning brain.

One of the crucial questions of neuronscience is that how different neuron types can act in the brain during complex activities. On one hand, *in vivo* measurements would give great possibilities to answer these questions but some important cases, such as how dendritic integration works in thin apical dendrites of the hippocampal cells during physiologically relevant spontaneous activities, can not be resolved by *in vivo* measurements because the currently available imaging technologies can not compensate motion artefacts at such a high spatial resolution. On the other hand, active and regenerative calcium signals in long, apical dendritic segments can be challenging to study in 2 dimension (2D) imaging techniques either *in vitro* or *in vivo*. Here I introduce a new type of experiments where almost the whole dendritic arbour can be measured simultaneously in 3 dimension (3D) in real time with a novel 3D random access two-photon microscope. Moreover, I can reproduce these signals with a novel glutamate uncaging material for the better understanding of the dendritic calcium signal integration and for pharmacological measurements as well. Following Szentágothai's way, I focus on the functions of anatomically well-known neuronal machineries.

DOI:10.14753/SE.2015.2055

1. Introduction to the Literature

How memory is formed and stored in the complex nervous system? Santiago Ramon y Cajal had already suggested a mechanism of learning which lacks formation of new neuronal cells (Cajal, 1909). According to his doctrine, the information flows from axons to dendrites in the network (Neuronal Doctrine). Later, his conceptions were confirmed and extended by Donald Hebb, who claimed that the cells may grow new connections while they undergo metabolic changes that enhance their ability to communicate (Hebb, 1949). To continue this paradigm, Terje Lømo described the mechanism of long term potentiation (LTP) which expanded the scientific field of learning and memory process (Lømo, 1966). Thanks to patch-calmp techniques, multi cell recordings, two-photon microscopy, different uncaging materials and optogenetics, we have a lot of detailed information about the component of memory and learning. Nowadays LTP and memory are studied in neuronal network, single cell, compartment and ion-channel level as well. By now we know that the hippocampus is an important area of the brain where the information is encoded, stored and retrieved by periodic network activity.

Sharp wave-ripple oscillations (SPW-Rs) were discovered by Cornelius Vanderwolf in 1969. This population event is the first network activity which is present in the developing hippocampus and showing their importance of SPW-Rs (Buzsáki, 2006). John O'Keefe investigated SPW-Rs in relation to the spatial memory of rats (O'Keefe and Dostrovsky, 1971). Later, György Buzsáki formed a theory of the importance of SPW-R complexes in the functioning brain in different behavioral states of the animal (Buzsaki, 1989). Buzsáki and his colleagues characterized and pointed out the significance of the SPW-Rs in memory formation and consolidation (Girardeau et al., 2009, Ego-Stengel and Wilson, 2010). In the past year it has been shown that one of the most important cell types which plays a crucial role in the generation and synchronization of SPW-R oscillations is the fast spiking parvalbumin containing interneuron (FS-PV IN) (Csicsvari et al., 2000, Lapray et al., 2012, Schlingloff et al., 2014, Stark et al., 2014). However, until now it was not possible to examine the dendritic signal processing in the long and thin dendrites of FS-PV INs during SPW-R oscillations. The question is how these neurons can organize such a large inputs arriving

during SPW-Rs to the extended dendritic arbour and form output of the cells remains elusive.

1.1. Functional and anatomical properties of the hippocampus

At the beginning of my thesis, the main paradigms such as anatomical properties of the hippocampus with neuronal circuits and their local and global projections will be reviewed. In addition I will mention the different oscillations of the hippocampus such as theta, gamma, and especially SPW-R oscillations. After the resume of the parameters of hippocampal macroscopic structures and rhythms, I discuss the functional properties of different interneurons during hippocampal oscillations. In my thesis I always refer to basket cells and axo-axonic cells as FS-PV INs located mainly in the pyramidal layer of the hippocampus.

The hippocampus is located under the cerebral cortex, next to the medial temporal lobe (Andersen, 2006) one in both sides of the brain. As a member of the limbic system it is responsible for emotion, long term memory, behaviour and motivation (Kandel, 1991). These functional properties are due to the extended connectivity of limbic system which contains the following brain areas beside the hippocampus: olfactory bulbs, amygdala, anterior thalamic nuclei, fornix, columns of fornix, mammaliar body, septum pellucidum, habenular commisure, cingulated gyrus, parahippocampal gyrus, limbic cortex and limbic midbrain areas. The hippocampus is a part of the hippocampal formation besides the entorhinal cortex (EC) and subiculum (pre-and parasubiculum) (Andersen, 2006). The two main parts of the hippocampus are the Ammon's Horn or Cornus Ammonis (CA) and the dentate gyrus (DG) (Andersen, 2006). Two important concepts can be linked to hippocampal functions. The cognitive or mental map is the first, where the activity of certain neurons and neuronal assemblies are strongly linked with certain location of the behaving animal. These neurons are called place cells (O'Keefe J, 1978). The second concept is the encoding of memory. During memory consolidation, short term memory converts to long term memory (Buzsaki, 1989). Without hippocampus new memory or information can not be formed and the memory procession is stopped (Mahut et al., 1982).

The **DG** can be easily recognised in rodents as a 'C' curved structure full with densly lined-up granule cells. The DG has three layers: molecular (external, middle and

inner), granular and polymorphic. The granule cells as principal, excitatory neurons are settled in the granular layer of the DG and they project to mossy cells, interneurons and to pyramidal cells. One of the main inputs of the DG is the perforant path where axons arrive from the layer II of EC. The information flows further via the mossy fiber through the CA3 subfield of the hippocampus.

The **hipocampal CA** region is a banana-shaped (Andersen, 2006) structure which can be easily recognised with highly dense neuronal cell bodies. The principal cell type here is also excitatory, namely the pyramidal neurons. It has four sub-divisions from CA1 to CA4. The CA4 is embedded in the DG, while the CA1 is located at the other end of the "banana". The CA region has lamellar structure with four different main layers, namely: *stratum oriens, stratum pyramidale, stratum radiatum and stratum lacunosum-moleculare*. The large numbers of cells' somata are settled in the stratum pyramidale. Many interneurons' somata, including axo-axonic-, basket-, bistratified-, ivy- and radial trilaminar cells are also located here. The apical dendrites are sorted parallel in the stratum radiatum while the basal dendrites expand into the stratum oriens. Both places accept commissural projections. In the stratum oriens mostly interneurons and glia cells can be found. The efferent inputs arrive here from the amygdala while the stratum-lacunosum moleculare accept projections from EC and thalamus. The CA3 region has a lucidum layer under the stratum pyramidale, where mossy fibers terminate from the DG. The alveus, which is a sheave of axons of the pyramidal neurons, cover the whole hippocampal structure and pass toward the fimbria or fornix, one of the main output of the hippocampus. The axons of CA3 pyramidal neurons are arranged in bundles and form the Schaffer collateral into stratum radiatum of CA1 sub-region. Schaffer collatarel and perforant path can arrive also in stratum lacunosum-moleculare and innervate the local interneurons and distal apical dendritic segments (Andersen, 2006).

Between the CA1 and EC regions, **subiculum** sub-region is formed as the most inferior part of the hippocampal formation. The cells are sparsely settled here and get information from the CA1 and EC layer III. The projections headed to EC, amygdala, nucleus accumbens, lateral hypothalamus, mammaliar nuclei, cortex or sensory cortex (Andersen, 2006).

The **EC** is located in the medial temporal lobe close to the hippocampal CA1 region in the parahippocampal gyrus, thus it is anatomically strongly connected to the hippocampus. The cells in the EC seem more diffuse than the hippocampal neurons, distinguished layers from I to V (Andersen, 2006).

1.2. Hippocampal circuits

Population activity of neuronal cells carries the information through excitatory pathways between the different brain areas. The hippocampus has two main loops. The long or so-called trisynaptic loop follows the EC layer II, granule cells of the dentate gyrus, CA3, CA1 and subiculum containig axis of the hippocampus with multiple short cuts and superimposed loops. In details: the inputs arriving from the EC layer II/IV spiny stellate cells through the perforant path reach the DG granule cells, which then innervate the CA3 pyramidal cells, which through the Schaffer collaterals innervate the CA1 and CA3 stratum radiatum. The short excitatory loop is formed between the EC layer III and CA1 directly which is then projected back to the EC layer V (**Figure 1A**) (Buzsaki and Diba, 2010). These excitatory loops are gently organized by inhibitory neuronal activities which are not organized in a loop like formation (Freund and Buzsaki, 1996, Traub and Bibbig, 2000, Schmitz et al., 2001, Traub et al., 2012). These pathways, especially the trisynaptic loop, provide bidirection information transfer between the hippocampus and the neocortex. Along these loops the main hippocampal oscillations are formed, namely the theta (4-12 Hz), the gamma (30-80 Hz) and the SPW (0.5-1.5Hz) with superimposed ripple (140-200 Hz) activities. Depending on the behavioural state of the animal, these oscillations form a well defined flow direction on the cortico-hippocampal axis (Buzsaki and Diba, 2010). Theta and gamma activities appear when the animal moves, senses and acts. This is the “on-line” mode of the animal. In this case the information flows in a cortico-hippocampal direction. In contrast, during consummatory behaviour and slow-wave sleep these oscillations disappear and are replaced by SPW-R activites. These hippocampal patterns are responsible for the encoding, storage and retrieval of memory (Squire et al., 2004). During the mechanism of encoding, the animal receives information from the surrounding environment, processes and combines the received information. These activites are supported by the above mentioned projections and loops. Thus SPW-Rs do

DOI:10.14753/SE.2015.2055

not only send information from the hippocampus to the neocortex but also receive inputs from the neocortex as well and affect the subiculum, the parasubiculum and the dentate gyrus. This sensitive dialogue forms the short term memory into long term memory transition with specific steps. But what are the specific properties of the SPW-R activites and how can they be generated in the hippocampus?

1.3. Properties of SPW-R complexes

SPW and superimposed ripples are associated with slow wave sleep, immobility and consummatory behaviour (Buzsaki, 1989, Wilson and McNaughton, 1994). They appear when the impact of subcortical inputs into the hippocampus decreases and the activation of the CA3 pyramidal cell population is activated.

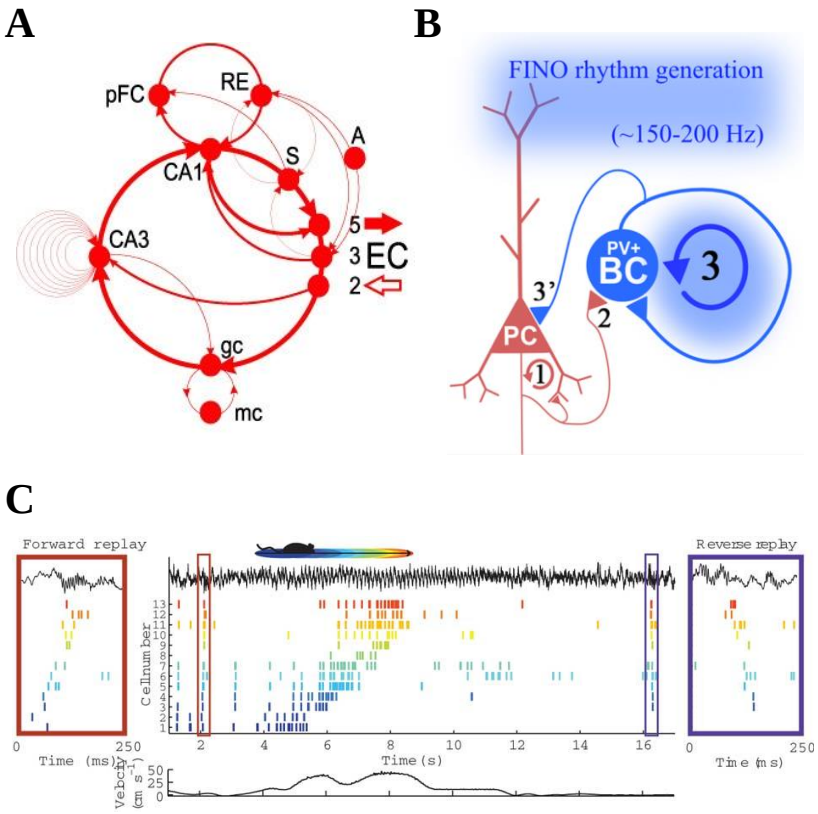

Figure 1. Structural and functional properties of the hippocampus related to the SPW-R activities. A: Schematic drawing of the hippocampal projections along the hippocampal-entorhinal cortex representing the long- and the short excitatory loop. *Abbreviations: mc: mossy*

cells of the hilus; A: amygdala; RE: nucleus reuniens of thalamus; pFC: prefrontal, anterior cingulate cortex (Buzsaki and Diba, 2010). **B:** Schematic representation of the generation of the ripple oscillations (Schlingloff et al., 2014). **C:** During SPW-Rs the place cells replay both forward and reverse the sequences that the animal senses during behaviour. Spikes of 13 neurons during running (middle). Before traversal of the environment the sequence replay forward and the reverse is represented after. The animal velocitiy during running is represented below, CA1 local field is represented on the top (Source: Diba and Buzsaki, 2007).

In contrast to the theta, SPW activity is a unique self organized endogenous rhythm of the hippocampus. It is characterized by a high amplitude and relatively slow oscillation (0.5-1.5Hz) (Buzsaki and Diba, 2010). A SPW event is the most synchronous rhythm of the hippocampus, because during immobility, 50.000-100.000 neurons discharge in the CA3-CA1-subicular-EC axis of the hippocampus that may cause an enhanced synaptic plasticity in this whole region (Csicsvari et al., 1999). Though the information flows in hippocampal-neocortical direction (Isomura et al., 2006) the cortical input highly affects the SPWs (Sirota et al., 2003, Buzsáki, 2006). Spike transmission throughout the CA3-CA1-subicular-EC axis is extremely fast, about 15-20 ms interval.

A SPW event can propagate along the hippocampal CA regions from CA3 to CA1 and activates locally the different pyramidal cell - inhibitory cell assemblies. The SPW's flow is led by the cooperation of excitatory and inhibitory neuronal networks (Buzsáki, 2006).

The CA3 and CA1 SPWs are associated by fast gamma (90-140Hz) (Sullivan et al., 2011) or ripple activities at 140-200Hz frequencies (O'Keefe J, 1978, Buzsaki et al., 1992) which are activated locally, led by the SPWs and synchronized by the local interneuronal sub-networks (Buzsáki, 2006, Schlingloff et al., 2014, Stark et al., 2014). The frequency of the ripple activities is well-correlated with the amplitude of the SPW events (Sullivan et al., 2011, Stark et al., 2014) which depends on the number of the activated cells.

1.3.1. The generation of SPW-R complexes

The initiation of the SPW-R complexes is driven by an interaction between hippocampal excitatory pyramidal cells and inhibitory neurons, especially local

perisomatic region-targeting interneurons. The strong recurrent network of CA3 pyramidal neurons enables this region to initiate SPW-Rs (Buzsaki and Chrobak, 1995, Csicsvari et al., 2000) and excite the CA1 stratum radiatum dendritic area via Schaffer collateral (Csicsvari et al., 2000, Ellender et al., 2010) and cause negative wave in the LFP, while in the somatic layer an outward current is present (Schonberger et al., 2014). Thus, the CA3 subnetwork of the hippocampus has a special role in the initiation of SPW-R complexes via the activation of pyramidal neuron populations. The population activity of the pyramidal neurons builts up around 50 ms before SPW-R peak from a baseline level of excitatory activity (Csicsvari et al., 2000, de la Prida et al., 2006, Schlingloff et al., 2014). Five to ten percent of the pyramidal cell population is activated during a single SPW-R event, but different pyramidal cell-interneuron assemblies are activated through the different SPW-R events (Buzsáki, 2006). Between two SPW-R events refractory mechanisms are formed while SPW-R could not restart within a 200-300 ms long time interval. These refractory mechanisms may play a role not only in the prevention of the next SPW-R event in a defined time interval but in the termination of the single SPW-R event as well (Schlingloff et al., 2014). Besides refractory mechanisms, inhibitory subnetwork activities are also important in the termination of the SPW-R events. The stochastic CA3 tonic activity of pyramidal cell's population triggers population activity in CA1 region at multiple locations (Buzsaki et al., 1992, Nadasdy et al., 1999, Sullivan et al., 2011, Tukker et al., 2013) via the Schaffer-collaterals. The information flow is organized by interneuronal cell assemblies (Buzsáki, 2006). The different hippocampal sub-regions have their own rhythm generating properties, but the ripple frequency range and its amplitudes are altered. In hippocampal mini slice preparation, which contains the CA1 and the CA3 regions of the hippocampus respectively, higher amplitude and slower frequency are shown of the SPW events in CA1 than in CA3 (Maier et al., 2003). This indicates that the whole hippocampal region has a kind of pace-maker ability with a region specific nature. Though the CA1 region has an own SPW-R trigger ability the CA3 activity basically defines the activity pattern of CA1. The propagation of SPW-Rs is maintained by specific neuronal assemblies with cell to cell precision (Both et al., 2008). Moreover the information transmission has layer specifity. The CA1 superficial neurons were excited

earlier and at higher probability than deep layer neurons, and basket cells get stronger excitation by superficial pyramidal neurons (Lee et al., 2014, Stark et al., 2014).

1.3.2. Models for the generation of fast ripple oscillations

In the last decade several excellent studies were published about the generation of fast ripples during the SPW events proposing several models underlying their cellular and network mechanisms.

Although early studies support the idea that burst firing of the pyramidal neurons are responsible alone for ripple generation (de la Prida et al., 2006, Foffani et al., 2007, Jefferys et al., 2012) via axonal gap junctions (Draguhn et al., 1998), two recent studies indicate that local perisomatic inhibitory interneurons are excited by the tonic activity of the pyramidal neurons which eventually causes synchronous inhibitory drive by reciprocal inhibition and, surprisingly, the contribution of gap junctional connections might be negligable (Schlingloff et al., 2014, Stark et al., 2014) in the generation of a ripple. The gap junction containing axo-axonal connections may give a possibility for the spikes to propagate antidromically to the soma (Traub and Bibbig, 2000, Schmitz et al., 2001, Traub et al., 2012) even during ripple activities *in vitro* (Papatheodoropoulos, 2008, Bahner et al., 2011) or *in vivo* (Ylinen et al., 1995), but a recent drug free *in vivo* study showed that during ripple activities spike propagation is rather ortodromical than antidromical (English et al., 2014). On the whole, the concrete roles of the gap junction effects on the ripple generation and synchrionization remain elusive. Other models claim that ripple generations are realized through the interactions between perisomatic region-targeting interneurons. These neurons are activated by SPW-associated depolarizations and evoke co-oscillations at ripple frequency range which periodically modulate the firing activity of pyramidal neurons (Buzsaki et al., 1992, Whittington et al., 1995, Ylinen et al., 1995, Traub et al., 1996, Brunel and Hakim, 1999, Geisler et al., 2005, Racz et al., 2009, Taxidis et al., 2012), or maybe the ripples are generated by short-lived interactions between interneurons and pyramidal cells (Buzsaki et al., 1992, Ylinen et al., 1995, Brunel and Hakim, 1999, Klausberger et al., 2003, Memmesheimer, 2010). In the Buzsaki lab it has been demonstrated in behaving and anesthetized animals that the activity of the pyramidal neurons is a necessary requirement for ripple generation and that inhibitory interactions play a critical role in rhythm generation and

in the synchronization of independent ripple oscillators (Stark et al., 2014). This *in vivo* study revealed that activity of a dozen pyramidal neurons is necessary for ripple generations, moreover fast GABAa receptor-mediated inhibition is a prerequisite for the generation of high frequency oscillations. The ripple timing can be set by the interaction between PV INs (Stark et al., 2014). The strong tonic excitatory drive evokes high frequency firing in PV basket cells and their reciprocal inhibitory activity is essential for coherence (Schlingloff et al., 2014). There is no cycle by cycle reciprocal inhibition between pyramidal cells and PV basket cells, rather reciprocal inhibition between PV basket cells which then entrain the local pyramidal cell population activities (Figure 1B). This phasic inhibition promotes (rather than inhibits) the otherwise tonically firing pyramidal cells (Schlingloff et al., 2014). Besides basket cells, axo-axonic cells could have an important role via selecting the subpopulation of pyramidal cells that may start firing at the beginning of the SPW-Rs (Ellender et al., 2010). While PV basket cells are active at the peak of the SPW-Rs, axo-axonic cells fire in the first half of the ripple period (Klausberger et al., 2003, Hajos et al., 2013).

The potential role of the synchronized CA1 ripples is to amplify the output messages of the hippocampus. They synchronize and coordinate local pyramidal cell activity, select the dominant and suppress the competing neuronal assemblies and propel forward to the cortical and subcortical structures (Logothetis et al., 2012). The LFP ripple cycles reflect the sequential activity of the neurons which is influenced during the explorative experiences (Buzsaki, 1989, Wilson and McNaughton, 1994). During SPWs the neuronal sequence is often similar to place cell sequences observed during exploration, which indicates that during SPWs the memory encoding is replaying the sequence that the animal senses during explorations (**Figure 1C**) (Diba and Buzsaki, 2007). Selective elimination of SPW-R activities highly affects memory (Girardeau et al., 2009, Jadhav et al., 2012).

1.4. Interneuronal subtypes and their activities during hippocampal rhythms

Five to ten percent of the cell population in the hippocampus is interneuron. Besides neurotransmitter gamma-aminobutyric acid (GABA), which causes inhibitory postsynaptic potentials in their target neurons (by inward chloride ions), the major

difference between pyramidal cells and inhibitory interneurons is that the axonal arbour remains the region where cells are settled (exceptions: long range projection interneurons). Though interneurons regulate the neighbouring territories in a relatively short distance, they receive their inputs not only locally but from extra-hippocampal areas as well. Feed-forward inhibition is generated when the projection excites the interneurons from neighbouring regions. The other type of excitation which activates the interneurons locally causes feed-back inhibition (Freund and Katona, 2007). The anatomical and physiological properties of interneurons including the feed-back and feed-forward inhibition result in the special activity control and coordination of neuronal cell assemblies. Activities of interneurons play a role in the generation of rhythmic network events of neuronal ensemble, control of excitatory inputs and synchronization of neuronal population discharge.

1.4.1. Classifications of hippocampal interneurons

At least three types of pyramidal cells and 21 types of interneurons are present in the CA1 hippocampal area (Klausberger and Somogyi, 2008). Interneurons show wide range diversitiy in functional and phenotypic appearance. The following paragraphs collect the different classification, in many examples the different classes will be merged.

First, it is a good approach to divide the interneuronal subtypes by physiological characteristics: e.g. action potential characteristics, firing pattern, short and long term synaptic plasticity. According to the Petilla convention, five major groups of interneuron's can be distinguished (without detailed description)*: regular spiking non-pyramidal neurons, fast spiking interneurons, burst-spiking non pyramidal neurons, irregular-spiking interneurons and delayed-spiking interneurons (Ascoli et al., 2008).*

Second, in many cases interneurons can classificate morphologically: including selective termination of the axons, number of laminar distributions of the dendrite, co-transmitter content, receptor expression pattern (Freund and Buzsaki, 1996). The perisomatic region innervating inhibitory neurons (basket and axo-axonic cells) have a primary effect on the somata or axon initial segments of their targets (Somogyi et al.,

1983, Buhl et al., 1994) and control the output function of the cells, while the dendritic inhibitory cell (Hartwich et al., 2009) family can control the plasticity of the postsynaptic area (bistratified- and oriens-lacunosum molecular interneuron (Miles et al., 1996)). In addition, the different types of neurons can express different types of voltage-dependent ion channels and different molecular composition of their synapses.

Third, with the molecular markers such as neuropeptides (somatostatin, cholecystokinin, vasoactive intestinal peptide and neuropeptide-Y) and Ca^{2+}-binding proteins (parvalbumin, calretinin and calbindin) we can selectively define the cell type by immunohistochemical techniques.

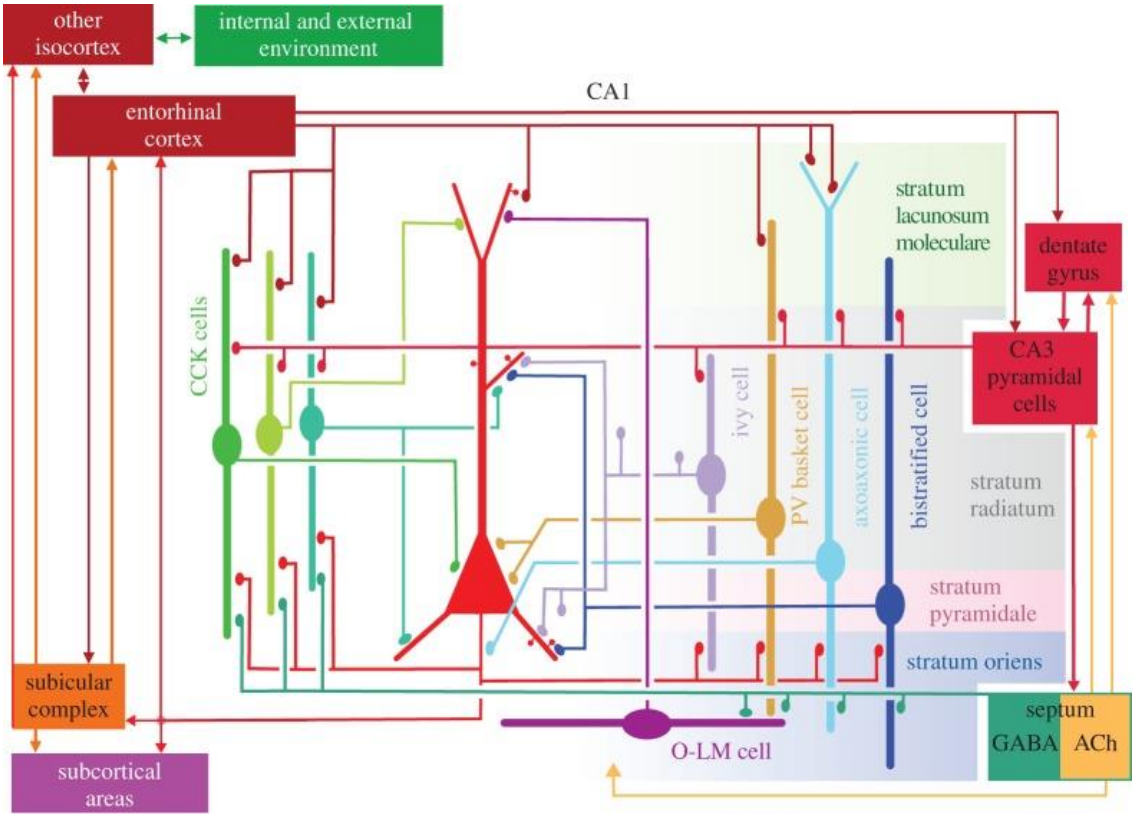

Figure 2. Spatial interaction between pyramidal neurons and several classes of interneurons in the hippocampal CA1 region, summerize the main synaptic connections of the cells. The same somatic and dendritic domains receive differentially timed input from several types of GABAergic interneuron (Somogyi et al., 2014).

The hippocampal CA1 region represent three types of CCK-containing cells (basket cell, perforant path-associated cell and Schaffer collateral-associated cell), ivy cells and PV-positive basket, axo-axonic, bistratified and O-LM interneurons. **Figure 2.** shows the local projections, afferents and efferents of these neurons in the hippocamapal CA1 region.

1.4.2. Activity patterns of the different interneurons during hippocampal oscillations

Several *in vivo* and *in vitro* studies paid attention to understanding the functional properties of the pyramidal cells and different interneurons during SPW-Rs, theta and gamma oscillations and define specific firing characteristics of identified neurons (summarizes: (Somogyi et al., 2014). Different domains of the pyramidal neurons are innervated by different interneuronal subtypes (**Figure 2**). During theta and ripple activities cells fire with distinct patterns which are coupled to field oscillations. The different temporal dynamics could come from interneurons expressing CCK or PV that innervate parallel the soma and dendrite of principal cells.

During theta activity recorded in CA1 pyramidal layer, the firing rate of pyramidal neurons is the lowest at the peak of the theta cycle, while axo-axonic cells, CCK- and PV-positive basket cells fire the most. Basket, ivy and O-LM cells show theta phase coupling and reach the maximal probability of their firing at the trough of a theta cycle. During gamma oscillations bistratified and ivy cells show the highest firing frequencies and their spike showed strong phase coupling in CA3 area. The firing probability of PV-positive cells and bistratified interneurons is the maximal during ripple oscillations such as pyramidal cell discharge, whereas the axo-axonic cells fire only the first half of the ripple activities (**Figure 3.**). O-LM cells could be inhibited or activated during ripples (Varga et al., 2012).

DOI:10.14753/SE.2015.2055

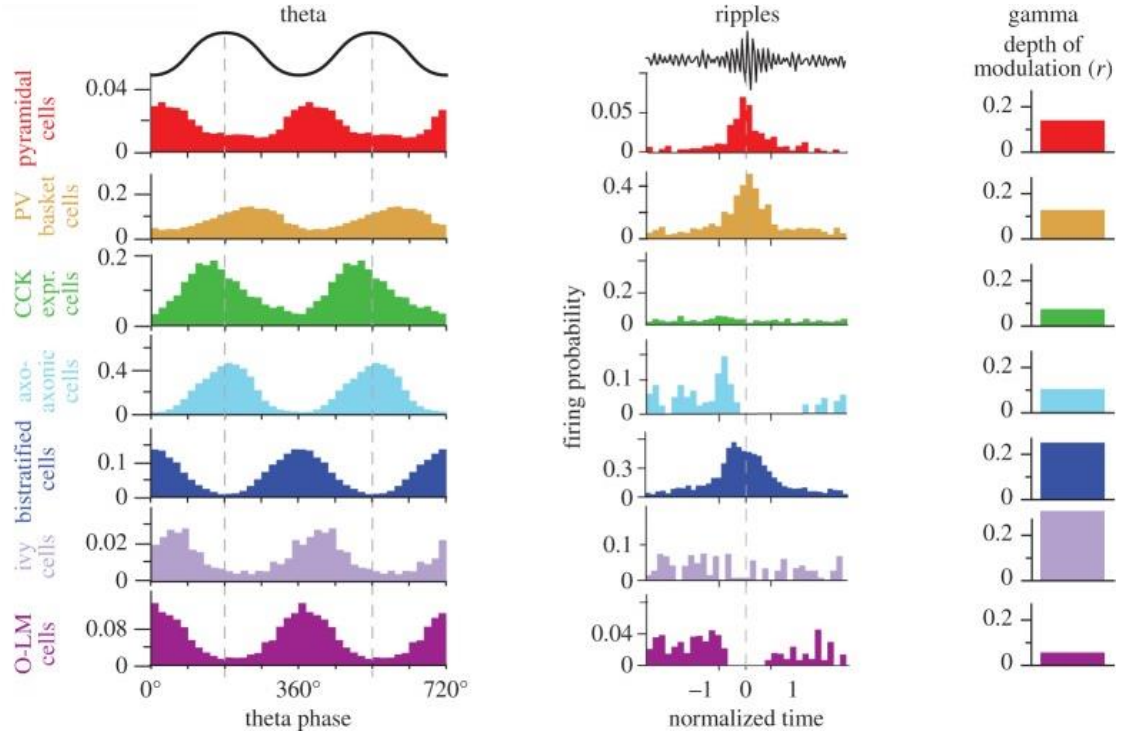

Figure 3. Main types of interneurons and their activities during hippocampal network oscillations. Their spike timing is coupled to field gamma, ripples and theta oscillations at different degrees (Somogyi et al., 2014).

1.5. Role of fast spiking PV-positive interneurons in SPW-R activities

As I have already mentioned, the role of FS-PV INs in SPW-Rs generation is extremely crucial. Early studies showed that the firing activity of the hippocampal FS-PV INs is strongly phase-locked to the peak of SPW-R oscillations (Klausberger et al., 2003, Bahner et al., 2011). To understand how these interneurons can integrate and convey the information even at such a high frequency range as ripple oscillations, I have to concern the basic properties of these types of neurons.

FS-PV INs are a subclass of interneurons which could be well-identified by distinct electrophysiological properties and molecular markers. These interneurons selectively express the Ca^{2+} binding protein, called parvalbumin (PV) which can be found in every compartment of the cell (Meyer et al., 2002). The extended thin, aspiny dendritic and axonal arbour (**Figure 4A**), the number of synapses and boutons, the ion channel distribution and types help to facilitate the generation of fast excitatory

postsynaptic potentials (EPSPs) on PV INs (Geiger et al., 1997). These features of FS-PV INs assist the better and faster information flow from the input of the cell to its output, to axonal boutons, which are equipped with machinery for fast transmitter release. These parameters support the fast signalling and signal transmission. These details are well-summarized in a recently published review by Peter Jonas and his colleagues (Hu et al., 2014).

1.5.1. Basic properties of hippocampal FS-PV INs

In the stratum pyramidale of CA1three types of PV-containing interneurons exist: PV basket cells, axo-axonic cells and bistratified cells. The somata of the O-LM cells are located in the stratum oriens, thus these neurons can be selectively separated often from the other three neuron types. PV as a neurochemical 'marker' is suitable for the post hoc identification of these cells (Celio, 1986, Eggermann and Jonas, 2012). Furtheremore the PV gene can be used for selective genetical targeting of these cells i.e. by enhanced green fluorescent protein (GFP) (Meyer et al., 2002) or viral vectors (Stark et al., 2014). The population of PV-containing neurons is about 2.6% of the total neuron population (24% within the interneuronal population) (Bezaire and Soltesz, 2013). PV interneurons innervate the postsynaptic cells mainly in their perisomatic region, i.e. at their somata and proximal dendrites (basket cells) or axons, axon initial segments (axo-axonic cells or chandelier cells) (Freund and Katona, 2007). The bistratified neurons innervate the proximal dendritic compartments of the pyramidal neurons. This means that the PV basket and axo-axonic cells regulate the site of the neurons where the action potentials (APs) are generated, thus adding a great impact directly to the output of the principal cells, whereas bistratified interneurons mostly have an effect on synaptic plasticity, LTP and LTD. The synaptic domain of the FS-PV INs contains P/Q type Ca^{2+} channels in order to shorten the synaptic delay and increase the temporal precision of transmitter release (Hefft and Jonas, 2005, Zaitsev et al., 2007).

In the stratum pyramidale of the CA regions these PV interneurons have similar electrophysilogical parameters (**Figure 4B**). According to Pettilla terminology (Ascoli et al., 2008), they are all fast spiking interneurons. The passive intrinsic membrane properties measured in a whole-cell current-clamp configuration show that the resting membrane potential is between -65.1 and -69.2 mV. Their input resistance is

between 31 to 73 MΩ, while their membrane time constant is between 7.7 to 18.6 ms. The action potential (AP) half width is 364 to 527 µs; somatically injected current can evoke a maximal firing rate at 120Hz to 300 Hz, showing a low accommodation in firing (Buhl et al., 1994, Buhl et al., 1996, Lamsa et al., 2007, Ascoli et al., 2008). These parameters defines their fast spiking phenotype.

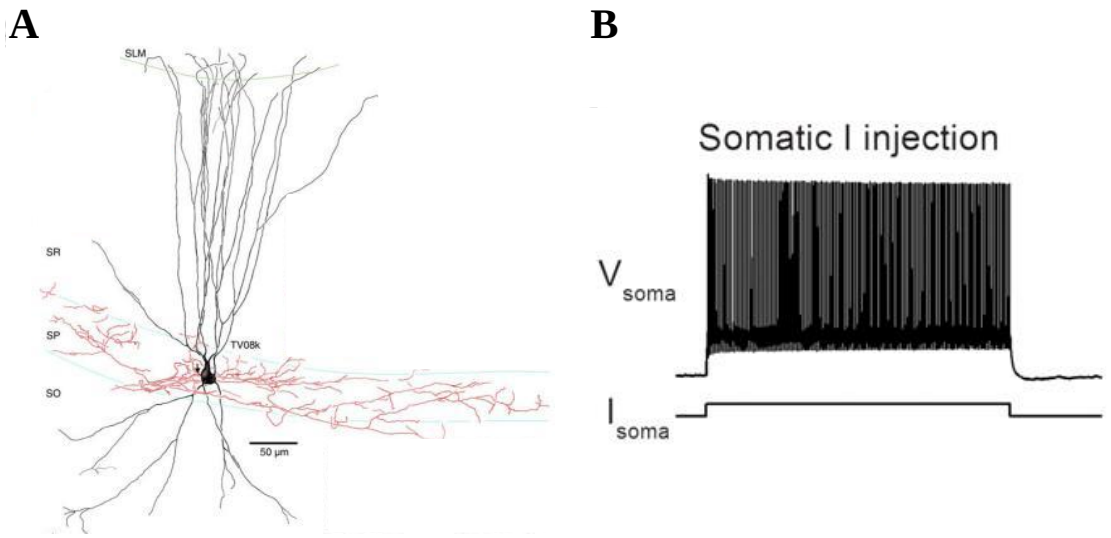

Figure 4. Morphological and functional properties of the FS-PV INs. A: Reconstruction of a PV-containing basket cell in the CA1 hippocampal region. Soma and dendrites are shown in black whereas axon in red. SR: stratum radiatum; SP: stratum pyramidale; SO: stratum oriens. (Soruce: Lapray et al., 2012). **B:** Fast spiking AP phenotype. Long somatic current pulse evoked a high-frequency train of AP in the recorded neuron (Hu et al., 2010).

1.5.2. Relevant functions of FS-PV INs

PV-expressing interneurons play a role in feed-forward and feed-back inhibition. Feed-forward inhibition of PV neurons is triggered by excitatory inputs which arrive from the surrounding areas. Feed-forward inhibition narrows the temporal summation of excitatory postsynaptic potentials (EPSPs) and AP initiation in principal neurons (Pouille and Scanziani, 2001). GABAergic inputs originating from PV interneurons generate fast inhibitory conductance right before the AP initiation in principal neurons (Hu et al., 2014), thus regulating the activity in a great number of principal cells. Their role in feed-back inhibitions is also crucial. In the winner-takes-it-all mechanism the pyramidal cell which gets the strongest input fires earlier than the

others, thus the remaining cells get inhibited (de Almeida et al., 2009). This mechanism is important for the understanding of, for instance, how grid cells respond in a well-determined place in the EC and the grid-place code conversion (Hafting et al., 2005, Leutgeb et al., 2007, de Almeida et al., 2009). The feed-back inhibition is compound of two types: the early inhibition is mediated by perisomatic interneurons while the late one is mediated by dendrite targeting interneuons (Pouille and Scanziani, 2001). Feed-forward and feed-back inhibition of perisomatic interneurons are also crucial in the local microcircuits which generate high frequency oscillations during SPWs as discussed above.

As I already mentioned, perisomatic interneurons have a crucial role in the generation, organization and synchronization of the SPW and ripple activities as well. High frequency ripple oscillations recorded in pyramidal neurons in whole cell mode shows oscillating postsynaptic potentials IPSPs, which indicate the important role of the perisomatic inhibitory inputs in the generation of the high frequency oscillations. The excitatory current temporally preceeds the inhibitory current in the LFP recording during SPW-R acitivities (Maier et al., 2011, Schlingloff et al., 2014) indicating that the surrounding pyramidal neuronal population can stimulate the local subnetwork of perisomatic interneurons, mostly including the basket cell population (Schlingloff et al., 2014, Stark et al., 2014). The activity is not uniform in the different hippocampal layers. Basket cells mediated inhibition to the pyramidal cells in the deep layers is stronger than those located in the superficial layers (Lee et al., 2014). Moreover, an *in vivo* study showed that interneurons receive excitatory inputs from diverse CA3 and CA1 pyramidal cell assemblies (Patel et al., 2013). Even tonic excitatory drive can entrain the activity of the reciprocally connected PV-positive basket cells, which then start ripple frequency range spiking activity. This activity is phase locked through reciprocal inhibition (Schlingloff et al., 2014).

DOI:10.14753/SE.2015.2055

1.6. Dendritic integration and role in SPW-R oscillation of fast spiking PV interneuron

1.6.1. Dendritic signal integration and dendritic Ca^{2+} spike

The theory of passive dendritic properties has assumed that dendritic arbour works as an antenna. In this case the signal propagation depends only on the membrane conductance, membrane capacitance, membrane resistance and the dendritic morphology (branch number, dendritic diameter) of the cells. These parameters indicate linear summation of the signal (Rall et al., 1966, Abrahamsson et al., 2012, Vervaeke et al., 2012). In this model no active ion channel contributes to the generation of signal transmission. The presence of active conductance on the dendrites, in contrast to this theory, predicts that these voltage-gated ion channels amplify the signals and thus results in sub-and supra-linear summations of the signals. The signal integration, the localization and density (Lorincz and Nusser, 2008) of the different ion channels in the dendrite effect synaptic events which may even lead in some cases to the firing of the neurons. The simultaneously arrived inputs to the dendrites can increase the local membrane potentials up to the threshold of voltage-gated ion channels. These responses are similar to action potential but emerge locally in dendrites. These local regenerative events are called dendritic spikes (Llinas et al., 1968, Golding et al., 1999, Gasparini et al., 2004). The types of dendritic spikes depend on what kind of voltage sensitive ion channel plays a role in its generation. Thus we can distinguish calcium (Llinas and Sugimori, 1980, Larkum et al., 1999, Waters et al., 2003, Larkum et al., 2009), sodium (Ariav et al., 2003, Magee and Johnston, 2005, Losonczy and Magee, 2006) and NMDA (Schiller et al., 1997, Schiller et al., 2000, Larkum et al., 2009) dependent spikes.

Dendritic Ca^{2+} spikes can induce LTP on pyramidal cells (Golding et al., 2002) and can affect the network activity through somatic action potential modulation (Golding et al., 1999). *In vivo* study demonstrated that Ca^{2+} spikes could modify the oscillative SPW-R network activity by local processing in hippocampal pyramidal neurons (Kamondi et al., 1998). The Ca^{2+} spikes can travel below the lowpass filtering threshold of the dendrites due to their slower rise and decay times. They emerge from multiple events as fast, burst-like activity which followed by a sort of synaptic events that increase the membrane potential to a threshold of the VGCC activation (Schiller et

al., 1997, Kamondi et al., 1998). In addition there is another type of Ca^{2+} spikes with the characteristic of longer depolarization at the dendrites which leads to Ca^{2+} plateau potentials that start with a short, burst like event and then keeping the dendrite at a hyperpolarized state for a longer period of time (Golding et al., 1999).

Single neuronal computation in the neuronal networks can be achieved by synaptic integration. In pyramidal cells, around 6 synchronously activated spines are needed for supralinear summation of signals (Losonczy and Magee, 2006). Similarly to the pyramidal cells' spines, the interneurons have a well-defined functional compartmentalization of responses (Goldberg et al., 2003a, Goldberg et al., 2003b, Rozsa et al., 2004) which makes for similar integration properties possible.

1.6.2. Dendritic properties of FS-PV INs

In contrast to the dendritic backpropagation AP calcium response in pyramidal cells, calcium signals in PV INs (basket and axo-axonic cells) show a high restricted spatial extent (Goldberg et al., 2003b, Aponte et al., 2008, Hu et al., 2010, Camire and Topolnik, 2014). This is in agreement with the literature, namely the dendrites of PV containing neurons are passive (**Figure 5**). Low densitiy of voltage gated Na^+ channels (Hu et al., 2010) and high densitiy of K^+ channels (Goldberg et al., 2003b) indicate high dendritic ratio of K^+ to Na^+ channels, which basically distinguishes their dendritic properties from other type of neurons (Stuart and Sakmann, 1994, Golding and Spruston, 1998, Martina et al., 2000, Vervaeke et al., 2012). With this ion channel content, it is understandable that dendritic spikes cannot be evoked neither by dendritic current injection nor by synaptic stimulation, at least in PV INs located in DG (Hu et al., 2010). In thin dendrites of PV interneurons AMPA receptor-mediated conductances generate EPSPs with large peak amplitude (Norenberg et al., 2010) which can reach the high activation threshold of Kv3 type of voltage-sensitive K^+ channels (Rudy and McBain, 2001). These channels show fast activation and fast deactivation kinetics (Rudy and McBain, 2001). Activation of these K^+ channels help in shortening the decay time of the EPSPs, shortening the time period of temporal summation and promoting AP initiation with high speed and temporal prescision (Fricker and Miles, 2000, Hu et al., 2010). K^+ channels activation supports sublinear integration and makes PV cells sensitive to distributed excitatory inputs but not clustered ones (Hu et al., 2010).

DOI:10.14753/SE.2015.2055

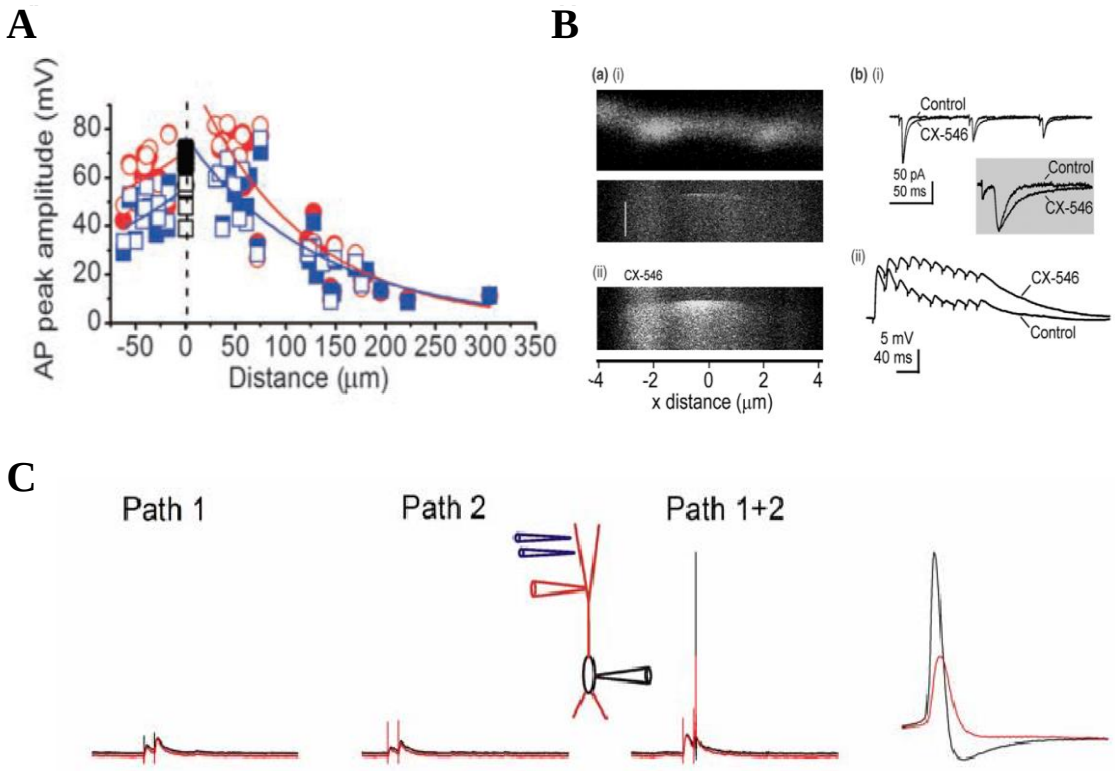

Figure 5. Passive properties of FS-PV INs. A: Action potentials in basket cell dendrites show robust amplitude' attenuation as a function of the distance, indicating passive action potential back-propagation**.** Positive distance, apical dendrite; negative distance, basal dendrite; both measured from the center of the soma. (*Source:* Hu et al., 2010). **B:** Local Ca^{2+} signaling and fast sublinear integration. Left: Thin, aspiny dendrite of a perisomatic interneuron with the representation of Ca^{2+} microdomain mediated by Ca^{2+}-permeable AMPA receptors. CX-546 inhibits AMPA receptor deactivation, resulting prolonged Ca^{2+} influx and summation of EPSPs (Right). (*Source:* Goldberg et al. 2005). **C:** Stimulation of two inputs fails to evoke dendritic spikes indicating the lack of dendritic spikes in basket cells (*Source*: Hu et al., 2010).

1.6.3. Activity of FS-PV INs during physiologically relevant SPW-R oscillations

During hippocampal SPW-Rs reactivation of previously established cell assemblies correspond to synchronized population dischargies and plays a crucial role in establishing long-term memory traces in the neocortex (Girardeau et al., 2009, Buzsaki, 2010, Buzsaki and Silva, 2012, Lorenz et al., 2012). A stochastic transient increase in pyramidal cell firing is generated autonomously in CA3 evoking depolarization in pyramidal cells and interneurons in CA1, leading to the generation of

network ripple oscillations (Traub and Bibbig, 2000, Buzsaki and Silva, 2012). The precisely timed input activity of CA3 neurons is nonlinearly transformed to neuronal output by the somatic and dendritic compartments of downstream neurons (Losonczy and Magee, 2006, Larkum et al., 2009, Katona et al., 2011). Voltage-gated ion channels contribute to the nonlinear dendritic processing which interacts through locally propagating and attenuating membrane potential fluctuations. Dendritic signal integration can be clustered in small (~10 μm) dendritic computational subunits ('hot-spots') (Polsky et al., 2004, Katona et al., 2011). In addition, voltage-gated ion channels activation can induce more global signals, thus regenerative dendritic spikes are engendered when more synaptic inputs are activated in synchrony (Stuart, 1999, Schiller et al., 2000, Larkum et al., 2009).

Several facts suggest that SPW-R-associated cell assemblies can activate dendritic hot-spots, but the relationship between SPWs, field ripple oscillations and dendritic hot-spots have not yet been studied. Synchronized cell assemblies have been shown to activate dendritic hot-spots (Kleindienst et al., 2011, Makino and Malinow, 2011, Takahashi et al., 2012) during a SPW-R event up to 10% of the total neuronal population discharges in the hippocampus, making SPW-Rs the most synchronized cell assembly pattern in the entire cortex (Buzsaki and Chrobak, 1995, Buzsaki, 2010). Moreover, synaptic inputs in dendritic hot-spots have been reported to be locally synchronized for an interval of around 60 ms (Takahashi et al., 2012), which matches the average length of individual SPW-R events (Buzsaki and Silva, 2012).

However, how and why these SPW-R-associated cell assemblies activate dendritic hot-spots and if this activation changes the dendritic computation and AP output of individual neurons, have not been investigated yet. Hippocampal FS-PV INs show higher activity rate than other types of neurons during SPW-Rs and their firing is strongly phase-locked to ripple oscillations (Klausberger et al., 2003, Bahner et al., 2011). It was shown that FS-PV INs play a crucial role in the generation of synchronized cell assembly activities, even in the SPW-R generation (Sohal et al., 2009, Buzsaki and Silva, 2012, Lapray et al., 2012, Taxidis et al., 2012, Tukker et al., 2013, Schlingloff et al., 2014, Stark et al., 2014). According to the generally accepted view, FS-PV INs act in cortical circuits as fast and, essentially, passive integrators of synaptic

inputs (Buhl et al., 1996, Pouille and Scanziani, 2004, Glickfeld and Scanziani, 2006, Hu et al., 2010).

Several papers support the passive properties of FS-PV INs: accelerated kinetics of excitatory postsynaptic potentials (EPSPs), a reduced, sub-millisecond temporal window for dendritic integration, and precise and fast coupling between EPSPs and AP outputs (Fricker and Miles, 2000, Goldberg et al., 2003b, Pouille and Scanziani, 2004, Goldberg and Yuste, 2005, Hu et al., 2010). These parameters were measured under the conditions of low network activites, when incoming synaptic activity is low. Ca^{2+} dynamics have been found to be fast in the aspiny dendrites of FS-PV INs and are strongly related to approximately 1 μm long, dendritic microdomains (Goldberg et al., 2003a, Goldberg and Yuste, 2005, Topolnik, 2012). According to the literature, regenerative dendritic spikes cannot be evoked in these cells and back-propagating APs are severely attenuated (Goldberg et al., 2003b, Hu et al., 2010). However, dendritic integration and EPSP-AP coupling can be different under high-activity conditions such as SPW-Rs when neurons receive precisely timed dendritic inputs (Katona et al., 2011).

DOI:10.14753/SE.2015.2055

2. Aims

I. One of my main goals was to reveal active, regenerative Ca^{2+} events in dendrites of FS-PV INs during spontaneous SPW-R activities.

II. Second, I addressed the connection between dendritic spontaneous Ca^{2+} events and the associated membrane potential signals to examine the input-output transformation of FS-PV INs.

III. My third aim was to define how many inputs require to evoke regenerative Ca^{2+} events in the distal dendrites of FS-PV INs and to specify the nonlinear dendritic integration mechanisms in the generation of Ca^{2+} events and associated membrane potential signals in FS-PV INs.

IV. Finally, I clarified the types of ion channels which play a role in the generation and propagation of dendritic Ca^{2+} events and membrane potential signals.

DOI:10.14753/SE.2015.2055

3. Methods

3.1. Mouse line and slice preparation

All experiments were carried out in accordance with the Hungarian Act of Animal Care and Experimentation (1998; XXVIII, section 243/1998.). Acute brain slices were prepared from transgenic mice line where the PV-containing neurons express enhanced green fluorescens protein (eGFP) (Meyer et al., 2002).

Acute hippocampal slices were prepared from 15-30-day old animals. The animals were deeply anesthetised with isoflurane before decapitation. The brain was removed into the ice cold cutting solution, containing (in mM): 2.8 KCl, 1 $MgCl_2$, 2 $MgSO_4$, 1.25 NaH_2PO_4, 1 $CaCl_2$, 10 D-glucose, 26 $NaHCO_3$ and 206 sucrose. Two types of slices were prepared: 450 µm thick slices for the spontaneous SPW-R measurements and 300 µm thick for the uncaging and pharmacological experiments. Horizontal slices were cut with a Vibratome 3000 (Vibratome, Bannockburn, IL, USA). After the cutting procedures the slices were stored at an interface-type chambers at 35°C in normal artificial cerebrospinal fluid (ACSF) solution containg (in mM): 126 NaCl, 2.5 KCl, 2 $CaCl_2$, 2 $MgCl_2$, 1.25 NaH_2PO_4, 26 $NaHCO_3$ and 10 glucose (Rozsa et al., 2004). After the preparation procedures the slices were incubated for at least 1 hour while the normal ACSF solution cooled down to room temperature.

3.2. Recording chambers

For the electrophysiological experiments two types of submerged recording chamber were used. For the recording of the spontaneous hippocampal SPW-R activities we developed a modified version of the dual superfusion recording chamber (Hajos et al., 2009) to improve two-photon imaging (**Figure 6.A-C**). In this type of chamber the 450 µm thick slices were laid on a nylon mesh. Both sides of the slices were oxygenated by simultaneously perfused ACSF at a higher perfusion rate (>10ml/min). The neuronal operation under this conditions might better approximate the physiological conditions, since the spontaneous activities such as SPW-R could be detected. The optical recording was optimized by changing the metal mesh into a nylon slice supporting grid (Warner Instruments; thickness: 100 µm; mesh size: 1.0 mm x 1.0

DOI:10.14753/SE.2015.2055

mm). The Pair of bubble traps was developed to eliminate bubbles from the perfusion tube system and to prevent to reach the recording chamber (**Figure 6.D-E**).

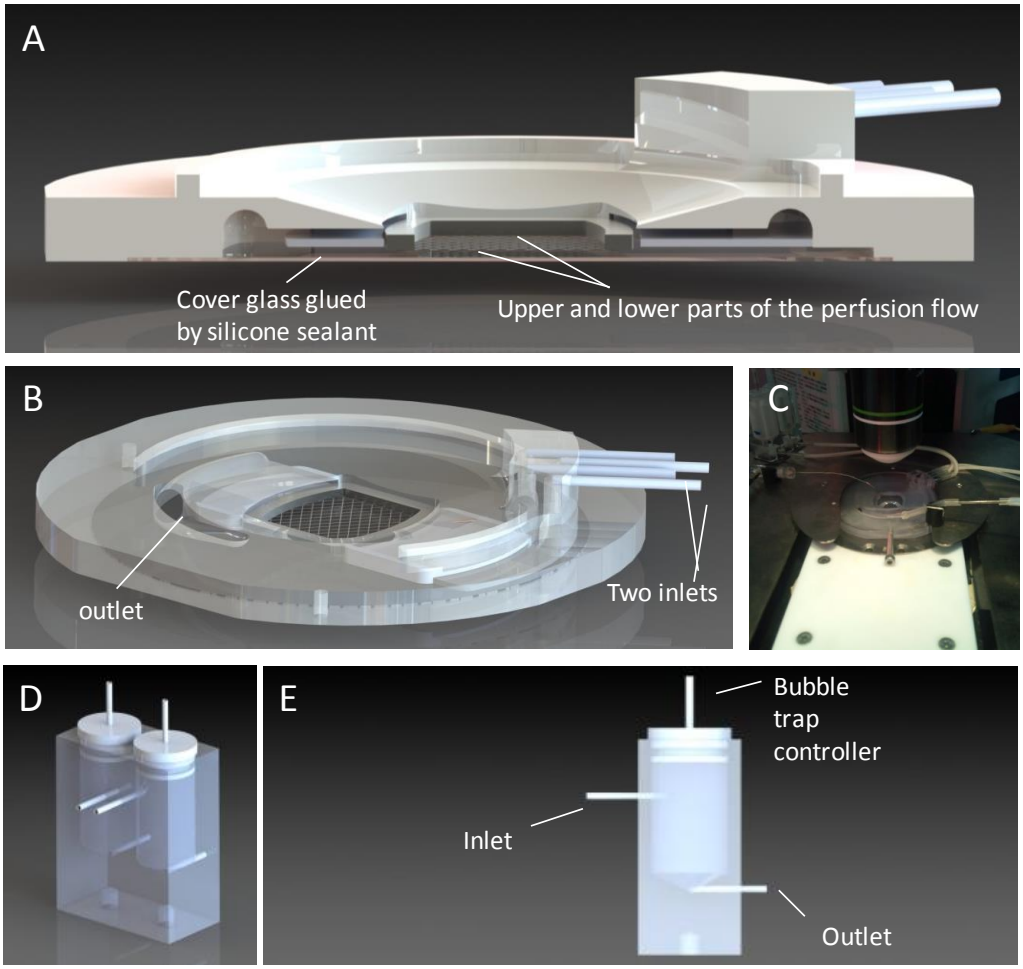

Figure 6. Schematic drawings of the optimized dual superfusion chamber and the bubble trap. A-B: Double perfusion system improved oxygenation of the 450 µm thick acute hippocampal sclices. The slices lay on a polypropylene mesh, the perfusion fluid flows on both sides of the slices. The polypropylene mesh and the glass coverslip on the bottom helped to optimize the optical recordings. **C:** Picture of experimental setup, during recordings. **D-E:** Polycarbonate bubble trap. The upper inlet and lower outlet eliminate the bubbles and reduce the vibrations of the perfusion system.

For the pharmacological experiments a commercially available chamber was used (Luigs&Neumann, Ratingen, Germany) that was equipped with single perfusion tubing. In this system 300 µm thick slices were used where spontaneous activities were

low. In this case the neuronal operation could be limited, which resulted a smaller neuronal activity.

3.3. Electrophysiology

Whole cell patch-clamp recordings were performed from FS-PV INs in the stratum pyramidale of CA1 region of the hippocampus. The LFP was recorded from the CA1 (close to the patched FS-PV IN) or the stratum pyramidale of the CA3. Both recordings were acquired by a MultiClamp 700B amplifier and digitized with a Digidata 1440 Data Acquisition System (Molecular Devices, Sunnyvale, CA, USA) and MES (Femtonics Ltd., Budapest, Hungary) software. Both patch clamp and LFP recordings were performed with 6-9 MΩ-resistance borosilicate glass electrodes. For LFP recordings, the intrapipette solution was normal ACSF. For whole cell recordings the pipette contained (in mM): 125 K-gluconate, 20 KCl, 10 HEPES, 10 Di-Tris-salt phosphocreatine, 0.3 Na-GTP, 4 Mg-ATP, 10 NaCl, and 0.008 biocytin. Patch pipettes also contained 100 µM Fluo-4 (Invitrogen, Budapest, Hungary) or 60 µM Oregon Green BAPTA-1 (OGB-1, Invitrogen), both in combination with 100 µM Alexa 594 (Invitrogen). The LFP signals were band-pass filtered offline (1Hz – 3 kHz and 100 – 300 Hz) using a built-in filtering function of the MES software package. Juxtacellular signals were recorded using glass electrodes (6-9 MΩ) filled with normal ACSF solution comparable to that obtained during LFP recordings. The electrophysiological recordings were performed at 32-34°C (in-line heater: Supertech; chamber heater: Luigs & Neumann).

FS-PV INs were visualized using a 880 nm infrared oblique illumination and two-photon imaging (830-900 nm) (**Figure 7**). For the physiological and optical recordings, cells were accepted with a resting membrane potential more negative than –50 mV. The recorded interneurons represented the typical electrophysiological properties of fast-spiking interneurons (Lamsa et al., 2007) (maximum firing frequency = 206.66 ± 43.33 Hz; firing adaptation = 7.8 ± 1.7 %; AP amplitude = 52.6 ± 12.4 mV; resting membrane potential = -63.9 ± 7.6 mV; n=47 cells). Backpropagating action potentials (bAPs) were induced by somatic current injections (700 pA for 5 ms; five bAPs were evoked at 40 Hz). Step depolarization was also induced by somatic current injections (1500-1700 pA for 100 ms).

DOI:10.14753/SE.2015.2055

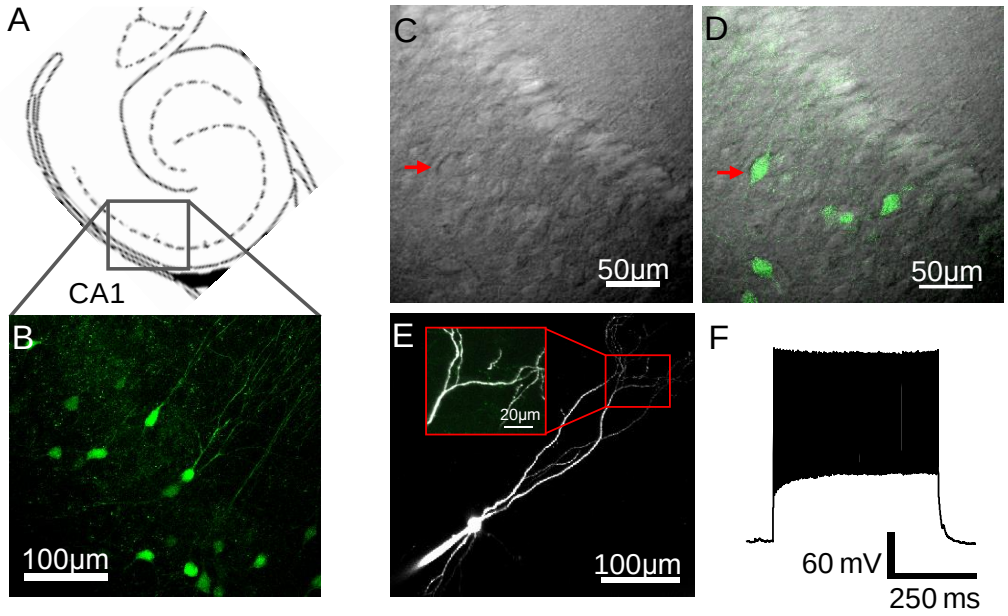

Figure 7. Identification of hippocamapal FS-PV INs in the CA1 region. A: Schematic drawing of the hippocampus, black box indicates the scanned CA1 region. **B:** Maximum intensity two-photon image stack projection of PV-containing interneurons in the strata pyramidale and oriens. The PV cells were visualized by 900 nm two photon imaging. **C:** Transmission infrared image of the stratum pyramidale. Red arrow indicates the localization of a FS-PV IN. **D:** Two-photon TiR and PMTgreen channel image are overlapped to show the PV content of the targeted cell. **E:** Maximum intensity two-photon image stack projection of the patched interneuron (PMTred). For whole cell recording, glass electrode was filled with intrapipette solution, containing Fluo-4 calcium sensitive dye (100µM) and ALEXA 594 (10µM). Inset: Enlarge image of the distant dendrites of the neuron (merged of the PMTgreen and PMTred images). **F:** Somatic voltage trace from the cell upon step depolarization. The recorded interneurons had the typical electrophysiological properties of fast spiking interneurons.

For the classification of the FS-PV INs, passive membrane properties (**Table 1**) were measured in a whole-cell current-clamp configuration (Buhl et al., 1996, Gloveli et al., 2005). No holding current was introduced during the estimation for resting membrane potential. Input resistance (R_{in}) and the membrane time constant (τ) were calculated from voltage responses to current injections (500 ms, 50 pA). The AP properties (e.g. half width) were measured for the first AP, evoked by an increased depolarizing current injection. To determine the AP accommodation, we increased the

somatically-injected current until the cell reached its maximal firing frequency (~800 pA, 500 ms). The level of the accommodation was estimated by the rate of the first and last 100 ms interval firing frequencies. Five bAPs were induced with somatic current injections (500-700 pA for 5 ms, five current steps at 40 Hz). LFP signals were recorded in a ~ 50 μm distance from the measured cell's soma of the hippocampal CA1 region. In a different set of experiments, LFP signals were recorded at the same area where the dendritic segments were activated and then the pipette was gradually moved away from the activated dendritic segment. Electrophysiological data were filtered at 3-10 kHz and sampled at 20 kHz. In some measurements, LFP signals were further filtered with a 3-5 kHz low-pass Bessel filter before baseline subtraction method (see later). Spectrograms are shown in the 0-600 Hz range (15-40 ms window side). In some cases, a sine wave was fitted to the low-pass filtered raw traces and was then subtracted in order to remove the 50 Hz noise.

3.4. Pharmacological experiments

All drugs were applied in the bath, except local TTX injection. Tetrodotoxin (TTX) (1 μM), nimodipine (20 μM), mibefradil (10 μM), ω-connotoxin MVIIC (0.5 μM), 6-cyano-2,3-dihydroxy-7-nitro-quinoxaline (CNQX) (10 μM) and D,L-2-amino-5-phosphonopentanoic acid (DL-AP5) (60 μM) were purchased from Tocris Bioscience. The cocktail of voltage-gated calcium channel (VGCC) blockers contained ω-connotoxin MVIIC, nimodipine, and mibefradil as well. During local puff of TTX we injected 10 μM TTX in combination with Alexa 594 using a patch pipete (6-9 MΩ).

3.5. Two-photon imaging

Two-dimensional two-photon imaging in the dendrites was performed during the glutamate-uncaging and pharmacological experiments where spontaneous neuronal network activity was low. 2D and 3D two-photon Ca^{2+} imaging was achieved when spontaneous SPW-R activities were occurred (**Figure 8**). Two-photon imaging started 15–20 min after obtaining the whole-cell configuration on a two-photon laser-scanning system (Femto2D, Femtonics Ltd., Budapest) equipped with a femtosecond laser tuned to 830 nm (Mai Tai HP, SpectraPhysics, Mountain View, CA, USA). The use of

DOI:10.14753/SE.2015.2055

Multiple Line Scan Imaging increases the signal to noise ratio (S/N), accelerates data collection and abolishes the effect of the time-dependent amplitude decrease of Ca^{2+} transients. In this scanning mode, user selected multiple regions of interest (ROIs) were scanned with constant speed and the intermediate sections were jumped over quickly within approximately 60 μs. Measurement control, real-time data acquisition and analyses were performed with Matlab- and C++-based MES program package (Femtonics Ltd., Budapest).

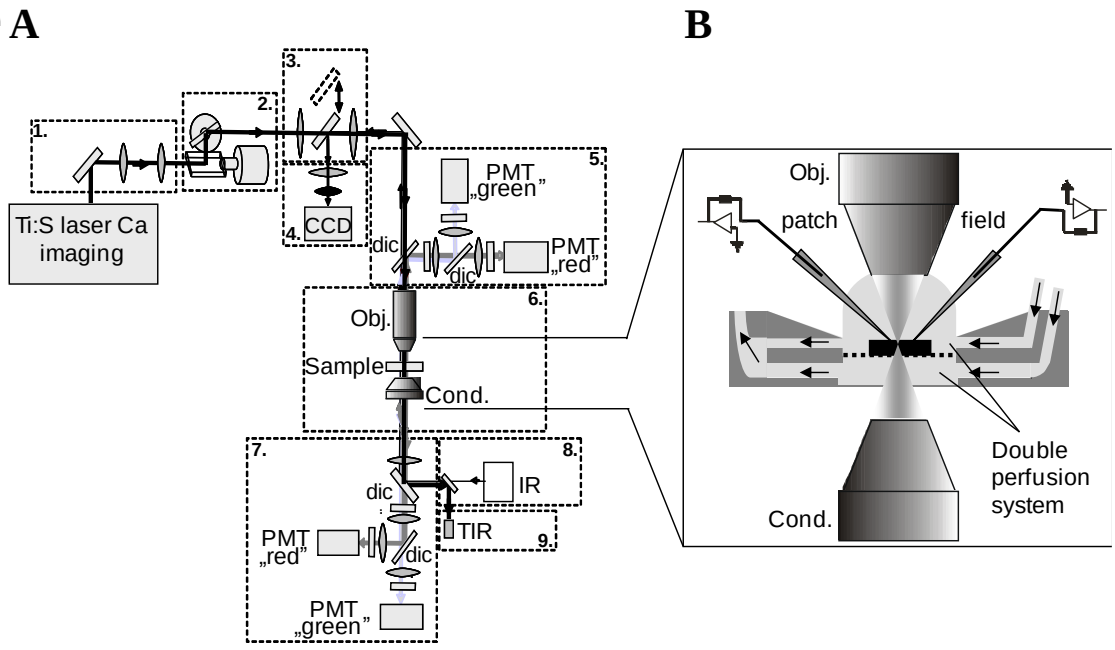

Figure 8. Schematic diagrams of the 2D two-photon experimental setup. A: Schematic drawing of the light path of the two-photon laser scanning microscope system used for imaging. (*PMT*; photomultiplier, *dic*; dichroic mirror, *IR*; light source, *TIR*; transmission infra-red detector). **B:** Schematic diagram of the perfusion flow in the dual superfusion chamber. The fluorescent signal was detected through both the high NA condenser (*cond.*) and the objective (*obj.*) lenses. Whole-cell patch-clamp and field recordings were performed simultaneously

3.5.1. Fast 3D two-photon imaging with acousto-optical scanning

In this study, I used a novel 3D-AO imaging (**Figure 9.A**) and trajectory scanning method (Katona et al., 2012) to increase the total transmission efficiency at higher wavelengths. Spatial resolution and scanning volume were also increased by

about 20% and 10%, respectively, by optimizing the system for the new XLUMPlanFI20×/1.0 objective lens (Olympus, 20×, NA 1.0). New software modules were also developed for fast 3D dendritic measurements and to compensate for sample drift. Three-dimensional acousto-optical trajectory scanning was performed as previously described (Katona et al., 2012). Laser pulses (at 810 nm or 875 nm) were provided by a Mai Tai eHP DeepSee femtosecond laser (SpectraPhysics). Coherent back-reflection was eliminated using a Faraday isolator (BB8-5I, Elec tro-Optics Technology). A motorized four-prism sequence compensated for most of the second- and third-order material dispersion (−72,000 fs2 and −40,000 fs3) of the optical path (Proctor and Wise, 1992, Rozsa et al., 2007). The final optimization of the dispersion compensation was performed using the motorized four-prism sequence in the acute slice during measurements. The thermal drift of the long optical pathway elements was compensated by using motorized mirrors (AG-M100N, Newport) and quadrant detectors (PDQ80A, Thorlabs) in a closed-loop circuit. The optical feedback signal was delivered to the surface of the quadrant detectors through custom-polished broad-band mirrors (BB2-E03; Thorlabs). Next, the beam was extended to 15 mm by a Galilean telescope (NT47319, Edmund Optics; ACN254-075-B, Thorlabs) in order to fit the large aperture of the acousto-optical deflectors. Z-focusing and lateral scanning was achieved by two separate pairs of acousto-optical deflectors which were coupled by two achromatic lenses (NT32-886, Edmund Optics). Finally, the light was coupled to an upright two-photon microscope (Femto2D, Femtonics Ltd.) using a telecentric relay consisting of an Edmund Optics (NT45-180, f = 250 mm) and an Olympus (f = 210 mm) lens. The excitation was delivered to the sample and the fluorescence signal was collected, using an XLUMPlanFI20×/1.0 lens (Olympus, 20×, NA 1.0) and then separated using dichroic mirrors (700dcxru, Chroma Technology). The separated fluorescence was delivered to GaAsP photomultiplier tubes fixed on the objective arm (H7422P-40-MOD, Hamamatsu). The fluorescence photons propagating opposite the objective were captured by photomultiplier tubes mounted below the condenser lens in order to enhance the collection efficiency of the scattered photons. 3D imaging started 20 minutes after attaining the whole-cell configuration.

DOI:10.14753/SE.2015.2055

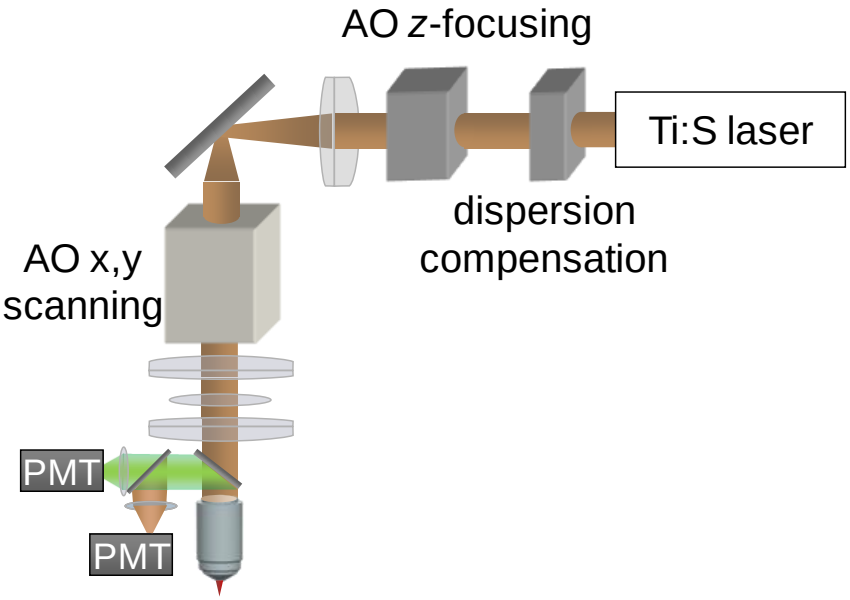

Figure 9. Schematic diagram of 3D two-photon imaging. A: Block diagram of two-photon 3D Acuosto-optic microscope light path for fast z and lateral scanning.

3.6. Two-photon uncaging experiments

DNI-Glu•TFA [2(S)-2-amino-5-(4-methoxy-5,7-dinitro-2,3-dihydro-indol-1-yl)-5-oxo-pentanoic acid-glutamate trifluoroacetate] (2.5 mM) was applied in the bath. DNI-Glu•TFA was photolised at 740 nm using a second ultrafast pulsed laser (Mai Tai, SpectraPhysics). Laser intensity was set using an electro-optical modulator (model 350–80 LA; Conoptics) after beam expansion (1:2, Thorlabs). The laser light was directly coupled into the imaging pathway of a two-photon microscope (Femto3D-RC, Femtonics Ltd.) with two motorized mirrors and a polarization cube (PBS10; Thorlabs). Imaging was interleaved with short uncaging periods during which the uncaging focal spot was jumped to the preselected locations in jump times of 40-50 µs. Fluorescent data values, collected during these uncaging periods, were used to monitor and correct uncaging positions relative to the imaged dendritic segment. Single-spot uncaging laser intensity was set to reproduce unitary EPSPs induced by local injection of high osmolar artificial cerebrospinal fluid (Katona et al., 2011), at similar distances from the soma where spontaneous activity was detected (amplitude of high osmolar artificial

cerebrospinal fluid-induced EPSPs was 0.71±0.06 mV, n=4). When recording the input-output curves of neurons, uncaging at the maximum number of selected locations (43.8 ± 2.9) was allowed first, then the inputs were gradually but randomly removed. Inputs were sequentially activated because the use of more complex sequences of active inputs in the same total uncaging time window did not cause any significant difference in the response amplitudes. Finally, uncaging with the maximum input number was repeated at the end of each experiment, and only experiments with the same final and initial maximum amplitude were accepted.

With the application of DNI-Glu•TFA, it became possible to rapidly and repetitively activate the required high number of unitary inputs (up to 60) in a short time period (4.39±0.32 ms, n=35 cells) without inducing a detectable level of phototoxicity in the dendrites. The trajectory of long dendritic segments (53.5±2.9 µm) was rapidly scanned (at 170-500 Hz) and after a 500 ms baseline period, DNI-Glu•TFA was uncaged at up to 60 locations in each sweep. We characterized each cell's input-output function by plotting the simultaneously-recorded Ca^{2+} and somatic voltage responses as a function of the progressively increasing input number, until the density of active inputs reached 1.36±0.09 synapses/µm, corresponding to the reported excitatory synapse density (1-5 synapses/µm) of FS-PV INs (Gulyas et al., 1999). The clustered active input pattern covered, on average, an 18.3±1.4 µm long dendritic segment (termed hot-spot region) on the apical dendritic tree in the distal dendritic region (235.4±63.5 µm, from the soma; mean ± s.d.), where large spontaneous SPW-EPSP-associated 3D Ca^{2+} responses were usually detected.

3.7. Measurement of oxygen concentration in slices

To define the oxygen concentrations in our slice preparations under different conditions and depth, an optode was used (tip diameter ~50 µm; Microx TX3, PreSens GmbH, Germany). The oxygen concentration in the hippocampal CA1 stratum pyramidale region was measured in brain slices having thickness of 300 µm or 800 µm. To eliminate the dissolved oxygen from the non-bubbled ACSF (defined as 0% oxygen) the sensor was calibrated using 2–3 mM of sodium sulfite (Na_2SO_3). Approximately 95% oxygen was set in ACSF, bubbled for one hour with a mixture of 95% O_2/ 5% CO_2.

DOI:10.14753/SE.2015.2055

The recording of oxygen saturation was started 200 µm above the slice within the perfusate. Thereafter, the sensor tip was lowered diagonally into the tissue with 50 µm steps using a micromanipulator (**Figure 10**). The oxygen level was recorded at each step for 30 seconds at 1 Hz. The raw data of this period were averaged and expressed as oxygen saturation % and µmol/l dimensions. Thin (300 µm) slices were measured in a regular, submerged-type chamber with single perfusion and at low flow rate (3.5 ml/min), while the 800 µm thick slices were recorded in a dual superfusion chamber at a high perfusion rate (11.2 ml/min).

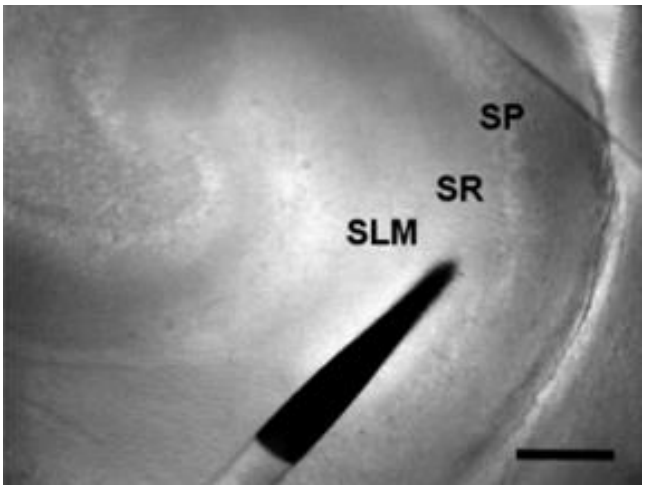

Figure 10. Charge-coupled Device (CCD) image of a hippocampal slice with an optode used for oxygen concentration measurements. *SP*; stratum pyramidale, *SR*; stratum radiatum, *SLM*; stratum lacunosum-moleculare.

3.8. Histology

After the experiments, slices were fixed in a mixture of 4% paraformaldehyde and 15% saturated picric acid dissolved in 0.01 M phosphate buffered saline (PBS; pH 7.4). For biocytin visualization, the slices were washed three times in PBS and subsequently incubated for 30 min in 0.3 v/v% TritonX-100 (Sigma-Aldrich) in PBS and overnight in 1/200 dilution of Fluorescein (DTAF) streptavidin complex (Jackson ImmunoResearch Europe Ltd.). The slices were then washed in PBS, mounted on glass slides in Vectashield Mounting Medium (Vector Laboratories, Inc. Burlingame, CA,

DOI:10.14753/SE.2015.2055

USA) and stored at 4°C. Sections were examined and pictures of the cells were taken with a confocal laser-scanning microscope (FV1000, Olympus) (**Figure 11**).

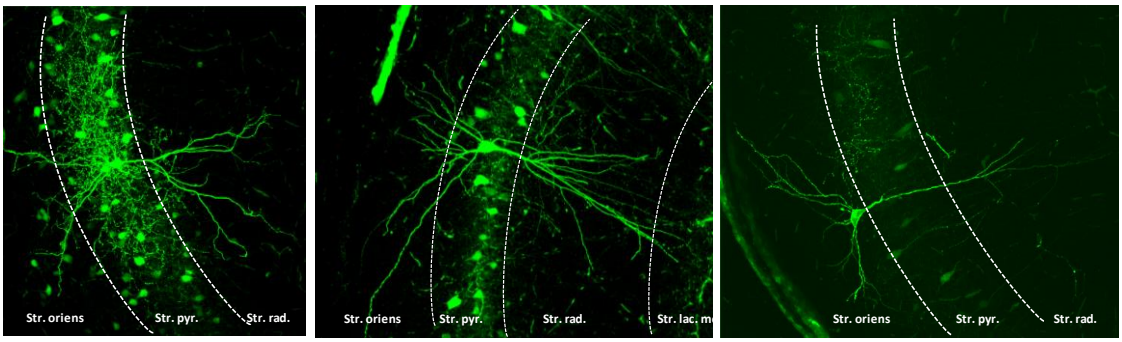

Figure 11. Confocal images of three FS-PV INs in CA1 region of the hippocampus after histological procedures. Dashed white lines indicate the borders of different layers of hippocapus strata.

3.9. Data analysis and statistics

Analysis was performed with a MATLAB-based program (MES, Femtonics) using custom-written software elements. The 3D raw green fluorescent data (*F*) were collected along the dendrite, spatially normalized, and then projected onto a two-dimensional plot (defined as 3D Ca^{2+} responses) by applying the formula:

$$\Delta F/F=(F(d,t) - F_0(d))/F_0(d) \qquad \text{(Equation 1)}$$

or the following formula:

$$\Delta G/R=(F(d,t) - R(d))/R(d) \qquad \text{(Equation 2)}$$

where *d* denotes the distance along the dendrite and *t* indicates time. $R(d)$ and $F_0(d)$ denote red and background green fluorescence, respectively, as a function of distance along the dendrite.

DOI:10.14753/SE.2015.2055

When 3D Ca^{2+} responses were simultaneously collected from multiple dendritic segments (**Figure 12)**, the data were consecutively projected into the same two-dimensional frame and responses from different segments were separated by dashed lines. In order to divide the spatial distributions of the red and green baseline (F_0) raw fluorescence, we measured it in six successive experiments separated by 60 s. Signals were integrated over a 500 ms long interval (**Figure 12C**). Grey dashed boxes show the location where the red and green fluorescence dropped due to the decreasing overlap between the scanning trajectory and the dendrite (**Figure 12C**). As shown in the Figure, peak dendritic Ca^{2+}-responses do not correlate with the normalized *G/R* ratio (Pearson's r = -0.060, n=6 cells) (**Figure 12D**). In addition the average ratio of the green over red fluorescence (**Figure 12E** blue trace) and the average peak dendritic Ca^{2+} response from the same location (**Figure 12E** green trace) (mean ± s.e.m., n=6) were compared. The grey dashed box in **Figure 12E** indicates the location where the red and green fluorescences dropped as in **Figure 12C**. Note that the *G/R* ratio was increased in this location. To avoid similar errors, signals from dendritic segments with a similar fluorescence drop were omitted during analysis. Local maximum in *G/R* inhomogenity was not reflected in the hot-spot Ca^{2+} response (**Figure 12E**). These data indicate that spatial inhomogeneity in the ratio of background green over red fluorescences (**Figure 12**) did not correlate with the amplitude of the dendritic Ca^{2+} responses (**Figure 12D**) and, therefore, it should not affect the Ca^{2+} responses associated with dendritic hot-spots (**Figure 12E**).

The distance-dependent distribution of 3D Ca^{2+} responses to bAPs and SPW-R associated EPSPs (SPW-EPSPs) in FS-PV INs could not be mediated by the small changes observed in F_0 as a function of distance from the soma (**Figure 13**). As indicated, in some measurements the colour look-up table (LUT) was shifted to higher $\Delta F/F$ values in order to better reveal the location of dendritic hot-spots.

DOI:10.14753/SE.2015.2055

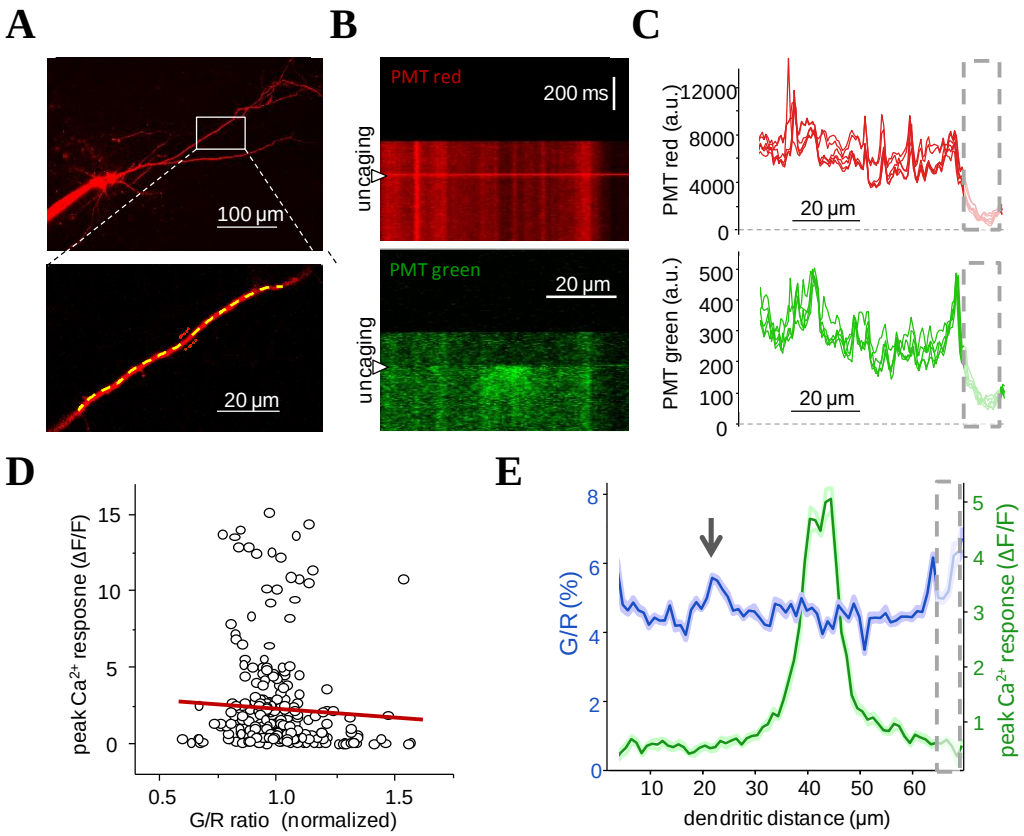

Figure 12. Relative change in baseline green fluoresecence (F_0) as a function of distance from the soma. A: Top, maximum intensity z-projection image of an FS-PV IN (red channel). Bottom, enlarged view of the imaged dendritic segment. Red points indicate the location of the glutamate uncaging. Dashed line shows scanning trajectory along which the inhomogeneity in baseline green and red fluorescences was quantified. **B:** Uncaging-evoked raw Ca^{2+} (bottom) and simultaneously recorded red fluorescence signals (top) shown without any spatial normalization. The white triangles indicate when uncaging occurred. **C:** Spatial distributions of the red and green baseline (F_0) raw fluorescence in six successive measurements separated by 60 s. **D:** Peak dendritic Ca^{2+}-responses do not correlate with the normalized *G/R* ratio (Pearson's r = -0.060, n=6 cells). **E:** Average ratio of the green over red fluorescences (blue) and the uncaging evoked average peak dendritic Ca^{2+} response (green). Grey arrow indicates a local maximum in *G/R* inhomogeneity.(*For more details: see the main text.*)

DOI:10.14753/SE.2015.2055

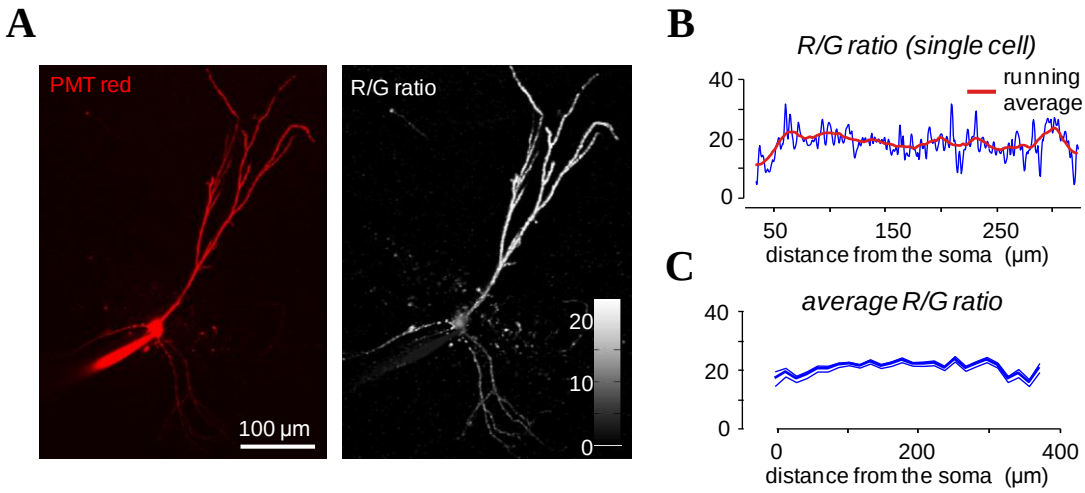

Figure 13. Local inhomogeneity in F_0 fluorescence does not interfere with dendritic Ca^{2+} responses. A: left: Maximum intensity z-projection image of an FS-PV IN (red channel). Right: Red over green (*R/G*) ratio image of the same neuron. Here the *R/G* ratio was used instead of *G/R* ratio for a better demonstration of the data. Note that the *R/G* ratio is relatively homogeneous which also indicated a homogeneous baseline green fluorescence in the dendritic arbor where a distance-dependent change in SPW-associated Ca^{2+} responses was measured (Figure 21A). **B:** The *R/G* ratio plotted as a function of distance in a different neuron. **C:** Average *R/G* ratio (mean ± s.e.m.) in five FS-PV INs show only a small change as a function of distance: this cannot explain the distance-dependent changes in the SPW-R- and bAP-associated dendritic Ca^{2+} responses shown in Figure 21A.

All neuronal input-output curves could generally be characterized by an initially concave or linear curve on top of which a sigmoid-like supralinear increase was superimposed at a given threshold input number. Therefore, the first step towards separating these two mathematically different intervals in the input-output curves was to fit the initial part of the input-output curve below the threshold input number, with a sublinear curve using the following equation:

$$y_1 = A_1(1 - e^{(-A_2*(x-A_3)})} \qquad \text{(Equation 3)}$$

where x denotes the number of glutamatergic inputs, A_i are fitting parameters, and y is the output.

DOI:10.14753/SE.2015.2055

The second step was to subtract the result of this fit from the whole input-output curve and then the ramnant was fitted using a Boltzmann equation:

$$y_2 = \frac{A_4}{1+e^{\left(\frac{x-A_5}{A_6}\right)}} + A_7 \qquad \text{(Equation 4)}$$

Input-output curves with or without the subtraction of the initial sublinear tendency are shown with the fit results (with y_1, $y_{2,\text{ and }}$ y_1+y_2 curves) either alone or in combination (as shown in **Figures 32, 33. and 35**). Threshold input numbers were generally defined as the smallest active input numbers above the sigmoidal increase described by **Equation 4**. The first threshold was simply defined as the smallest active input number above the first sigmoidal jump in the central input region. Similarly, the second threshold was the smallest number of active inputs just above the sigmoidal jumps in the lateral dendritic region: this could be deteced simultaneously in the central dendritic Ca^{2+} responses and somatic EPSPs at a higher input number (**Figure 33**). The active inputs below the first threshold were ignored or subtracted when the fitting **Equations 3 and 4** were used to determine the second threshold.

Relative fluorescence changes were transformed to Ca^{2+} concentration change using the following equation (Maravall et al., 2000, Rozsa et al., 2004):

$$\frac{\Delta Ca}{K_D} = \frac{f_{\max}}{f}\left(1 - R^{-1}{}_f\right)\frac{\delta f}{\left(\delta f_{\max} - \delta f\right)\delta f_{\max}} \qquad \text{(Equation 5)}$$

where δf is $\Delta F/F$, ΔCa^{2+} = $[Ca^{2+}]$ - $[Ca^{2+}]_0$, K_D denotes the affinity of the Ca^{2+} indicator (fluo-4: 345 nM), f_{max} is the maximum fluorescence, and R_f (=f_{max}/f_{min}) denotes the dynamic range of the dye (for a detailed methodology see: (Maravall et al., 2000, Rozsa et al., 2004, Rozsa et al., 2008). The maximal relative fluorescence change, δf_{max}, was determined for each dendritic region at the end of the experiments by using the maximal number of spatio-temporally clustered inputs and increased uncaging laser intensity to induce a burst of APs at the soma (5-10 APs, δf_{max}=6.16±1.15).

To preserve all the information in Ca^{2+} signals during this nonlinear transformation, the relative fluorescent changes of the Ca^{2+} dye must be within the non-

saturating range. Responses were not saturated in the hot-spot region because the subthreshold EPSP-associated Ca^{2+} responses, used throughout the pharmacological measurements, were much smaller than those which were associated with one, two, or three somatic APs, or an AP burst (**Figures 14 and 24A**), therefore they were far below the Fluo-4 saturation level (the average saturation level was: 53.9±6.7%; **Figure 14D**).

The amplitude of the measured Ca^{2+} transients were normalized to single AP evoked signals (EPSP n=8 cells; 2 AP n=3 cells; 3 AP n=6 cells, AP burst n=5 cells).

AP-burst-associated Ca^{2+} response was also induced at the end of the experiments. Note that the responses associated with EPSPs and single APs cannot be saturated as their amplitude is much smaller than that of the burst-associated response.
Normalized $[Ca^{2+}]$ as function of maximum ΔF/F value ($\delta f\max$) were plotted according to Equation 5 shows the nonlinearity of the transformation. One unit of normalized $[Ca^{2+}]$ is equivalent to $K_D \frac{10 f_{\max}}{f \cdot \delta f_{\max}} \left(1 - R^{-1}{}_f\right)$. Note that Ca^{2+} responses associated with uncaging-evoked EPSPs were far below saturation.

In addition, Fluo-4 responses were also not saturated in the lateral dendritic region because their amplitude in this region was much lower than in the hot-spot region (45.6 ± 0.03%, $p < 0.0001$; see for example **Figures 40B and E**). These data indicate that **Equation 5** could be used in the non-saturating range to calculate $[Ca^{2+}]$ and hence remove dye nonlinearity from our measurements.

The propagation speed of dendritic Ca^{2+} spikes was determined in lateral dendritic regions, where Ca^{2+} responses showed plateau-like characteristics. The border of these regions could be characterized by a sharp decrease in the Ca^{2+} response amplitude and was, therefore, detected by the peak in the second derivative.

The statistical difference was estimated using the Student t-test (*, **, or *** indicate p values of less than 0.05, 0.01, or 0.001, respectively). If not otherwise indicated, data are presented as mean ± s.e.m.

DOI:10.14753/SE.2015.2055

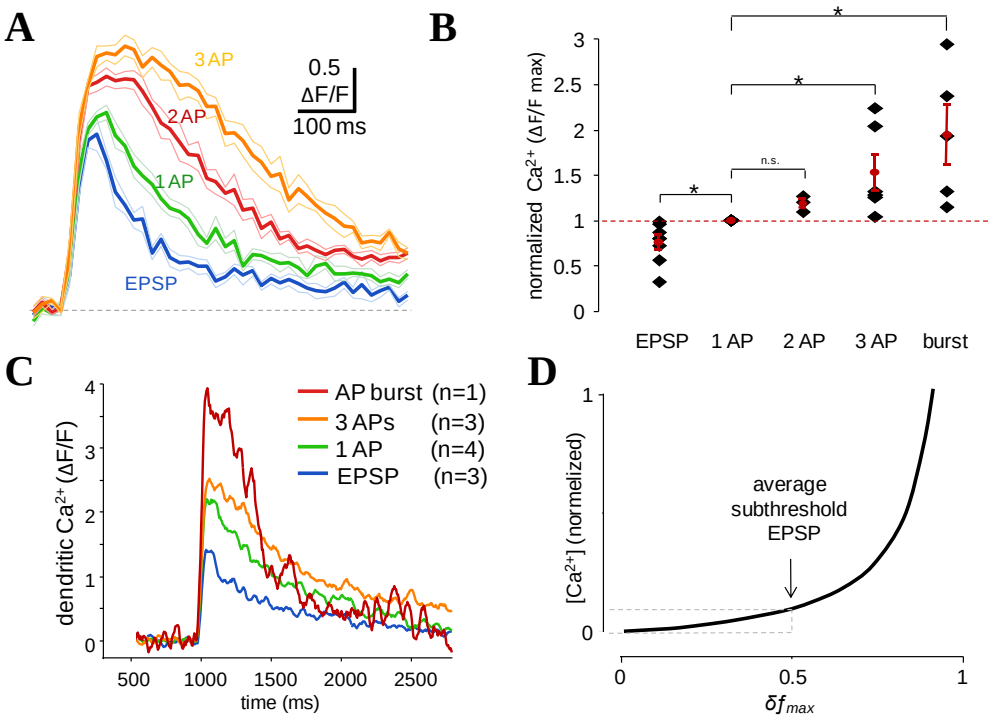

Figure 14. Ca^{2+} responses associated with EPSPs and single APs, used throughout this study, were also far below saturation in the central hot-spot region. A: Ca^{2+} transients in the hot-spot region evoked by clustered glutmamate uncaging (somatically recorded EPSPs (blue), one (green), two (red), and three APs (orange)). **B:** Amplitude of the uncaging-evoked dendritic Ca^{2+} responses (black) and their averages (red) measured in the central input region as a function of the number of the simultaneously recorded APs. Data were normalized to single AP. **C:** Similar dendritic responses for EPSPs (blue), one (green), and three (orange) APs as in A, but an AP-burst-associated Ca^{2+} response was also induced at the end of the experiments **D:** Normalized [Ca^{2+}] as a function of maximum $\Delta F/F$ value (δf_{max}) plotted according to Equation 5.

DOI:10.14753/SE.2015.2055

3.10. Cluster analysis

Gaussian mixture distribution parameters were estimated using the Expectation Maximization algorithm (McLachlan and Peel, 2000) for different component numbers on the seven-dimensional dataset of the 47 FS-PV INs. The mean Bayesian information (Schwarz, 1978) from 1000 estimates was identical for one and two clusters ($p > 0.7$), but was larger ($p < 0.01$) for higher cluster numbers, indicating no clustering. According to these data, the measured FS-PV IN population was electrophysiologically homogeneous.

3.11. Detection of interneuronal ripple oscillations without filtering artefacts using the baseline subtraction method

Band-pass filtering is generally used for demonstrating oscillations in different frequency bands (theta, gamma, and ripple, etc.). For example, network ripple oscillations are typically presented by the use of band-pass filtering in the 100-300 Hz frequency range. However, according to the Fourier transformation theory, band-pass filtering can artificially generate ripple oscillations from short non-oscillating depolarizing humps, which last for a time period of roughly one SPW event (**Figure 15A and 15B**).

SPW-EPSP events recorded in FS-PV INs (n=62) were separated into three groups based on the amplitude of the interneuronal ripple oscillations, which were then averaged (no-oscillation, n=10; medium-oscillation, n=22 and high-oscillation groups, n=30) (**Figure 15A**). Instead of aligning the EPSPs to their peaks, transients were "randomly" and temporally shifted to eliminate phase synchrony of interneuronal fast-ripple oscillations before averaging. This random temporal shift was achieved by aligning all the transients to arbitrary threshold amplitude (7 mV, thr.) (**Figure 15A**). After baseline subtraction, the group of highly-oscillating SPW-EPSPs showed no oscillations and was similar to the non-oscillating group (**Figure 15B** left, red and black, respectively). These data, therefore, show that the random temporal shift in **15D** effectively eliminated phase synchrony and significantly reduced oscillations in the average trace. In contrast, when a band-pass filter (Chebyshev, 100-300 Hz) was applied instead of baseline subtraction, it generated large oscillations in the ripple

frequency range in each of the three groups of SPW-EPSPs, irrespective of whether the SPW-EPSP belonged to the no-oscillation, medium-oscillation, or high-oscillation group (**Figure 15B**, right). Moreover, band-pass filtering over-estimates oscillation amplitudes in the subgroup of SPW-EPSPs which have no, or very low, oscillations (**Figures 15C-E)**. When Chebysev band-pass filtering was used on the same EPSP groups, the separation between the three groups was less evident (**Figure 15D**). In addition, band-pass filtering can generate extra oscillation cycles and artificial phase shifts when the biological oscillations are irregular, e.g. SPW-R-associated interneuronal ripple oscillations (**Figures 16B-C**).

Off-line Gaussian filtering (100 Hz) was used on the raw whole-cell traces to generate a "baseline", which was then subtracted from the raw traces to preserve ripple oscillations (referred to as baseline-subtraction method, **Figure 16A**). In contrast to band-pass filtering, the baseline-subtraction method did not generate any extra oscillation cycles, phase shifts (**Figures 16A-C**), or false oscillations from the relatively slow depolarizing humps which characterize SPW-associated EPSPs (**Figures 15A-E**). Therefore, the baseline-subtraction allowed us to detect individual ripple oscillation cycles in the somatic membrane voltage with the required phase and amplitude precision (**Figure 16A**).

DOI:10.14753/SE.2015.2055

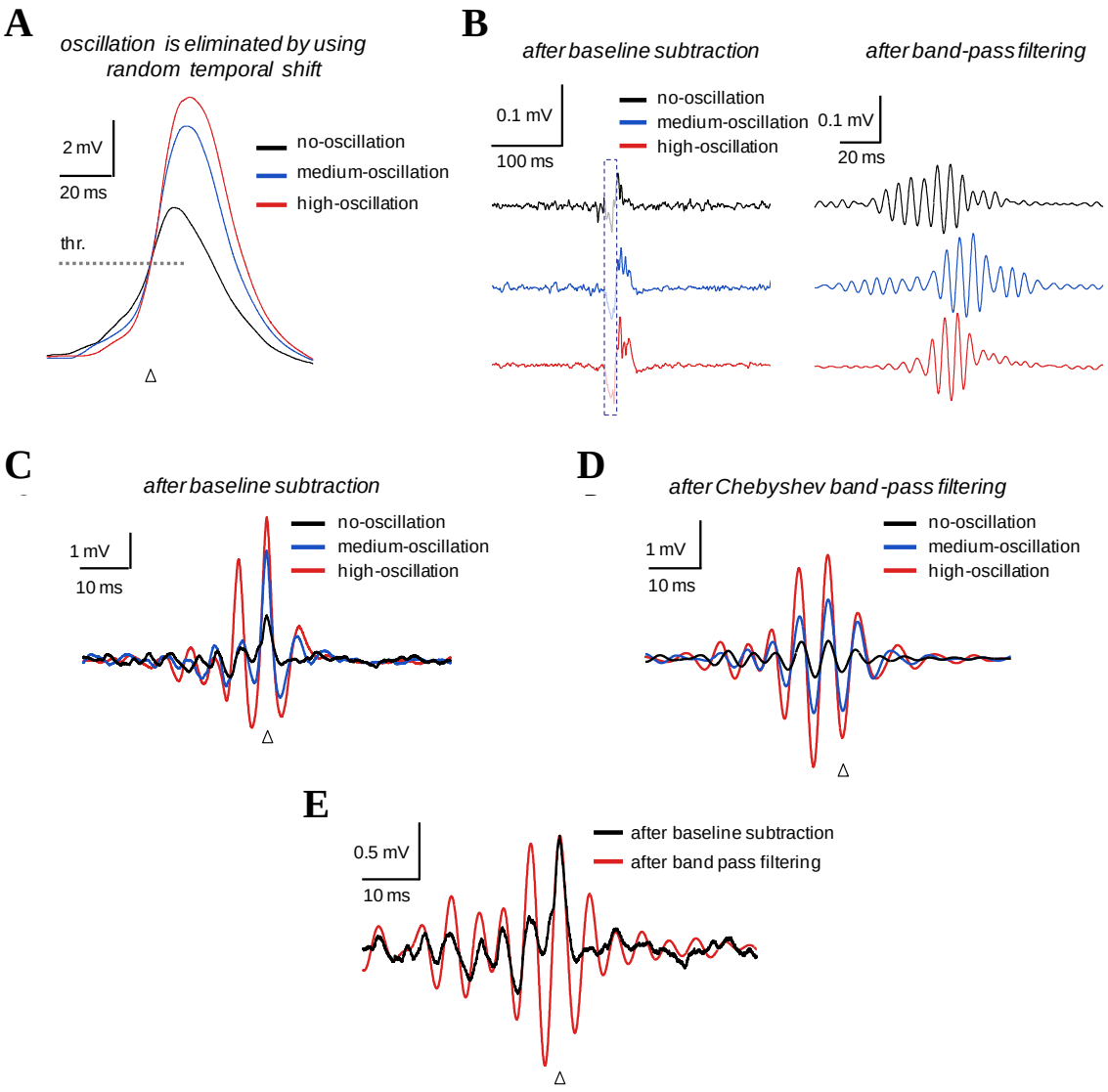

Figure 15. Band-pass filtering versus baseline subtraction methods in the detection of interneuronal ripple oscillations. A: Three groups of randomly and temporally shifted SPW-EPSPs eliminate phase synchrony of interneuronal fast-ripple oscillations before averaging (no-oscillation, n=10; medium-oscillation, n=22 and high-oscillation groups, n=30). **B**, Left: The same three groups of SPW-EPSPs as in A, but after baseline subtraction. Right: SPW-EPSPs after band-pass filter (Chebyshev, 100-300 Hz) was applied **C:** The same three groups of EPSPs as in A following baseline subtraction but without the random shift. **D:** Same as in C, but Chebysev band-pass filtering was used on the same EPSP groups instead of baseline subtraction **E:** Overlay of the non-oscillating groups in C and D.

DOI:10.14753/SE.2015.2055

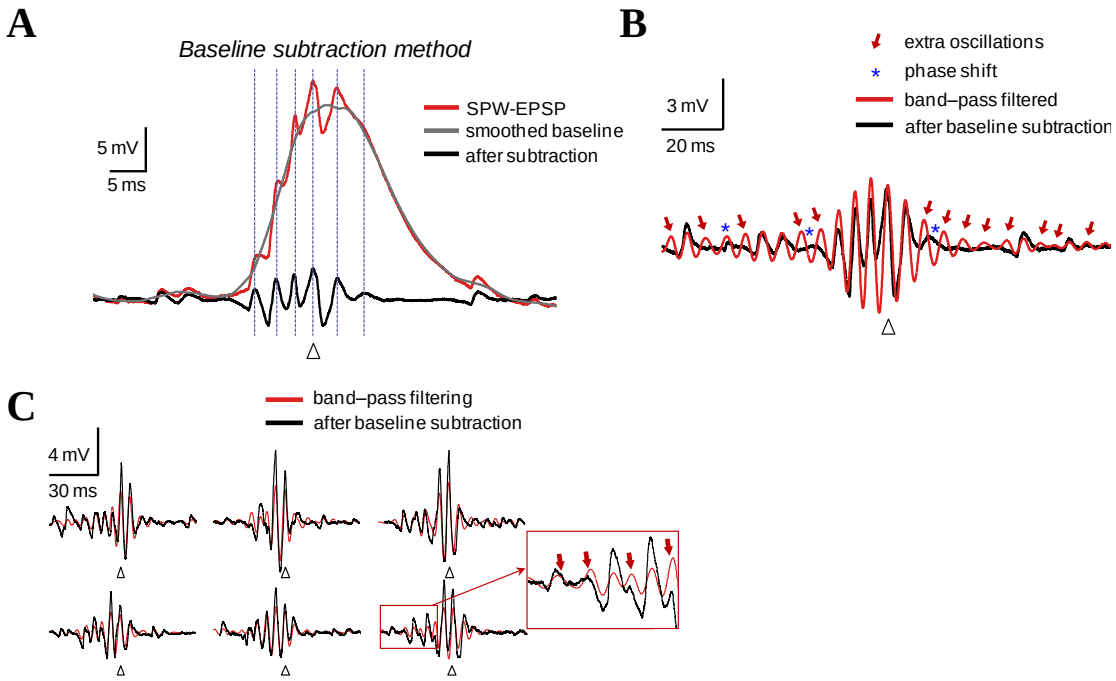

Figure 16. Comparison of the baseline subtraction method and the generally used band-pass filtering for the detection of individual oscillatory cycles during interneuronal ripple oscillations in somatic membrane potential. A: A somatic EPSP with interneuronal ripple oscillations was recorded from an FS-PV IN during an SPW event (red). The high frequency component was removed by Gaussian filtering (cut-off frequency 100 Hz), which yielded a smooth baseline trace with a hump (gray). Oscillations could be seen (black) after subtracting this Gaussian-filtered baseline trace (gray) from the original trace (red). The peak of the SPW-EPSP is indicated with a triangle. Dashed blue lines indicate individual oscillatory events which could be reliably detected by this method. **B:** Comparison of the baseline subtraction method (black) and band-pass filtering (red). Black trace is the same as in A. Note that the use of a Chebyshev band-pass filter (100-300 Hz) resulted in extra oscillation peaks (red arrows), and also shifted the phase of responses (blue asterisks). **C:** Six further examples of baseline-subtracted and band-pass filtered SPW-EPSPs. Similarly to A, all oscillatory events in black traces were also visible on the raw traces (data not shown), but the Chebyshev band-pass filter generated undesired extra oscillatory events. In the enlarged image, the red arrows indicate these events.

The disadvantage of the baseline-subtraction method is that it can generate artefacts in intervals where the transient is rapidly changing, i.e. where the second

DOI:10.14753/SE.2015.2055

derivative is too high. These artefacts could be observed in two cases in our measurements, but in both cases the impact of the artefact on the detection of ripple oscillations could easily be excluded during analysis. In the first case, when EPSPs start with a rapid increase following two-photon glutamate uncaging, the baseline-subtraction method generates a two-phase artefact limited to the initiation phase of the EPSPs. However, interneuronal ripple oscillations occur a few milliseconds after this period, and they could therefore be isolated temporally (see for example **Figure 35A**). I have marked this two-phase artefact with blue dotted boxes in figures. In the second case, when an AP was rising on uncaging or SPW-associated subthreshold depolarizations, the baseline had to be locally corrected before baseline subtraction to avoid generation of an artefact before and after the AP. Therefore, APs were replaced with spline interpolated curves before the baseline was smoothed and substracted. Traces of the interpolated periods were marked with dashed lines in the figures (see **Figures 29B and 36A**).

The ripple frequency of individual traces and averages was determined either by Fourier transformation ($f_{Fourier}$) or by measuring the time between oscillation peaks after baseline subtraction in an interval centered on the peak of raw events (f_{max}).

DOI:10.14753/SE.2015.2055

4. Results

4.1. Recording of spontaneous sharp wave–ripple activities *in vitro* using a modified dual superfusion recording chamber and fast perfusion rate

In order to understand the basic neuronal mechanism underlying SPW-R oscillations, we performed simultaneous two-photon calcium imaging, electrophysiology and pharmacological manipulations. For imaging, a submerged type of recording chambers was required. Recording of the spontaneous sharp wave-rippple activities *in vitro* is difficult in a submerged-type recording chamber but not in an interface-type chamber. One of the main problems is the limited oxygenation of the slices using a submerged-type chamber. In addition, a proper network size is required to create spontaneous neuronal population activities, which have to be well-oxygenized. To have a necessary population of the neurons which can generate oscillations, 450 µm thick slices were used. For the better oxygenation of slices, I used a modified dual superfusion-type chamber; where the perfusate was flow (11.2 ml/min) below and above the slices. The samples were placed on a mesh. Under such conditions the slices could generate neuronal network oscillations. On the other hand, the dual superfusion chamber was modified for better imaging as well. The slice supporting metal mesh was exchanged to a nylon mesh and it was lowered to match the working distance of a high numeric aperture (NA) condenser (**Figures 6A-B and 8B**). Moreover, gas bubbles that normally accumulate below the slices decreasing photodetection efficiency were kept out of the chamber by a custom-made, dual-channel bubble trap (**Figure 6D-E**). The optical aperture of the chamber was increased to be optimized for multi-channel recordings and for the application of high NA objectives with small working distances. In the dual superfusion chamber, SPW-R activities could be recorded because of the better oxigenation. In order to support this idea I measured the oxygen concentration with an optode in different depth of the acute hippocampal slices. The results from a regular chamber with normal flow rate (3.5 ml/min) using 300 µm thick slices and the dual superfusion chamber with an increased flow rate (11.2 ml/min) using 800 µm thick slices were compared. Oxygen concentration decreased rapidly with the depth of the slice in the regular chamber **(Figure 17A)**. Conversely, in the dual superfusion chamber

DOI:10.14753/SE.2015.2055

the oxygen content was high enough for the generation of spontaneous SPWs **(Figure 17A-B)**.

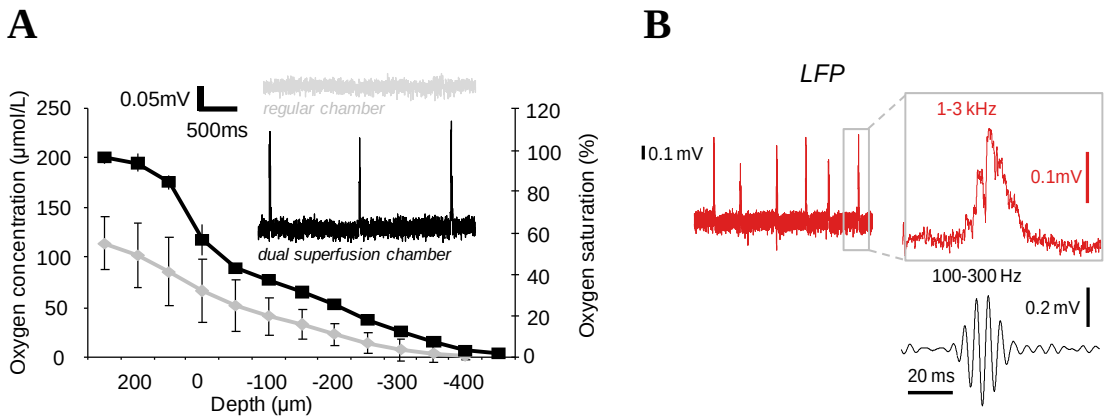

Figure 17. Spontaneous SPW-R activities are recorded in a dual superfusion chamber. **A:** Oxygen concentration and saturation are shown as a function of depth from the surface of the slice in the dual perfusion chamber with fast flow rate (11.2 ml/min; black trace and symbols) and in regular chamber with normal flow rate (3.5 ml/min; gray trace and symbols). Inset: representative local field potentials recorded in regular chamber (top, grey) and in the dual perfusion chamber. **B:** Representative LFP recording from stratum pyramidale with six spontaneous SPW-R events (red). The last event is shown on an extended scale filtered at two different frequency bands.

Under our recording conditions, SPW events occurred spontaneously at a rate of 1.44±0.09 Hz (n=32) and were associated with network ripple oscillations (f_{max} 249.2±12.7 Hz) **(Figure 17B and Movie 1)** (Hajos et al., 2009) using 450 µm thick slices. Importantly, the observed spontaneous SPW-Rs had similar laminar profiles, oscillation frequencies, and hippocampal propagation properties to those observed *in vivo* (Buzsaki, 1986, Hajos et al., 2009, Maier et al., 2011). Therefore, according to the previous observations (Hajos et al., 2009), the dual superfusion chamber with an increased flow rate provides better recording conditions, which can maintain physiological network oscillations such as SPW-Rs.

DOI:10.14753/SE.2015.2055

4.2. SPW-R-associated dendritic input patterns revealed by 3D two-photon calcium imaging

Even nowadays it's still unachievable to measure the long distal dendritic region of the FS-PV INs *in vivo* or *in vitro* in the hippocampal CA1 region even with the generally used imaging and patch clamp techniques. Thus to record the network activity-related dynamic functions of FS-PV INs in slices, 3D fast acousto-optical (3D-AO) trajectory scanning was applied (Katona et al., 2012) with combination of simultaneous whole cell patch calmp recordings and LFP recordings in a dual-supefusion recording chamber (Hajos et al., 2009, Katona et al., 2011). This approach allowed acces to multiple, long, thin, tortuous apical dendritic segments up to 700 µm in length **(Figures 18, 19 and Movie 1)**. GFP expressing FS-PV INs (Meyer et al., 2002) in the CA1 pyramidal layer were identified with two-photon imaging (900 nm) than the cells were filled with a fluorescent calcium indicator (OGB-1 or Fluo-4) and Alexa 594 via a somatic recording pipette. All of the recorded neurons classified as a fast spiking interneurons, according to their passive and active parameters **(Table 1)** (Buhl et al., 1996, Lamsa et al., 2007, Hu et al., 2010, Avermann et al., 2012). The homogeneity of the neuronal population was supported by cluster analysis.

Table 1. Electrophysiological parameters used to classify the FS-PV INs (n=47) in accord with previous data (Buhl et al., 1996, Lamsa et al., 2007, Hu et al., 2010, Avermann et al., 2012).

	Frequency (Hz) during the first 100 ms	Frequency (Hz) during the last 100 ms	Adaptation	R_{in} (MΩ)	AP half width (ms)	τ (ms)	Resting membrane potential (mV)
Mean	221.79	197.44	0.88	73.08	0.35	7.82	-66.21
s.e.m.	11.88	12.29	0.02	6.29	0.02	0.72	0.52

DOI:10.14753/SE.2015.2055

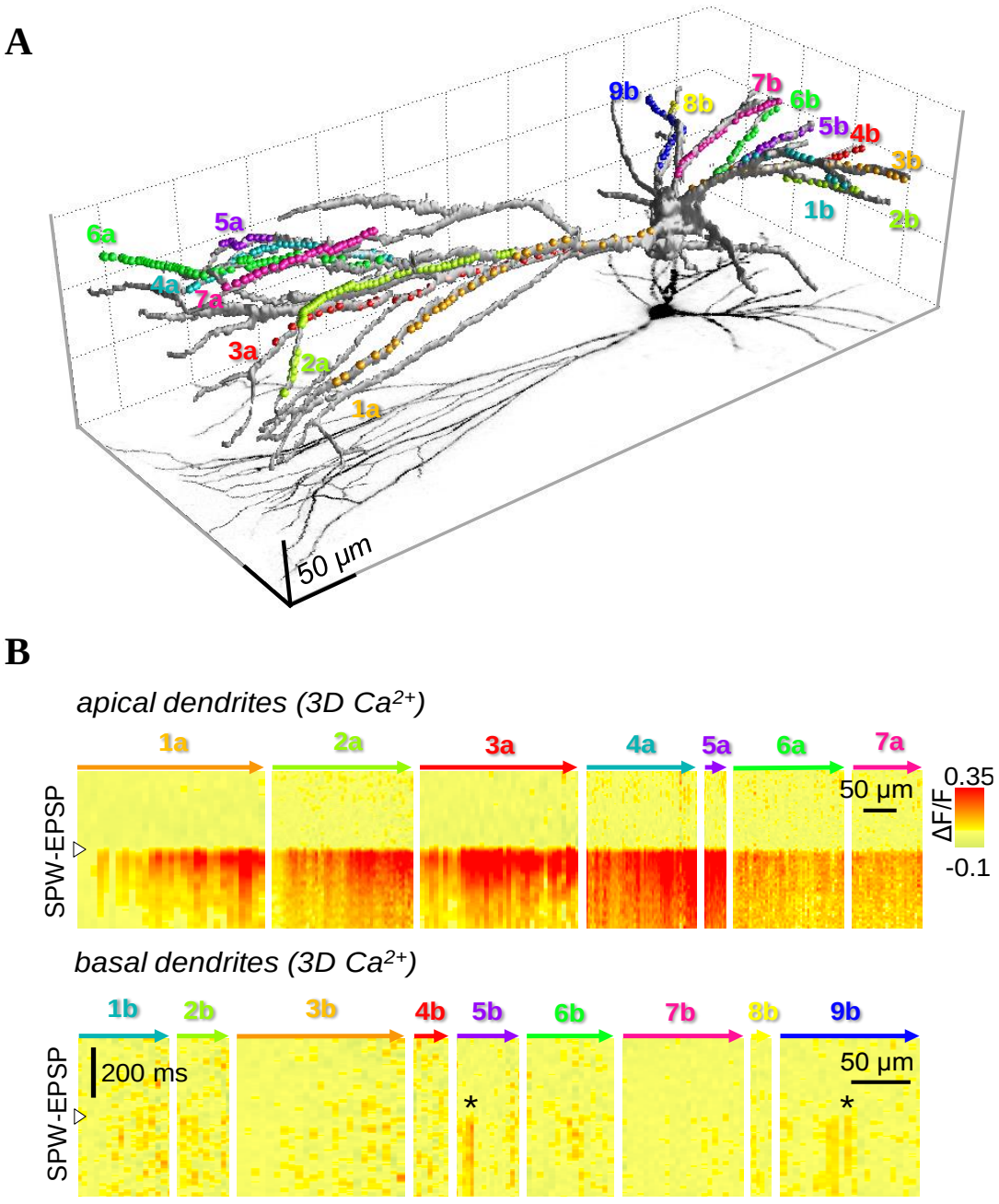

Figure 18. SPW-R associated dendritic spikes revealed by fast 3D-AO imaging in thin distal dendrites of FS-PV INs. A: Full dendritic arborization of an FS-PV IN imaged by 3D-AO scanning in the hippocampal CA1 region. Colored spheres represent locations selected for 3D trajectory scanning. **B:** SPW-EPSPs associated Ca^{2+} responses aligned to the peak of the EPSPs (average of five to nine responses). The 3D scanning trajectories cover the majority of the dendritic arbor, and the segments were imagined simultaneously in different combination in the apical (top) and the basal (bottom) regions. Numbered arrows correspond to segments in A and point distally. Asterisks indicate small compartmentalized synaptic responses.

DOI:10.14753/SE.2015.2055

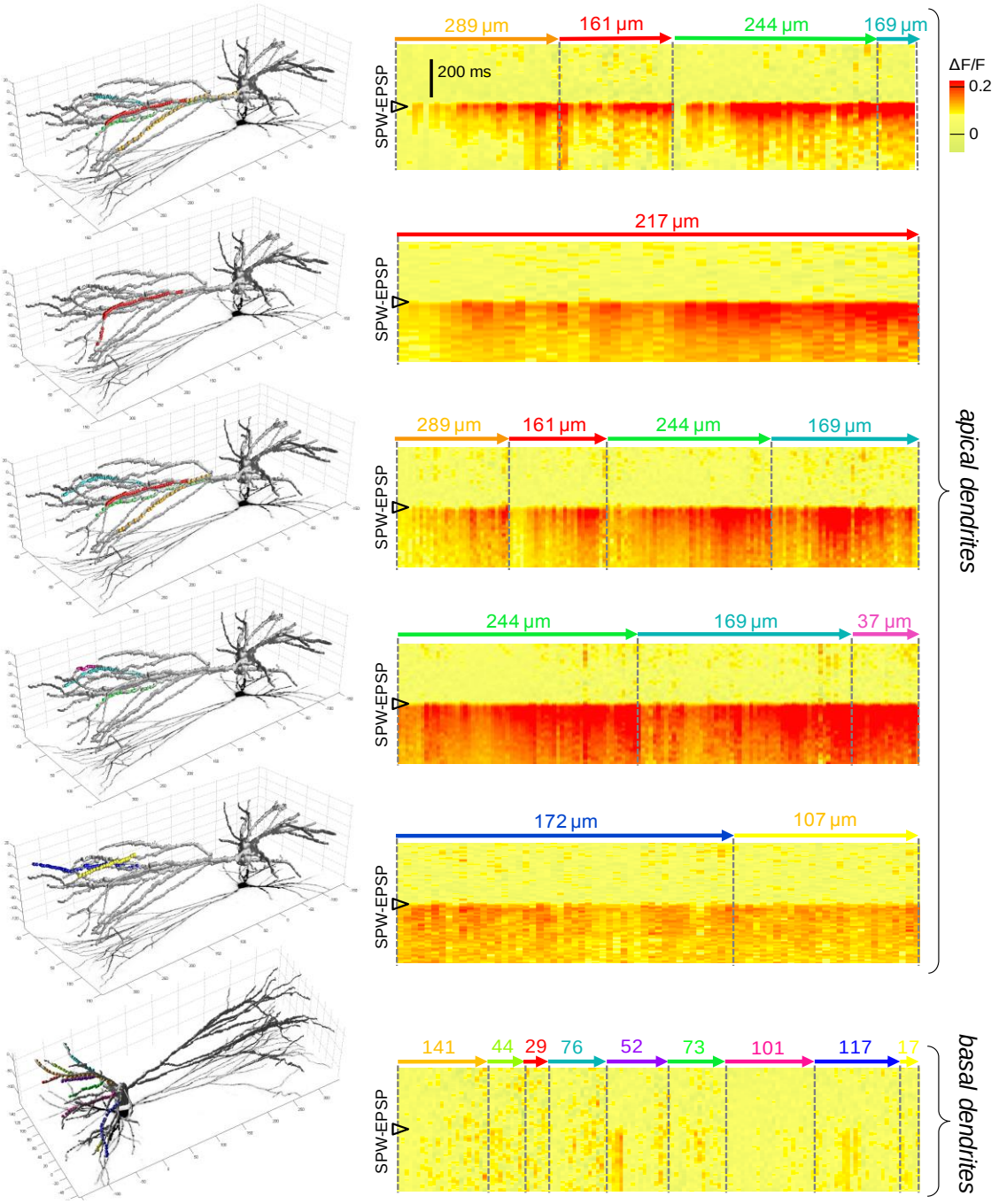

Figure 19. Fast 3D Ca^{2+} imaging of SPW-R-associated dendritic spikes in fine terminal dendrites of FS-PV INs. Six representative 3D measurements performed on the FS-PV IN used in Figure 18A during spontaneous SPW-R activities. (Left) Different combinations of dendritic segments were simultaneously measured in 3D as indicated by color-coded dots in the diagram of the cell. (Right) Corresponding 3D Ca^{2+} responses associated with SPW-EPSPs were measured simultaneously in the color-coded (arrows) dendritic segments (n=5-9 responses).

DOI:10.14753/SE.2015.2055

For 3D Ca^{2+} imaging reference z-stack was recorded in order to select multiple, long dendritic segements covering the majority of the dendritic arbor. Simultaneous trajectory scanning in 3D was performed along the multiple dendritic segments during SPW-R activity **(Figure 18A)**. The 3D Ca^{2+} responses were spatially normalized and projected in 2D **(Equation 1 and 2, Figure 18B)** in several combinations (**Figure 19**).

According to the previous published data (Hu et al., 2010, Topolnik, 2012, Hu et al., 2014), somatically evoked bAP Ca^{2+} signals in FS-PV IN dendrites show non-uniform manner and decreased below the recording threshold at a short distance from the soma (113.88±14.50 µm, n=13) (**Figures 20A-F, 21A and Movie 2)**. In our experiments, 5bAPs were evoked between two SPW-R events at 40 Hz (**Figure 19B**). These data support the passive nature of FS-PV INs which could be explained by the high K^+ to Na^+ conductance ratio along the dendrites (Hu et al., 2010, Norenberg et al., 2010).

DOI:10.14753/SE.2015.2055

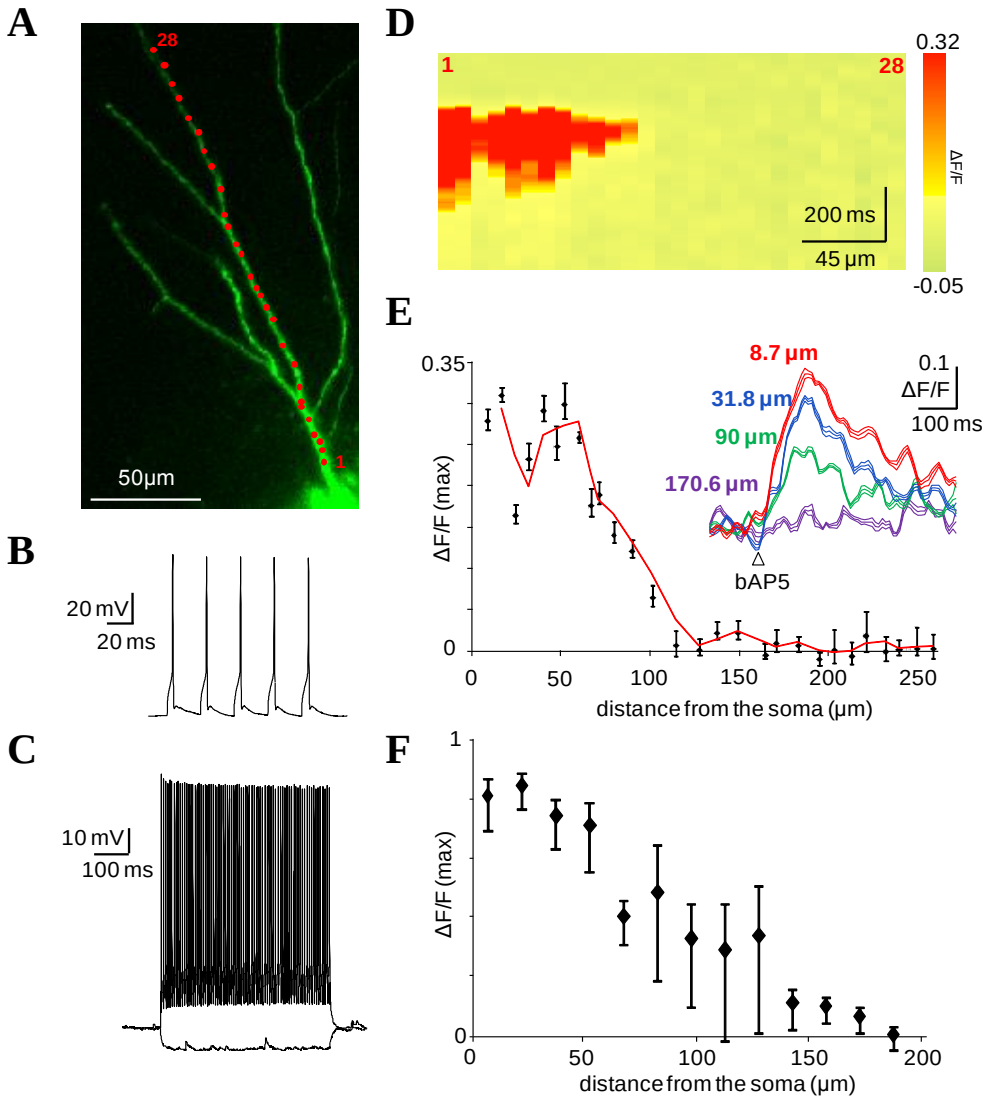

Figure 20. Rapid attenuation of bAP-induced Ca^{2+} responses in FS-PV IN dendrites. A: Maximum intensity z-projection image of a long dendritic segment of an FS-PV IN imaged using 3D acousto-optical scanning in the hippocampal CA1 region. The 28 red points were selected for 3D random-access trajectory scanning. **B:** A somatic membrane potential response induced by a burst of five APs. **C:** Representative current steps-induced somatic voltage responses in FS-PV INs used for characterization. **D:** Five bAP-induced 3D Ca^{2+} responses (average of n=5 transients) recorded at the red points in A. **E:** Mean amplitude of the Ca^{2+} responses as a function of distance along the dendrite (mean±s.e.m., n=5 measurements). Inset: Ca^{2+} transients derived from the 3D Ca^{2+} response in B at different dendritic distances (mean±s.e.m., n=5 measurements). **F:** Average amplitude (mean±s.e.m.; n=21 cells) of five bAP-induced Ca^{2+} responses as a function of dendritic distance from the soma. Responses were induced in the FS-PV INs used to characterize these cells.

DOI:10.14753/SE.2015.2055

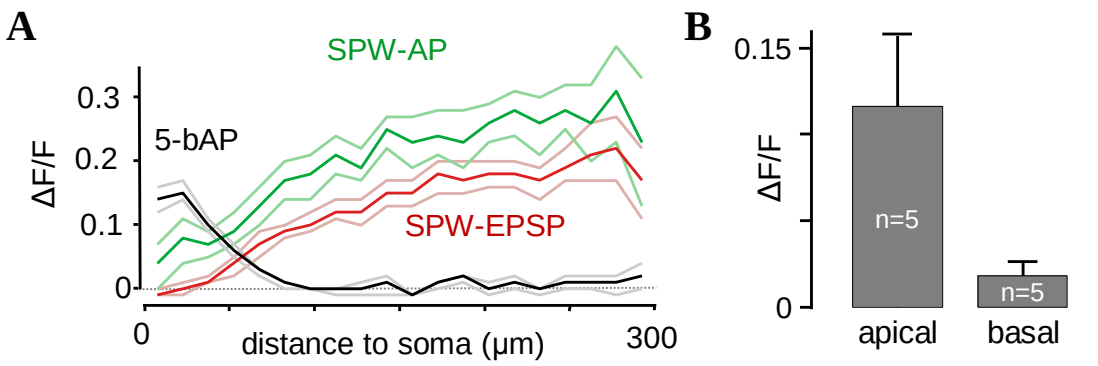

Figure 21. Spontaneous SPW-R associated Ca^{2+} signals in apical and basal dendrites of FS-PV INs. A: Average SPW-EPSP-induced (red), SPW-AP-induced (green, with 1 AP), and somatically evoked backpropagating AP-induced (black, 5 AP) 3D Ca^{2+} responses as a function of distance from the soma. Mean ± SEM, n=5 cells. **B:** Average apical and basal dendritic Ca^{2+} signals during SPW-EPSP (mean ± SEM, n=5 cells).

In contrast to somatically evoked bAPs the spontaneous SPW-R related AP (SPW-APs) calcium signals increased as a function of a distance from the soma (**Figure 21A** green and **Movie 3**). Furthermore the somatically recorded subtreshold events related SPW-R (SPW-EPSPs) show similar features (**Figure 21A** red). In both cases the 3D Ca^{2+} responses were close to zero at the soma, suggesting dendritic origin for these signals. Complementary distributions of SPW-APs, SPW-EPSPs Ca^{2+} versus bAPs are represented along the apical dendrite (**Figure 21A and Movie 4**). In our *in vitro* preparations, SPW-EPSP-associated network activities which induced locally clustered responses, termed dendritic hot-spots (FWHM: 3.73±0.13 μm; **Figure 22A-D**), was also able to generate more generalized signals, which invaded continuous dendritic segments of the distal apical, but not the basal dendritic arbor (**Figure 18B and Figure 21B**).

DOI:10.14753/SE.2015.2055

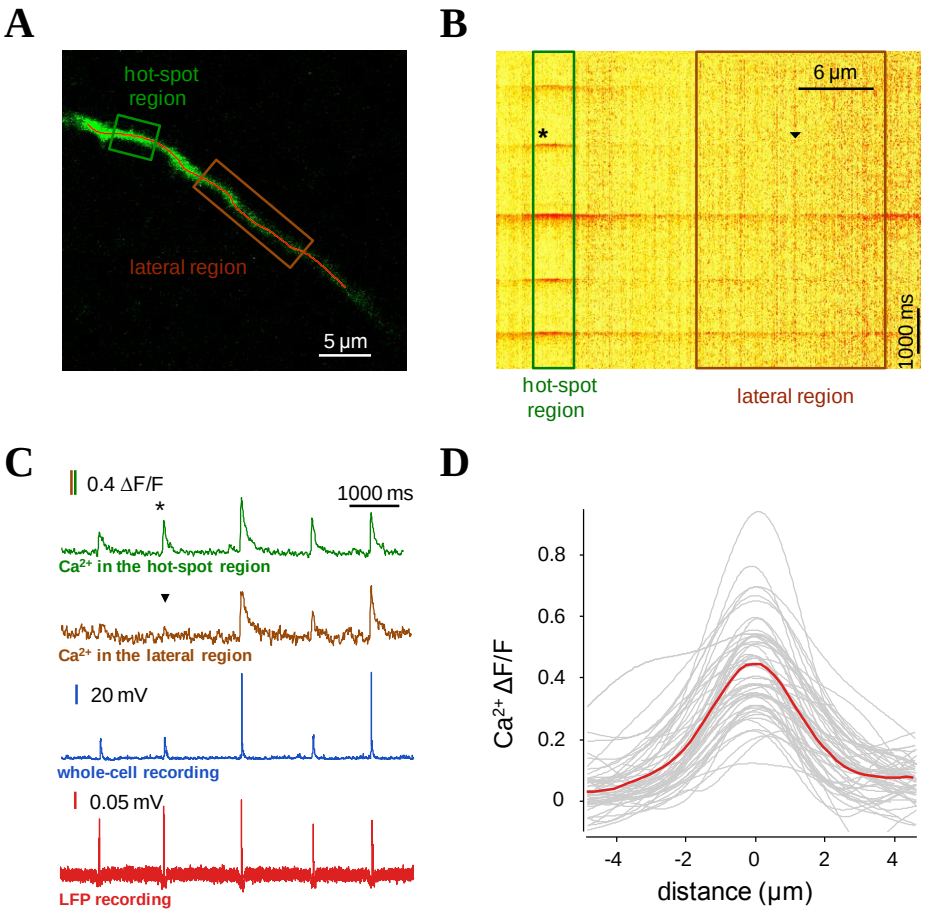

Figures 22. Dendritic hot-spots during SPW-R activities. A: Z-stack of a dendrite of an FS-PV IN. **B:** Ca^{2+} response measured along the red line in A. **C:** Ca^{2+} transients are spatial averages of the Ca^{2+} responses measured in the color-coded boxes in B. Simultaneously recorded somatic whole-cell and LFP recordings are shown in blue and red, respectively. Note the localized Ca^{2+} response (asterisk) which does not propagate to the neighboring lateral dendritic segment. **D:** Spatial distribution of SPW-EPSP-associated dendritic hot-spot responses in 9 cells.

The SPW-EPSP 3D calcium signals show reciprocal distance-dependent distributon compared to the somatically evoked bAPs (**Figure 21A**). Moreover when the SPW-EPSPs were combined with APs to generate SPW-APs, they give a large and more distributed calcium signals along the dendritic arbor (**Figure 21A**). These data support the idea that the passive FS-PV INs can switch from a ground state to an excited, active state when the neuronal networks are active generating a changed dendritic integration status. Thus these data support that at the excited state,

DOI:10.14753/SE.2015.2055

regenearative dendritic activities, such as propagating dendritic Ca^{2+} spikes, could occur.

In order to test this hypothesis, we have established a set of criteria based on previous definitions (Stuart, 1999, Losonczy and Magee, 2006, Katona et al., 2011), the fulfillment of which strongly indicates that there is a dynamic switch in integration mode, and that dendritic spikes are generated in FS-PV INs during SPW-Rs:

(1) *spikes are detectable in the membrane potential signal*;
(2) *spike initiation is dendritic in origin*;
(3) *spikes actively propagate into neighboring dendritic segments*;
(4) *spikes are initiated in an all-or-nothing manner above a well-defined threshold*;
(5) *and spikes are mediated by voltage-gated ion channels*.

I address these criteria in detail in the following sections.

DOI:10.14753/SE.2015.2055

4.3. Dendritic spikes are associated with membrane potential oscillation called interneuronal ripple oscillation

To address the first criteria somatic membrane potential activities were simultaneously measured during the 3D Ca^{2+} imaging and SPW-R recordings (**Figure 23**). The Ca^{2+} signal amplitude in average was well-correlated with the amplitude of the subtreshold somatic activity induced by SPW-EPSPs (r=0.84) and with the numbers of the SPW-APs (**Figure 24A**). SPW-EPSPs with amplitudes below the mean EPSP amplitude (small SPW-EPSPs) induced significantly smaller responses than the ones with amplitudes larger than the mean (large SPW-EPSPs). In these suprathreshold cases, the average Ca^{2+} responses were proportional to the number of APs. In contrast, the single data showed great variability, some case the calcium amplitude was higher at a SPW-EPSP than at a SPW-AP in the same dendritic region (**Figure 23A-B**). The Ca^{2+} signal amplitude accompanied specifically with larger SPW-EPSPs with long oscillating plateau-potentails than SPW-APs (**Figure 23B-C**). This oscillating-like behavior was revealed by our baseline subtracted method and with short time Fourier transform (spectrograms) of somatic membrane potential. The oscillation frequencies were at ripple range, therefore these oscillations were named as *interneuronal ripple acitivities*. The oscillation frequency was rapidly increased before the SPW-EPSP peak, it reached the maxima at the peak (fmax 270.3±18.18 Hz, n=11) and slowly decresed after the peak (239.97±19.25 Hz), while its duration extended 17.1±3.19 ms beyond the termination of the network LFP signal (LFP FWHM 12.23±1.85 ms, EPSP FWHM 29.37±2.49 ms, p=0.0001) (**Figures 23C and 25A-B**). The somatically recorded interneuronal ripple acitivties could occur even whereas the LFP activities were terminated (**Figure 25**). The membrane potential oscillations on the plateau were more elongated than the simultaneously recorded LFP oscillations; they indicate the intrinsic oscillatory properties of the FS-PV INs.

DOI:10.14753/SE.2015.2055

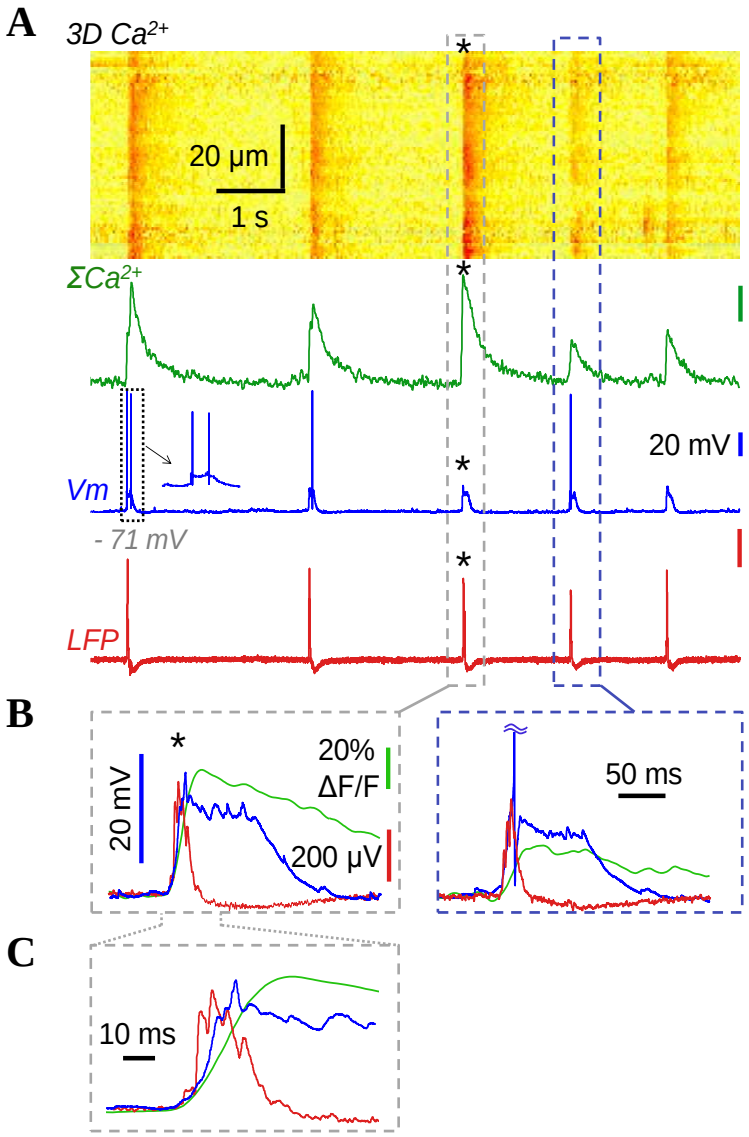

Figure 23. SPW-associated dendritic spikes and interneuronal ripple oscillations. A: Representative 3D Ca^{2+} response (top) recorded during five successive SPW-R events in a single, long dendritic segment shows that Ca^{2+} signals invade the full apical dendritic segment both in the presence and absence (asterisks) of somatic APs. The spatially integrated dendritic Ca^{2+} response (green) is shown with the simultaneously recorded somatic membrane (blue) and CA1 local field potentials (red, str. pyramidale). **B:** Overlaid Ca^{2+} (green), LFP (red), and whole-cell membrane potential (blue) traces from the two boxed areas in A. **C:** Traces in B shown at a higher magnification.

DOI:10.14753/SE.2015.2055

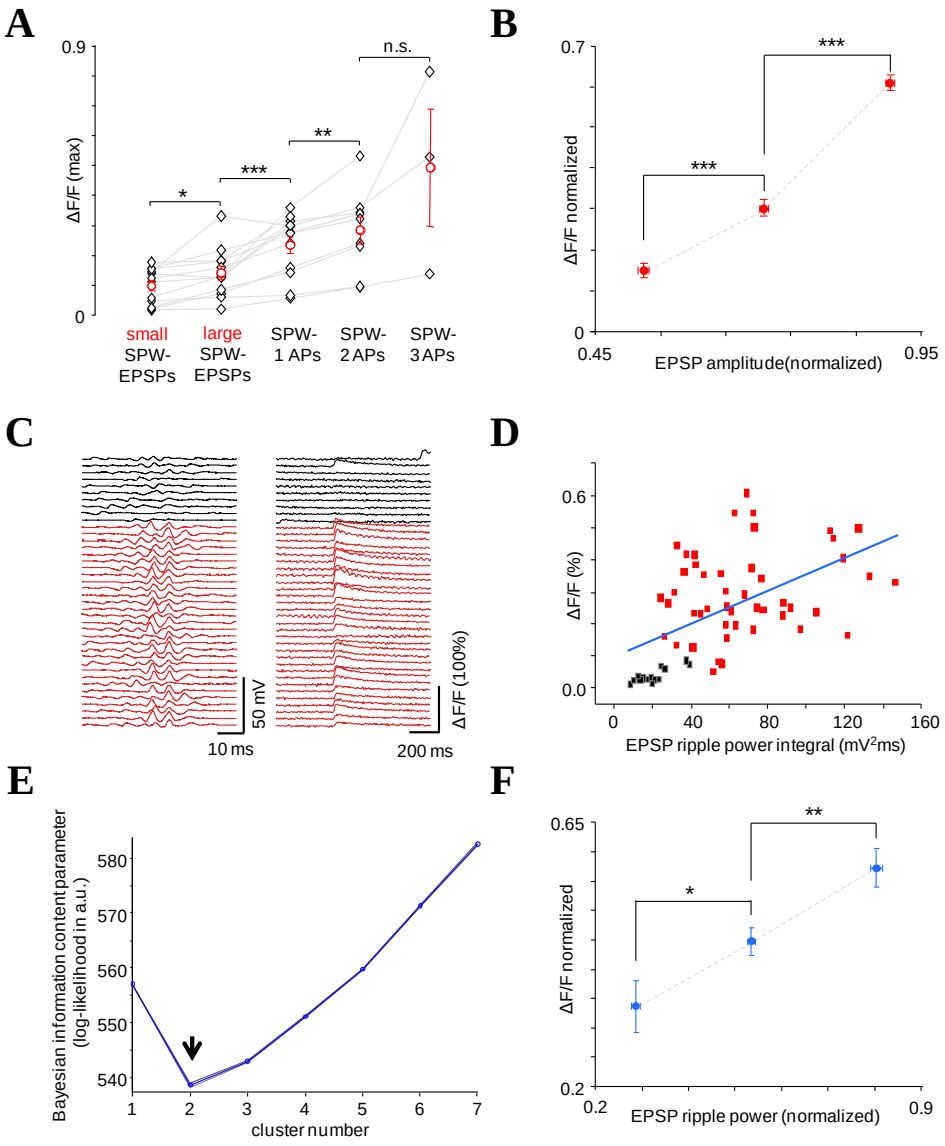

Figure 24. Correlation of interneuronal ripple oscillations and dendritic Ca^{2+} responses during SPW-Rs. A: Average dendritic SPW-EPSPs and SPW-AP-associated Ca^{2+} responses recorded in different neurons (gray lines). Mean±s.e.m. are in red. Asterisks indicate significance (n.s., non-significant). **B:** Peak of the average SPW-EPSP-associated dendritic Ca^{2+} transients as a function of EPSP amplitude (n=5 cells). **C:** (Left) Further representative individual SPW-EPSPs with (red) and without (black) interneuronal ripple oscillations and corresponding average dendritic Ca^{2+} transients (right). **D:** Peak of the average dendritic Ca^{2+} signal plotted against the power integral of the baseline-subtracted voltage traces. Blue line shows linear fit. **E:** Gaussian mixture distribution parameter estimates. Traces are mean±s.e.m. **F:** Peak of the average SPW-EPSP-associated dendritic Ca^{2+} transients (mean±s.e.m, n=5 cells) as a function of the power amplitude of interneuronal ripple oscillations.

DOI:10.14753/SE.2015.2055

Moreover, in over 50% of the cells, I simultaneously recorded individual SPW-EPSPs and LFP traces whose phases, frequencies, and amplitudes did not correlate, despite the fact that the average SPW-EPSP and LFP signals correlated well (**Figure 26**). These data also suggested that intrinsic membrane mechanisms may contribute to the generation of the dendritic Ca^{2+} spikes and accompanying interneuronal ripple oscillations; therefore, I further investigated the relationship between the oscillations and Ca^{2+} responses.

The amplitude of SPW-EPSP associated Ca^{2+} responses were well-correlated with the power of the interneuronal ripple oscillations in spatial averages across dendrites and in individual dendritic segments (**Figure 27 and Figure 28,** r=0.59). The correlation showed a continous distribution. At the same time a subgroup of SPW-EPSPs with no interneuronal ripple oscillations and with small Ca^{2+} responses could be separated with cluster analysis (**Figure 24C-E**). Cluster analysis revealed two clusters of responses.

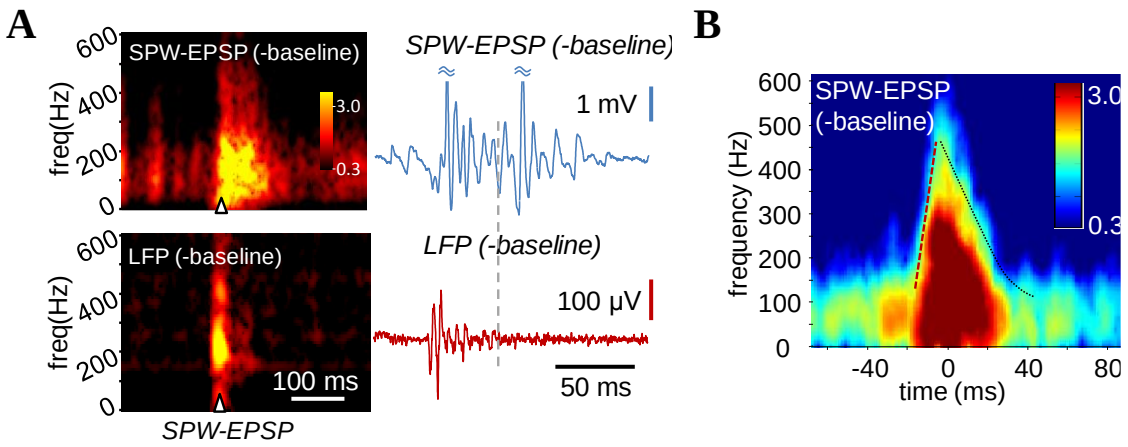

Figure 25. The membrane potential oscillations on the plateau were more elongated than the simultaneously recorded LFP oscillations. A: Left, averaged spectrograms of baseline-subtracted SPW-EPSPs and LFPs (n=7). Right: representative individual traces after baseline subtraction are shown on the same timescale. **B:** Spectrogram of peak-aligned and averaged SPW-EPSPs (n=7 measurements). Red dashed lines indicate the rapid frequency increase just before the EPSP peak. The black dotted line shows a more elongated frequency decrease in the high frequency band after the EPSP peak. The zero time indicates the peak of the EPSPs.

DOI:10.14753/SE.2015.2055

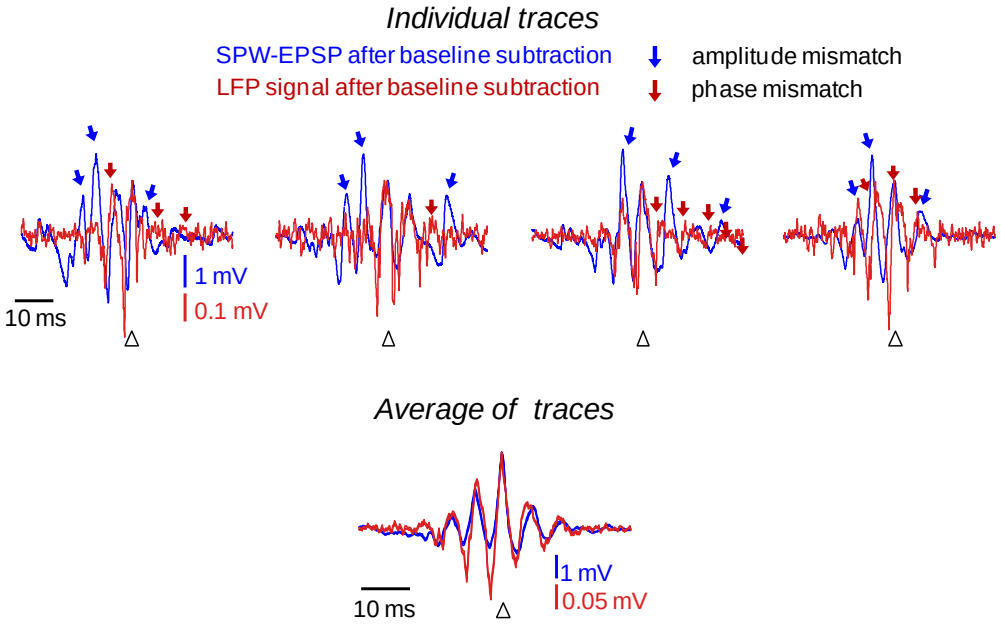

Figure 26. Individual SPW-EPSPs (blue) and LFP signals (red) recorded simultaneously in an FS-PV IN and shown at a similar scale. The baselines were subtracted using the baseline subtraction method, as before. Note the amplitude (blue arrows) and phase (red arrows) mismatches between the SPW-EPSP and LFP traces. (Bottom) Average (mean ± s.e.m) of 20 traces recorded in the FS-PV IN. Note that averaging eliminated the amplitude and phase mismatches.

In the first cluster (red), high amplitude ripple oscillations were accompanied by high amplitude Ca^{2+} signals. However, in the second cluster (black), no oscillations could be detected and the corresponding Ca^{2+} signal was close to zero (**Figure 24D-E**). By using Expectation Maximization (EM) algorithm for different component numbers (Schwarz, 1978, McLachlan and Peel, 2000) on the data set from **Figure 24C,** we found that the optimal cluster number is two (**Figure 24E** black arrow): the elements of the two clusters are shown in **Figure 24B**. Ca^{2+} signals with no ripple oscillations did not show expanded location, remained well-localized, small responses (**Figure 27**). With peak aligned and baseline subtraction it appearent that the interneuronal ripple activities showed similar frequency and phase values in both cases, SPW-EPSPs and SPW-APs (239.97±18.35 Hz and 239.70±11.00 Hz, respectively, $p>0.3$, $n=10$) (**Figure 29A-B**). On the other hand the output of the cells were precisely phase locked to the peak of the interneuronal ripple activites, indicating that the dendritic spikes induced by

DOI:10.14753/SE.2015.2055

synchronized network activities could transiently switch the input-output transformation function of FS-PV INs from the well-characterized sub-millisecond precision of EPSP-AP coupling to a slower integration scale, where interneuron output is gated in phase synchrony with interneuronal ripple oscillations (**Figure 29C**).

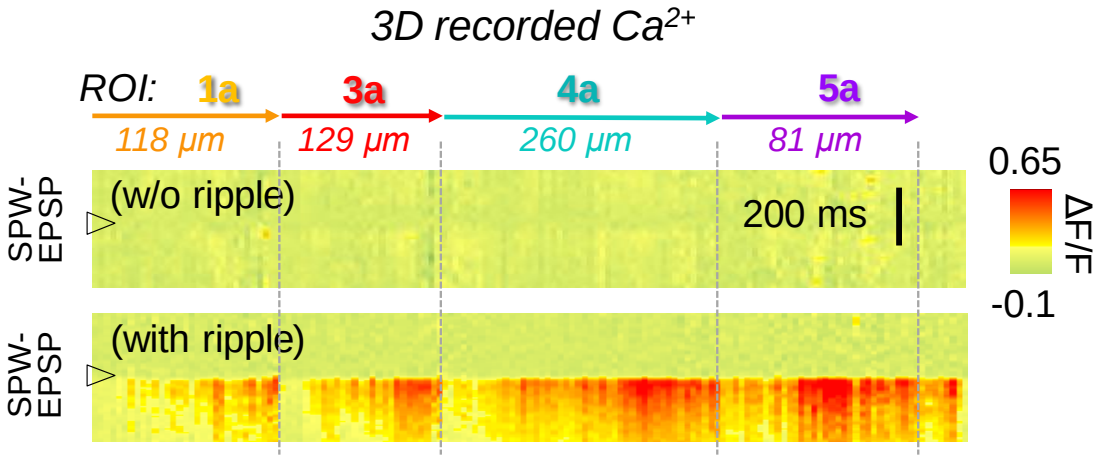

Figures 27. Dendritic spikes are associated with interneuronal ripple oscillations. The subgroup of SPW-EPSPs with interneuronal ripple oscillations (with ripple) induced larger 3D Ca^{2+} responses than those without oscillations (w/o ripple) in apical dendrites of an FS-PV IN.

DOI:10.14753/SE.2015.2055

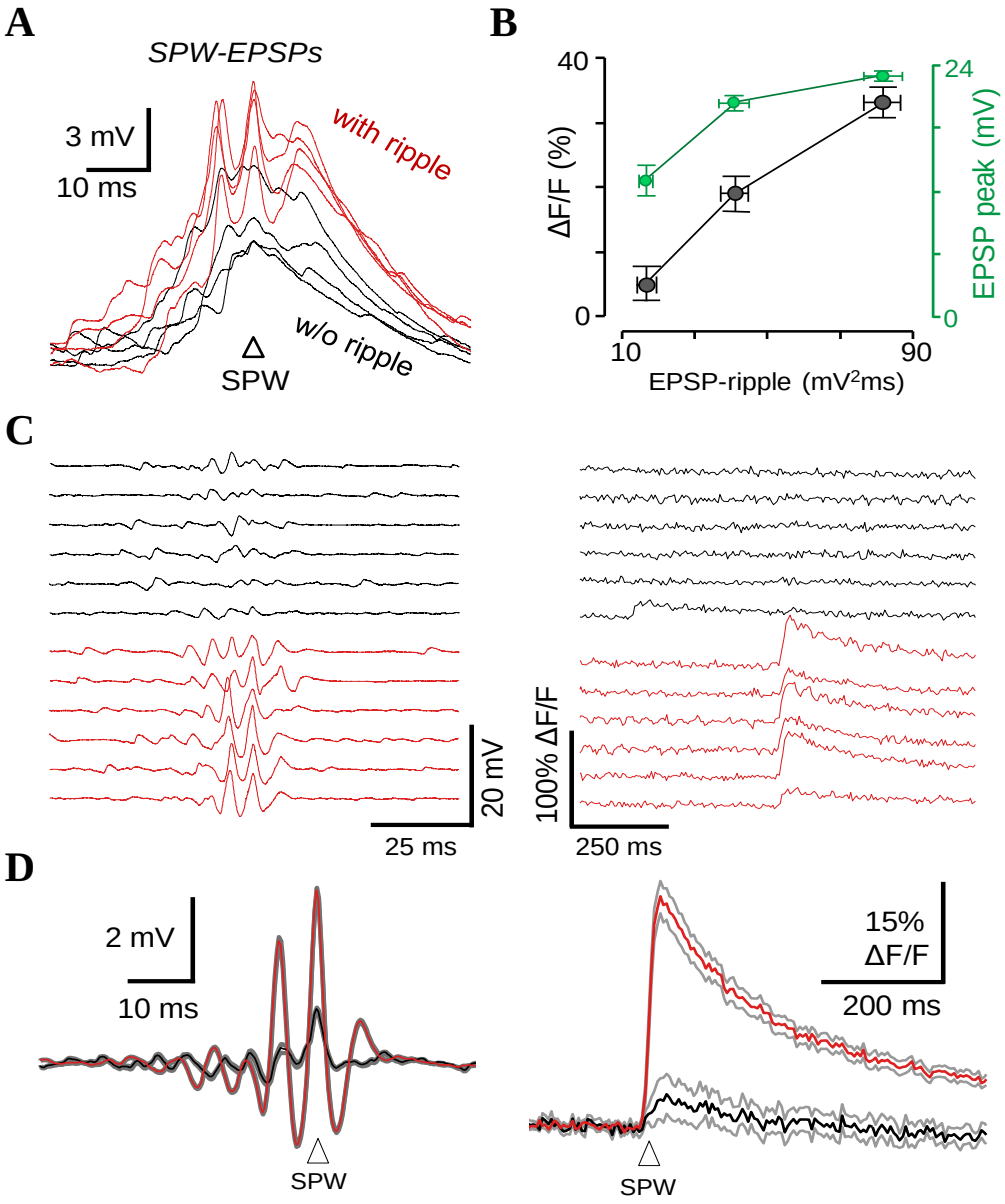

Figure 28. Dendritic spikes are associated with interneuronal ripple oscillations. A: Representative SPW-EPSPs with (red) and without (black) interneuronal ripple oscillations. **B:** Average dendritic Ca^{2+} transients (black) and simultaneously-recorded EPSPs (green) as a function of the power of interneuronal ripple oscillations. **C:** Left: Individual SPW-EPSPs after baseline subtraction with (red) and without (black) oscillations. Right: Corresponding dendritic Ca^{2+} transients. **D:** Left: peak-aligned oscillating (red) and non-oscillating (black) SPW-EPSPs after baseline subtraction (mean ± s.e.m.; n=30). Right: corresponding mean dendritic Ca^{2+} transients.

DOI:10.14753/SE.2015.2055

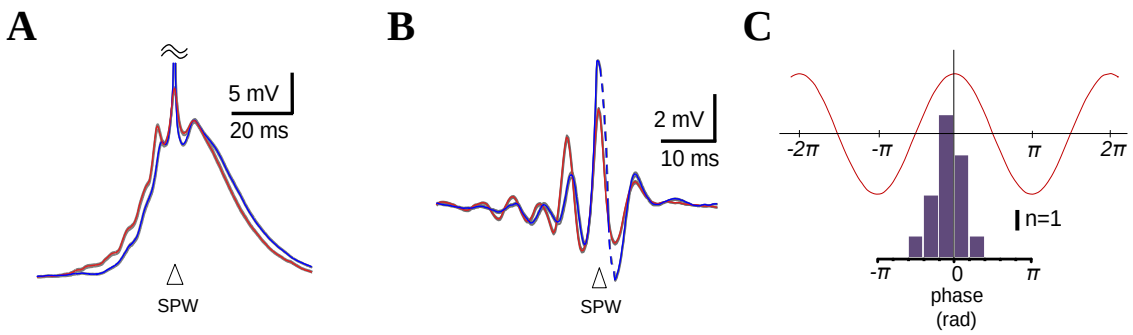

Figure 29. FS-PV IN output is gated in phase synchrony with interneuronal ripple oscillations. A: Average SPW-APs (blue) and SPW-EPSPs (red) showing similar interneuronal ripple oscillations. (mean ± s.e.m.; n=30). Triangle indicates the peak of the SPW-R event. **B:** The same as A, after baseline subtraction. **C:** Binned firing probability relative to the phase of the interneuronal ripple oscillations (n=17 cells).

4.4. Characteristics of SPW-R associated dendritic Ca^{2+} spikes

To answer the second criteria, high-speed 3D scanning was used to define the dendritic origin of the Ca^{2+} spikes (**Figure 30**). Simultaneously scanned, long apical dendrites of the FS-PV INs in the distal zone, up to 308 µm from the soma in order to avoid the effect of the bAPs (where the bAPs responses were below the detection threshold). Large 3D Ca^{2+} responses were detected during both SPW-EPSPs and SPW-APs as well. This Ca^{2+} invades the whole apical dentritic region with non uniform manner. There were several local maxima along the apical arbor where the Ca^{2+} signal amplitudes were significantly higer, called hot-spots (**Figures 30 and 31**). The relevance of hot-spots is further supported by the fact that, although the occurrence of APs boosted the dendritic 3D Ca^{2+} response in the measured distal segments evenly by 41.3%±2.9% (n=5 cells over 150 µm distance), the location of hot-spots also remaind well-preserved in this supratreshold case (**Figure 30**).

To avoid the bAPs putative effects from this experiment [Ca^{2+}] which was associate SPW-EPSPs only was measured. In these hot-spots the Ca^{2+} responses were not only larger than the [Ca^{2+}] record in the neighboring dendritic segment (333% ±51%, n=17 regions in n=9 cells), but emerge earlier at 12.8±2.4 ms (41.5±12.7 µm from the center of the hot-spot), indicating that the hot-spots are the initiation site of the

DOI:10.14753/SE.2015.2055

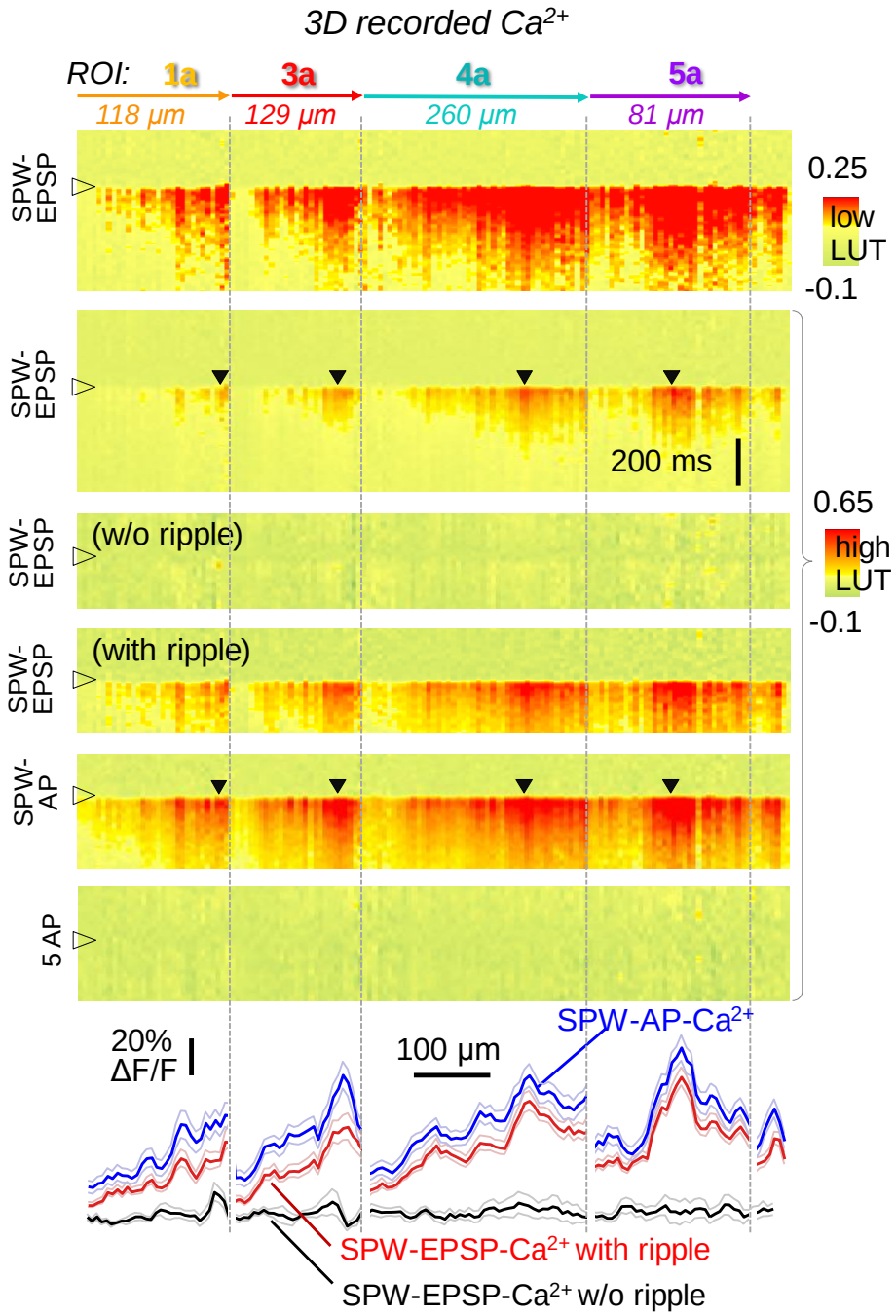

Figure 30. Dendritic spikes are initiated in multiple hot-spots during SPW-Rs. Top: Average SPW-EPSP-, SPW-AP-, and bAP-associated 3D Ca^{2+} responses, recorded simultaneously in the apical dendritic segments in Figure 18A. The look-up table with high ΔF/F values (high LUT) revealed hot-spots (black triangles). The subgroup of SPW-EPSPs with interneuronal ripple oscillations (with ripple) induced larger 3D Ca^{2+} responses than those without oscillations (w/o ripple). In these distant dendritic locations, five bAPs (5 bAP) did not induce any response. Bottom: spatial distribution of peak 3D Ca^{2+} responses (mean ± s.e.m.).

DOI:10.14753/SE.2015.2055

dendritic calcium spikes (**Figure 31A**). I analysed this with the previously developed temporal super-resolution method (Katona et al., 2012). Several hot-spots were identified along the apical dendrites. The Ca^{2+} spike invade both centripetally and centrifugally from the hot-spots. Supporting the regenerative nature of the dendritic spikes, the propagation speed from the hot-spots toward lateral dendritic segments could be clearly measured in 68.8±8.2 % of long dendritic segments (222.1±63.0 µm, n=13, **Figure 31B**), yielding an average propagation speed of 34.22±4.32 µm/ms, a substantially higher speed than that expected from diffusion (Goldberg et al., 2003a, Katona et al., 2011). These Ca^{2+} spikes which associated the SPW-EPSPs never propagated from the soma, suggesting their dendritic origin. These signals showed regenerative nature and actively propagated from dendritic hot-spots. With this, the third criterion was also answered revealing the regenerative, active characterisitcs of these events.

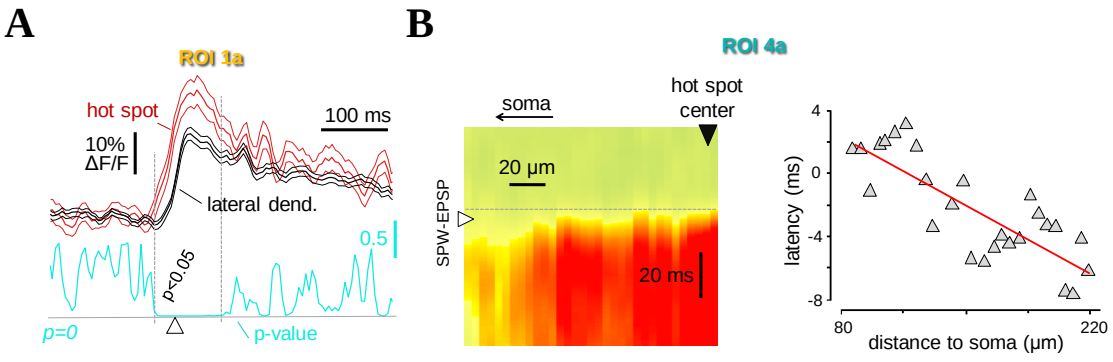

Figure 31. Properites of Ca^{2+} hot-spots and propagating dendritic Ca^{2+} spikes. A: The Ca^{2+} signal in the center of the hot-spot (red) in dendritic segment #1a in A was larger and significantly (cyan) preceded the Ca^{2+} signal of adjacent dendritic regions (black) in the rising phase (mean ± s.e.m.). Triangel indicates the center of the hot-spots. **B:** Left, propagation of the SPW-EPSP-associated Ca^{2+} spike from the center of the hot-spot of region #4a (example dendritic segments from the cell showed in Figure 18) toward the soma. Right, corresponding Ca^{2+} signal onset latency times. Red line is a linear fit (r=0.65).

DOI:10.14753/SE.2015.2055

4.5. Spatially and temporally clustered inputs generate the dendritic spikes

To answer the question of how many clustered excitatory inputs are needed to evoke a regenerative event in an all-or-nothing manner (fourth criterion), excitatory synaptic inputs were activated by using two-photon glutamate uncaging in temporally and spatially clustered patterns (Katona et al., 2011). To the better modeled the FS-PV IN dendritic mechanism conventional type submerged recording chamber was used for glutamate uncaging experiment and pharmacology to avoid high spontaneous activities in the networks. To reconstraction the large amplitude (29.37±2.49 ms, 22.6±1.63 mV, n=12) SPW-EPSP associated hot-spots and propagated calcium spikes from small unitary input (<1 mV) (Ali et al., 1998), tens of unitary inputs needed to be activated in a short time window. The widely used MNI-glutamate is too toxic to activate repetitively high number of inputs within 5-6 ms interval (the time window for ripple oscillations). Therefore we used another glutamate uncaging compound called DNI-glutamate•TFA (DNI-Glu•TFA), which has 7.17±0.84 times higher two-photon uncaging efficiency, thus we could evoke clustered input on FS-PV IN apical dendrites without a marked photodamage side-effect. It has been demonstrated earlier that the input-output transformation of the FS-PV INs is linear or sublinear (Hu et al., 2010, Norenberg et al., 2010). Other two groups showed the same mechanism in cerebellar neurons (Abrahamsson et al., 2012, Vervaeke et al., 2012). In contrast of this, I found that the uncaging evoked Ca^{2+} responses in the hot-spot-like regions showed a step-like nonlinear increase at a well defined active input number, identified the first threshold (11.04±1.4 active inputs, n=9 cells) (**Figure 32**). Ca^{2+} responses were evoked point by point by glutamate uncaging in a well-localized region of the dendrite. The single uncaging point represents single input, whose amplitude was previously defined (see methods). A modest increase at a slower rate was followed by a progressively increasing input number (**Equations 3 and 4**). SPW-R associated hot-spots in this way could be reproduced by glutamate uncaging. The first threshold was followed by a second one which was clearly visible outside the input zone (hot-spot-like zone) termed lateral dendritic region where the evoked Ca^{2+} responses show a sigmoid-like increase (**Figures 32D and 33**). The active input number at the second threshold was 30.3±4.0 (range 10-47 n=9 cells). As the average release probability of excitatory synapses onto

DOI:10.14753/SE.2015.2055

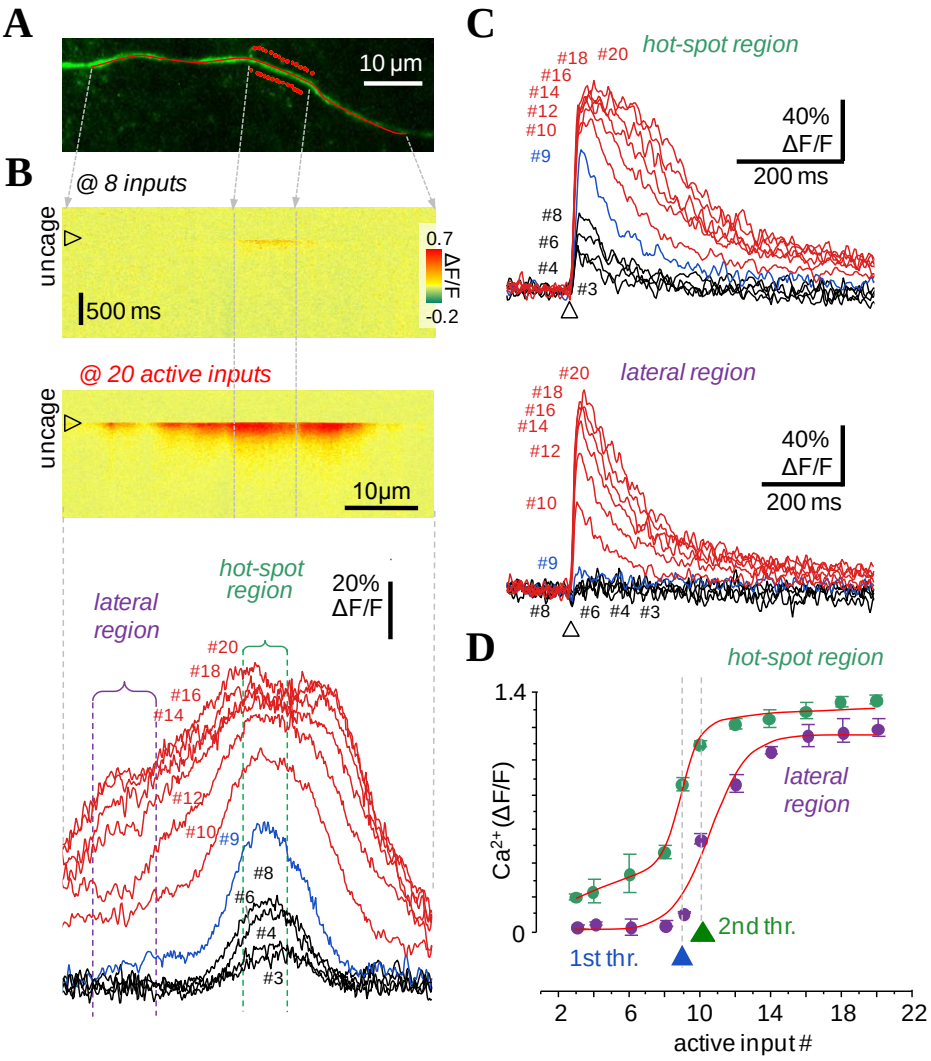

Figure 32. Synchronous activation of clustered glutamatergic inputs reproduces SPW-R-associated dendritic Ca^{2+} spikes. A: Maximum intensity z-projection image of a dendritic segment of an FS-PV IN. Red points are active input locations used for patterned two-photon glutamate uncaging in the presence of DNI-Glu•TFA. Uncaging-evoked Ca^{2+} responses measured along the red line in A, and the corresponding somatically-subthreshold EPSPs below the first threshold (black), at the first threshold (blue), and above the second threshold (red). **B:** Average Ca^{2+} responses (n=5) induced by uncaging with a near-subthreshold number of active inputs (top), and at a suprathreshold number of active inputs (middle). (Bottom) Spatial distribution of the peak Ca^{2+} responses at an increasing number of active inputs. **C:** Ca^{2+} transients derived at the hot-spot (top) and at the lateral dendritic (bottom) regions in B at an increasing number of active inputs. **D:** Mean peak Ca^{2+} responses (n=4 measurements). Boltzmann fits are shown in red. Note the sharp increase at the first and second thresholds in the hot-spot and lateral dendritic regions, respectively.

DOI:10.14753/SE.2015.2055

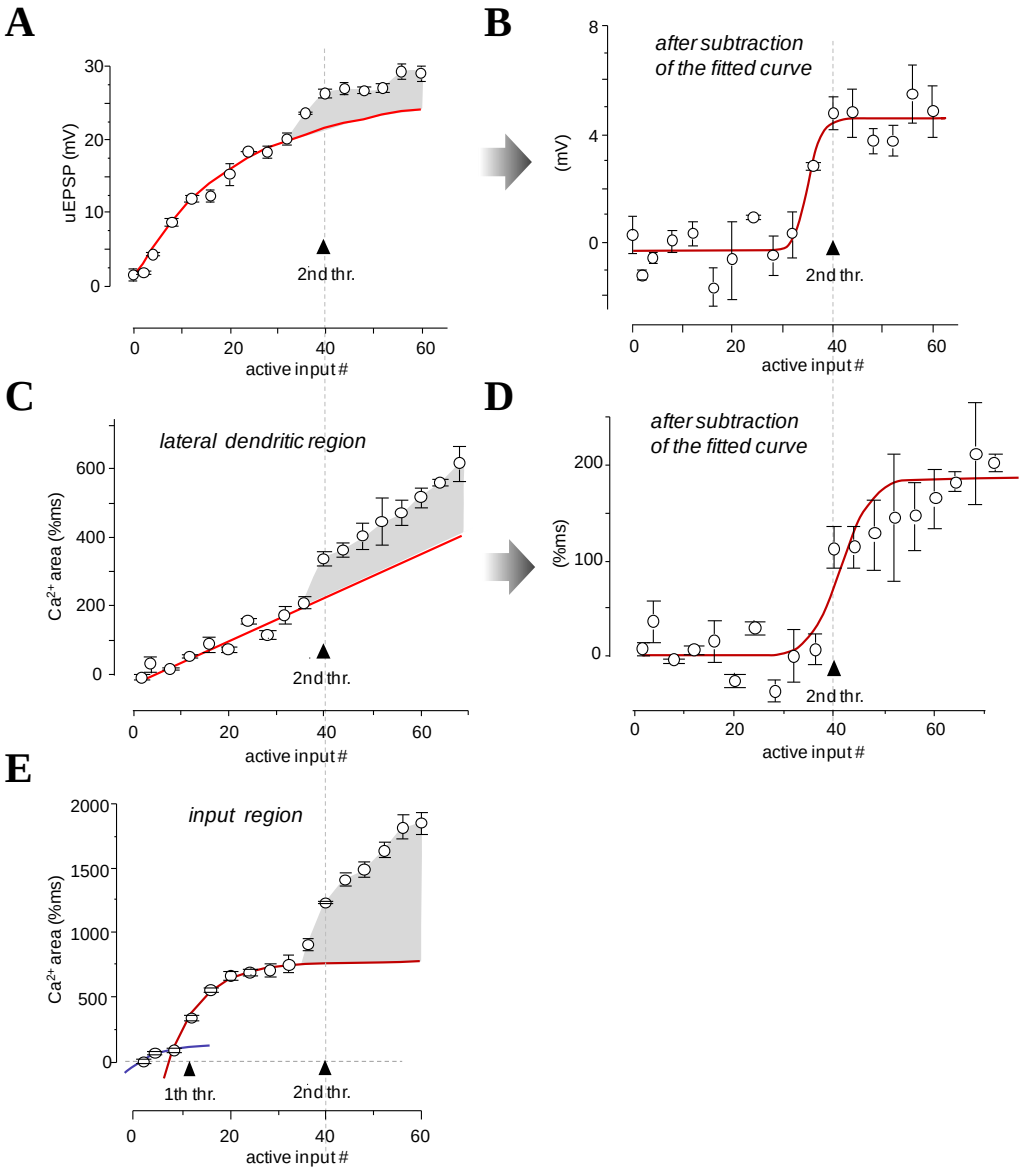

Figure 33. Nonlinear input-output functions of a representative FS-PV IN where a dendritic spike occurred at relatively high input numbers. A: Somatic EPSP amplitudes induced by a clustered uncaging pattern (uEPSP) plotted against the number of inputs. **B:** The same as in A, but after subtracting the result of the exponential fit. Red line indicates a fit derivated from Boltzmann equation (Equation 3) **C:** The area of the corresponding Ca^{2+} responses (mean ± s.e.m.) plotted against the number of inputs. Red line shows a linear fit to points below the threshold. **D:** The same as in C, but after subtracting the result of the linear fit. Red line indicates a fit obtained using Boltzmann equation (Equation 3). **E:** The area of the corresponding Ca^{2+} responses (mean±s.e.m.) in the input region plotted against the number of inputs. Red line shows an exponential fit using Equation 2 (r=0.98). Similarly to other neurons, the first threshold is visible only in the input region.

FS-PV INs is 0.75±0.19 (Gulyas et al., 1993), the first and second threshold of active input numbers correspond to the activation of around 15 and 40 release sites, respectively. The simultaneously-recorded somatic membrane potential remained below the AP threshold.

4.6. Characteristics of uncaging evoked dendritic Ca^{2+} spikes

The uncaging evoked dendritic Ca^{2+} therefore could be separated to two parts a hot-spot like input region where activated synapses were localized and a lateral dendritic region where spike propagation speed could be measured. The spatial distribution of the Ca^{2+} increase in the lateral dendritic regions showed a plateau-like characteristic above the second threshold. The amplitude of the Ca^{2+} plateau was slightly decreased as a function of a distance from the input region. Large, propagating Ca^{2+} signals were recorded similarly as spontaneous SPW-EPSP associated Ca^{2+} showed (**Figures 30 and 31**). The propagation speed could also be estimated resulting in 17.4±3.6 µm/ms in 85.1±16.4 µm-long dendritic segments (n=5 cells **Figure 34**), which speed is similar to the propagation speed of the large, spontaneous SPW-EPSP-associated dendritic 3D Ca^{2+} responses (**Figure 31B**). The small difference in the propagation speed between spontaneous SPW-EPSP-associated Ca^{2+} responses and uncaging-evoked Ca^{2+} signals could be explained by the lack of activated synaptic inputs in the lateral dendritic regions upon uncaging, which may decrease the local voltage. Indeed, Ca^{2+} responses were larger when the activated inputs were more widely distributed along the dendrite (see later: **Figure 38**). These data are in good agreement with the increase in the amplitude of backpropagating AP-associated Ca^{2+} responses during SPW-Rs (**Figure 21A**), when many synchronous dendritic inputs were arrived.

DOI:10.14753/SE.2015.2055

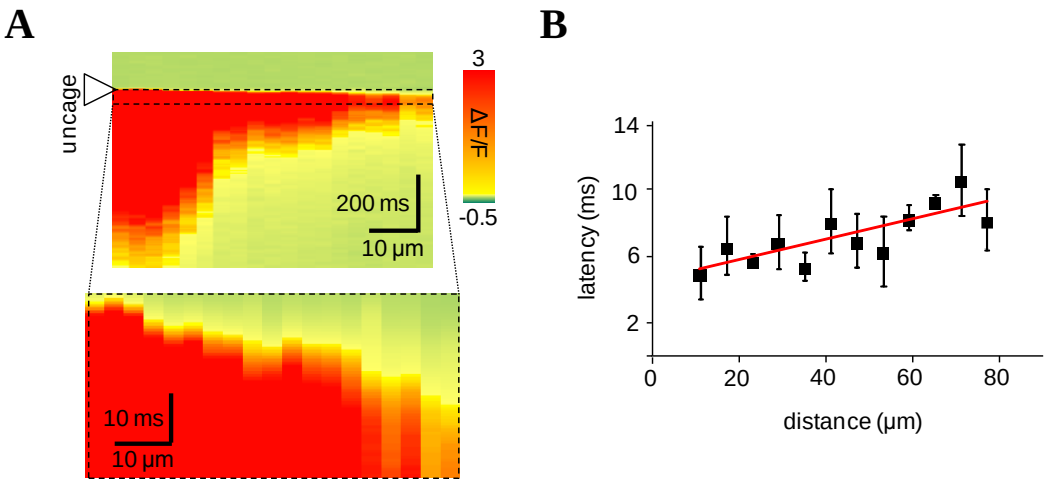

Figure 34. Properites of uncaging evoked dendritic Ca^{2+} hot-spots and propagating Ca^{2+} spikes. A: Propagation of an uncaging-evoked dendritic spike from the border of a hot-spot region to the lateral direction. **B:** Corresponding Ca^{2+} signal onset latency times. Linear fit is shown in red.

4.7. Activation of a short dendritic segment by glutamate uncaging can generate interneuronal ripple oscillation

The input-output characteristic of FS-PV INs was investigated to understand what the connection is between the Ca^{2+} spikes and the somatically recorded membrane potential. Until the second threshold the amplitude of the uncaging evoked EPSPs were showed similar step–like increasing manner - like the Ca^{2+} response - (**Figure 35**). This initial linear or sublinear increase progressively jumped at the second threshold and shows supralinear characteistic as a function of an increasing number of active inputs (**Figures 33A-B and 35; Equation 3 and 4**). In the case (**Figure 33**) of high second-threshold input numbers (above ~ 15 active input numbers), the initial sublinear increase in the EPSP summation was revealed, as shown in this example. The first phase of the input-output curve, below the second-threshold input number onto the FS-PV INs can be well characterized with a sublinear increase. A similar sublinear integration rule of EPSPs, but without the step-like increase, has also been demonstrated in other aspiny interneurons in silent acute slices (Abrahamsson et al., 2012, Vervaeke et al., 2012). However, at 40 inputs on the FS-PV INs, the responses reached the second

threshold (2nd thr.) and a sigmoid-like increase in EPSP amplitudes was superimposed on the sublinear input-output curve. The sublinear input-output curve below the second threshold was fitted with an exponential equation (Equation 2, r=0.99) (**Figure 33A**). After subtracting the result of exponential fit revealed the sigmoid-like increase, which was fitted with the Boltzmann equation (**Equation 3; Figure 33B** red). Responses above the threshold were significantly larger. The sigmoid-like increase of the EPSP aplitude was combined with a simultaneously-occuring Ca^{2+} increase in the places of the inputs and the lateral dendritic regions (**Figure 33C-E**). In this case, areas were calculated as the temporal integral of the spatially averaged Ca^{2+} responses in a lateral dendritic region. Note the sharp, nonlinear increase at the same second threshold input number as in **Figure 33A (Figure 33C-E).** Somatically recorded interneuronal ripple oscillations could be detected above the second threshold in 48.57% of the measured cells (in 17 out of 35). The frequency of spontaneous SPW-EPSPs associated interneuronal ripple activities was 239.97±18.35 Hz. The uncaging evoked interneuronal ripple oscillations were robust in 11 cells while the frequency was 219.3±14.5 Hz similar to that found for the spontaneous one (**Figure 35**).

DOI:10.14753/SE.2015.2055

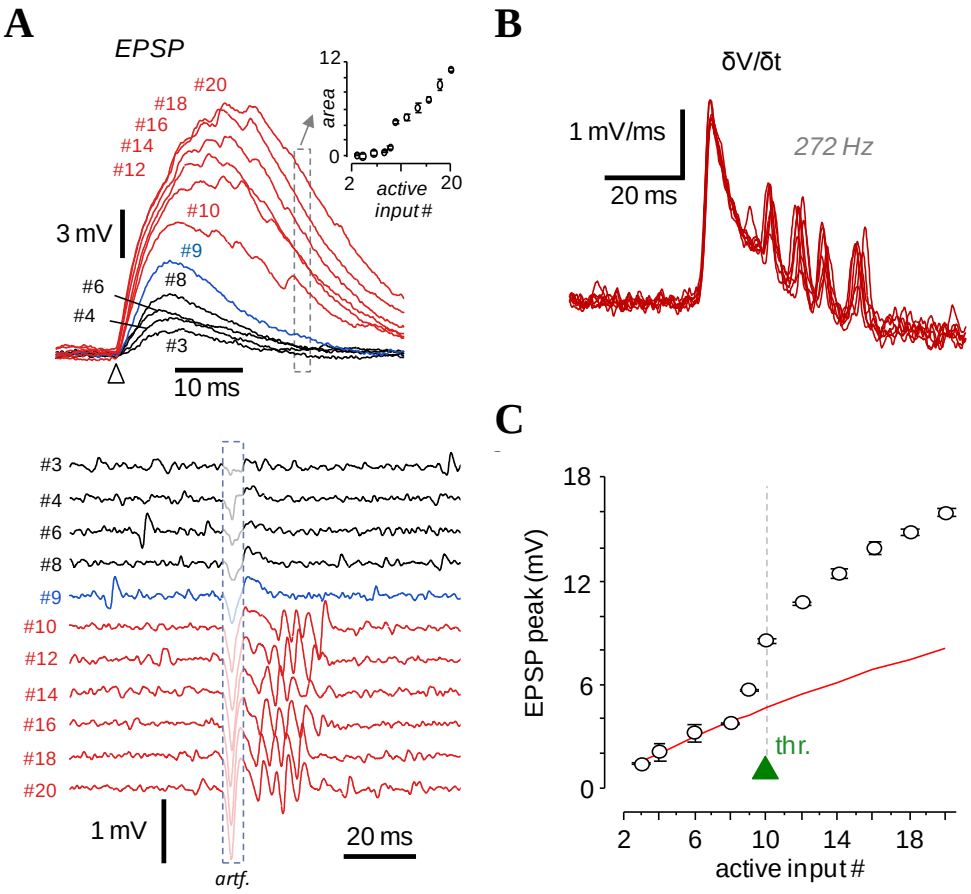

Figure 35. Synchronous activation of clustered glutamatergic inputs reproduces SPW-R-associated interneuronal ripple activities. A: Corresponding individual EPSPs with (bottom) and without (top) baseline subtraction demonstrate that ripple oscillations occur. Inset shows EPSP integrals calculated from data in the boxed region. *artf.*; signal of the uncage time evoked artefact. **B:** First derivative of representative EPSPs induced by 32 active inputs shows the stability of the oscillations. **C:** Amplitude of the simultaneously recorded EPSP peak versus the number of active inputs (mean ± s.e.m.). Dashed line and triangle indicate threshold input number (thr.). Initial part of the input-output curve was fitted by using Equation 3 (red).

Dendritic Ca^{2+} responses were 41.8±9.6 % larger when interneuronal ripple activities could appear on the top of the evoked EPSPs (p=0.008; n=6 cells) (**Figure 37**). The onset latency of the evoked interneuronal ripple oscillations became shorter when the active input numbers were pogressivlely increased. The interneuronal ripple activities varied less in amplitude and phase, but the frequency did not change (p>0.38, *t*-test) (**Figures 35B and 38**).

DOI:10.14753/SE.2015.2055

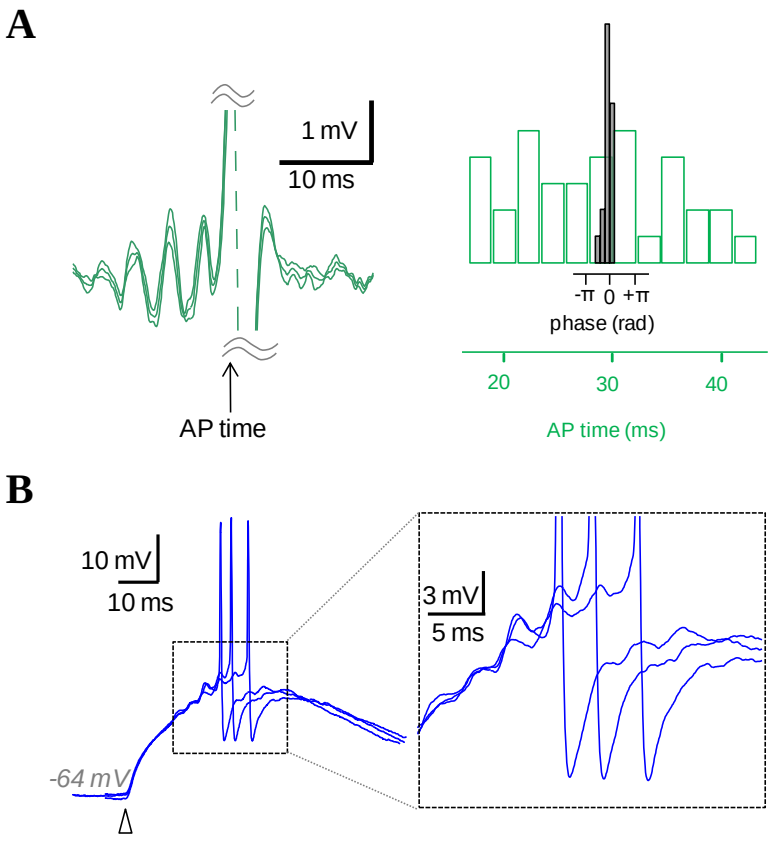

Figure 36. APs are phase locked to the peaks of the ripple oscillation. A: Left, suprathreshold voltage responses (mean ± s.e.m.) induced by 59 active inputs, baseline-subtracted and aligned to the peak of the AP. Right: Histogram of AP timing relative to the phase of interneuronal ripple oscillation (gray, n=18), and relative to the EPSP onset time (green, n=36). The two x-axes were overlaid according to the average oscillation time. **B:** Suprathreshold somatic voltage responses induced by DNI-Glu•TFA uncaging (2.5 mM) using a distributed pattern. Although there is an almost complete overlap between the three exemplified EPSPs immediately after uncaging (triangle), the appearance of interneuronal ripple oscillations can shift AP output by 1 or 2 cycles relative to the uncaging time. This means that the initially tight coupling between the time-course of EPSPs and uncaging time, which would alone indicate a precise AP output relative to the uncaging time, is destroyed by the interneuronal ripple oscillations, and AP output is disrupted by the interneuronal ripple oscillations.

Then we compared the effects on the interneuronal ripple activities on the activation of the spatiotemporally clustered and distributed inputs (**Figure 38**). The frequency of the evoked interneuronal ripple oscillations were similar (p=0.23, *t*-test,

DOI:10.14753/SE.2015.2055

n=7), but distributed input patterns induced ripple range oscillations in more dendritic segments (73.68%, 14/19 segments in 14/19 cells) and produced more oscillation cycles upon each induction. To investigate the functional relevance of interneuronal ripple oscillations we found that the distribution of somatic APs relative to EPSP onset time was rather broad in the presence of interneuronal ripple activities. APs were strongly coupled to the peaks of the ripple oscillations (**Figure 36**) which is in a good agreement with to that seen at the spontaneous SPW-Rs measurements (**Figure 29**).

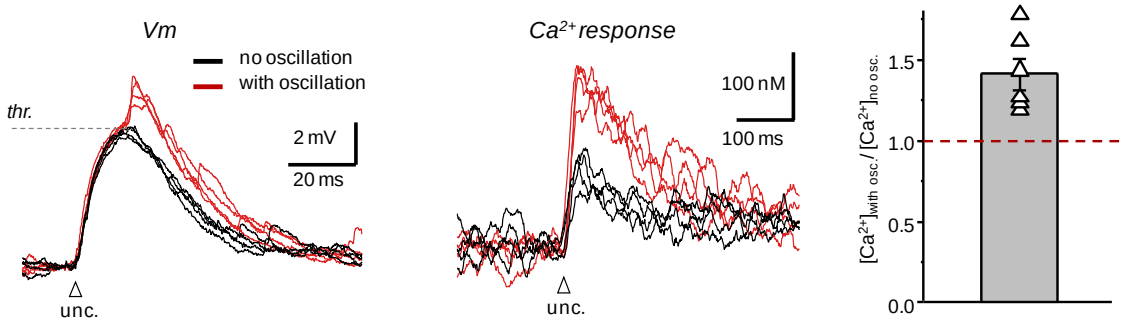

Figure 37. Dendritic Ca^{2+} responses were larger when interneuronal ripple activities could appear on the top of the evoked EPSPs. A: Left, uncaging-evoked somatic EPSPs induced by two-photon glutamate uncaging using a clustered input pattern similar to that shown in Figure 32. The number of activated inputs was set close to the interneuronal oscillation threshold in order to have EPSPs both with and without oscillations during the measurement. EPSPs which had similar amplitudes before approaching the oscillation threshold were separated into two groups depending on the power of the interneuronal oscillations (EPSPs with and without oscillations are shown in red and black, respectively). Middle: Although EPSP amplitude was not significantly different in the two groups before the appearance of the oscillations (p> 0.3), the group of EPSPs with larger interneuronal oscillations was associated with significantly larger Ca^{2+} responses in the lateral dendritic region (red). Right: Normalized increase in $[Ca^{2+}]$ following the appearance of interneuronal ripple oscillations in the lateral dendritic region (mean ± s.e.m., n=6 cells, p=0.008, *t*-test).

DOI:10.14753/SE.2015.2055

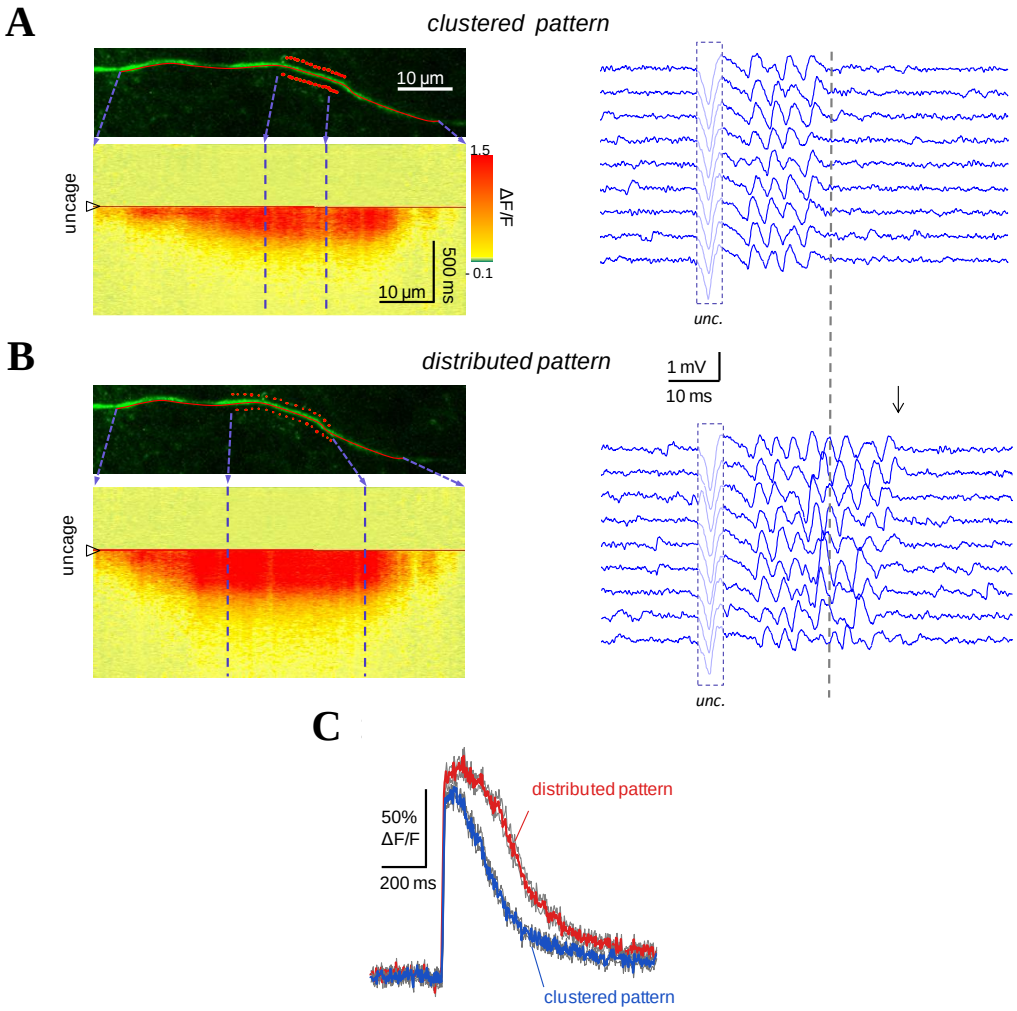

Figure 38. Distributed input patterns induce dendritic Ca^{2+} spikes with larger amplitude and more elongated interneuronal ripple oscillations than clustered patterns but the frequency of interneuronal ripple oscillations is maintained. A-C: The amplitude of the Ca^{2+} spikes further increased, and interneuronal ripple oscillations were more elongated, when oscillations were induced by more distributed input patterns, but the frequency kept constant. **A:** Left, maximum intensity z-projection image of the imaged dendritic segment shown in Figure 32A, with the location of 32 active inputs (red dots). Red line shows the scanning trajectory. (Bottom left) Average Ca^{2+} response (n=9 traces) induced by the 32 active inputs and measured along the red line. Arrows show corresponding locations. Right: Simultaneously recorded individual somatic voltage traces after baseline subtraction show interneuronal ripple oscillations. All traces were induced by the clustered input pattern of 32 active inputs activated by DNI-Glu•TFA uncaging. Traces are shifted relative to each other by 0.8 mV for clarity. Note the stability of interneuronal ripple oscillations at successive repeats. **B:** The same measurement

as in A but a distributed pattern of the same input number (32 active inputs) was used. Dashed line indicates time when oscillations stopped when using a clustered input pattern. Note, that the distributed pattern (bottom) of the same number of inputs induced more elongated interneuronal ripple oscillations with a larger dendritic Ca^{2+} signal than the clustered pattern. Although interneuronal ripple oscillations were longer, in this case their frequency did not change. **C:** Average Ca^{2+} transients calculated in the middle of the input regions in A and B. Traces are mean±s.e.m. Transients in Figure 32 are not saturated, as the distributed input pattern was able to induce dendritic spikes with higher peak Ca^{2+} amplitudes.

These data imply that the well-known fast, reliable EPSP-AP coupling of FS-PV INs is replaced during periods of strong excitation by a new integration mode where the timing of AP output is determined primarily by the phase of interneuronal ripple oscillations.

4.8. Ca^{2+} spikes are mediated by L-type voltage gated Ca^{2+} channels

To address the fifth criterion, we investigated the functional role of different ion channels in the mechanisms underlying dendritic spikes and inteneuronal ripple activites. The sigmoid-like increase in the temporal width of the uncaging-evoked EPSPs as a function of the number of active inputs (**Figures 35A**) suggested that an NMDA receptor-mediated mechanism contributed to the dendritic spike. Moreover, the propagating nature of Ca^{2+} responses (**Figures 31B and 34**), and the extended Ca^{2+} plateaus (**Figure 18A**), indicated that voltage-gated Ca^{2+} channels (VGCCs) could have a role, while the fast kinetics of interneuronal ripple oscillations suggest that voltage-gated Na^{+} channels should also contribute. Therefore the role of VGCC, NMDA and AMPA receptors in the generation of Ca^{2+} spikes were investigated.

Our earlier study supported the idea that the L-type VGCC blocker Nimodipine had the greatest effect on the Ca^{2+} responses in FS-PV INs' dendrites, thus evoked Ca^{2+} signal in the dendritic region is mostly determined by VGCCs. In this case, somatic depolarizing current steps (100 ms, 0-1,700pA) were injected into the somata of FS-PV INs in the presence of TTX (1µM), which induced large, well-propagating Ca^{2+} transients (**Figure 39**). Mibefradil did not decrease the step depolarization-induced dendritic Ca^{2+} accumulation in proximal dendritic area of FS-PV INs dendrites (104.40±1.63%, n=4, p=0.07). In contrast, L-type, voltage sensitive calcium channel

DOI:10.14753/SE.2015.2055

blocker Nimodipine induced significant reduction in Ca^{2+} transients under the same conditions (41.66±7.75%, n=4, p=0.0024) (**Figure 39C-D**). But what happens in distal dendritic area since upon somatic current injection APs do not back-propagate?

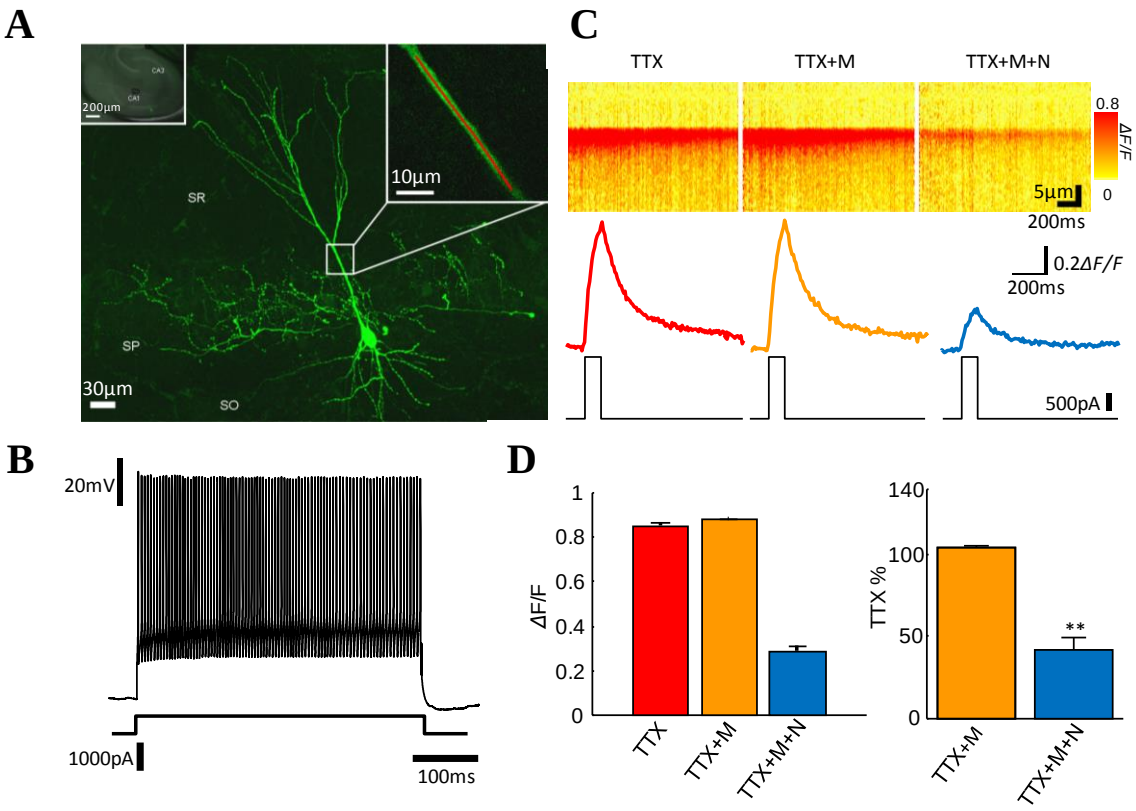

Figure 39. L-type VGCC mediate proximal dendritic Ca^{2+} signals in FS-PV INs. A: Confocal image stack of a representative FS-PV IN developed with DTAF-conjugated avidine after the physiological recording. In this case axonal process of the recorded neuron in the stratum pyramidale (SP) show the typical axonal arborization of the basket cells. Left inset shows the location of the recorded FS-PV basket cell in the hippocampal CA1 region. **B:** Somatic current injection (bottom) (AP frequency 200 Hz, adaptation 6.45%). **C:** Two-photon measurement of dendritic Ca^{2+} transients evoked by somatically injected current step (1,700 pA) in the presence of TTX and VGCC blockers (TTX, red trace) T-type VGCCs were blocked by 10 µM Mibefradil (TTX+M, orange trace), while L-Type VGCCs were blocked by 20µM Nimodipine (TTX+M+N, blue trace). Averge of three traces. **D:** Left, changes in the average peak amplitude of Ca^{2+} responses of the interneuron in A TTX (red bar), TTX+M (orange bar) and TTX+M+N (blue bar). Right: Pooled Ca^{2+} responses in the percentage of evoked Ca^{2+} responses in the presence of TTX (n=4 cells; $p<0.01$).

DOI:10.14753/SE.2015.2055

Spatiotemporally clustered input patterns were activated in the distal, apical dendritic segments of the FS-PV INs dendrites above the second threshold (43.8±2.9 active inputs) but carefully avoid evoking AP generation which might cause a putative side effect. Fluo4 and Alexa594 filled long dendritic segment were selected. In order to better separate of the input region and the lateral dendritic region, glutamate uncaging locations were selected in one end of the dendritic segment (**Figures 40 and 41**).

For the precise quantification of the pharmacological effects, I had to take into account the saturation and nonlinear response of the Ca^{2+} dye, and I therefore transformed the relative fluorescence data into [Ca^{2+}] using **Equation 5**.

Dendritic Ca^{2+} signals are dominantly triggered by AMPA and NMDA receptors, thus as we expected the combined application of AMPA and NMDA receptor blockers (CNQX and AP5, respectively) reduced the Ca^{2+} signals almost to zero (**Figure 42**) in both, hot-spot and lateral regions. In the lateral dendritic region the cocktail of VGCC blocker evoked great reduction in Ca^{2+} signal (**Figures 40 and 42**). Hippocampal interneurons express P/Q-, R-,L-,N- and T-type of VGCC (Vinet and Sik, 2006), but we found that the most important VGCC is the L-type one, because when we applied its specific blocker the Ca^{2+} signal reduced the most which is in agreement of our previous result (**Figure 39**). These data indicate that the lateral dendritic Ca^{2+} spikes are mainly determined by the VGCCs. In the central, hot-spot region the dependencity of the VGCC on the Ca^{2+} signal is more complex, because it is mediated in paralell by NMDA, calcium permeable AMPA receptors and VGCC, moreover further amplified by Na^{+} channel (**Figures 40, 41 and 42**). In line with other observations, I noted that Ca^{2+}-permeable AMPA receptors had a larger effect on the postsynaptic Ca^{2+} influx than NMDA receptors (Goldberg et al., 2003a, Goldberg et al., 2003c, Goldberg and Yuste, 2005, Lamsa et al., 2007, Topolnik, 2012). All the experiments were calculated in $\Delta F/F$ and $\Delta G/R$ as well (**Figure 43**).

DOI:10.14753/SE.2015.2055

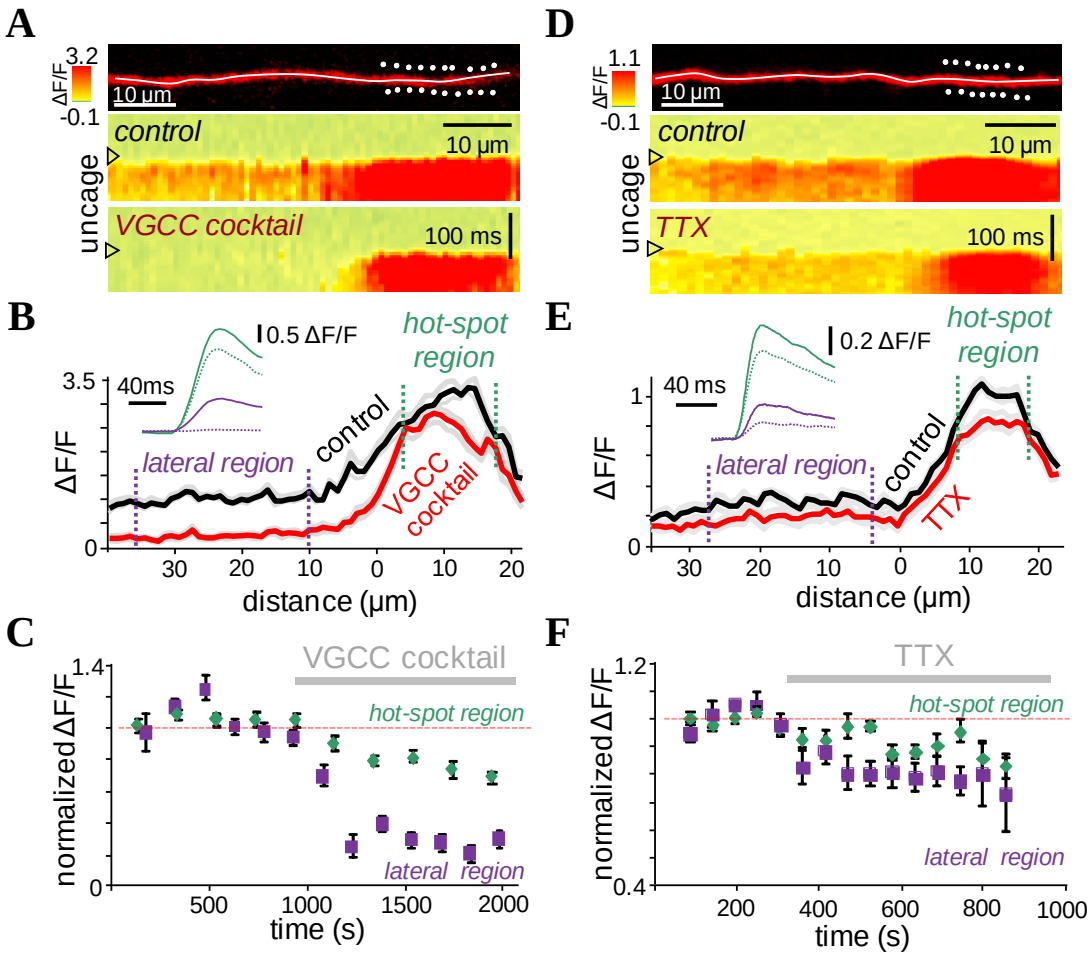

Figure 40. Dendritic Ca^{2+} spikes are mediated predominantly by L-type Ca^{2+} channels. A-C: Effect of VGCC blockers on uncaging-evoked Ca^{2+} responses. **A:** Maximum intensity z-projection image of a distal dendritic segment of an FS-PV IN. Average uncaging-evoked Ca^{2+} responses in control conditions (middle), and in the presence of a cocktail of VGCC blockers (bottom). White points are active input locations used for DNI-Glu•TFA uncaging (top). **B:** Spatial distribution of the peak dendritic Ca^{2+} response (mean ± s.e.m.) measured along the white line in A under control conditions (black) and in the presence of VGCC blockers (red). Inset: mean Ca^{2+} transients derived from the hot-spot (green) and lateral dendritic (magenta) regions before (solid line) and after (dashed line) application of the VGCC cocktail. **C:** Time-course of the effect of the VGCC cocktail on Ca^{2+} responses in the hot-spot (green) and lateral dendritic (magenta) regions. **D-F:** The same as A-C, respectively, but for TTX.

DOI:10.14753/SE.2015.2055

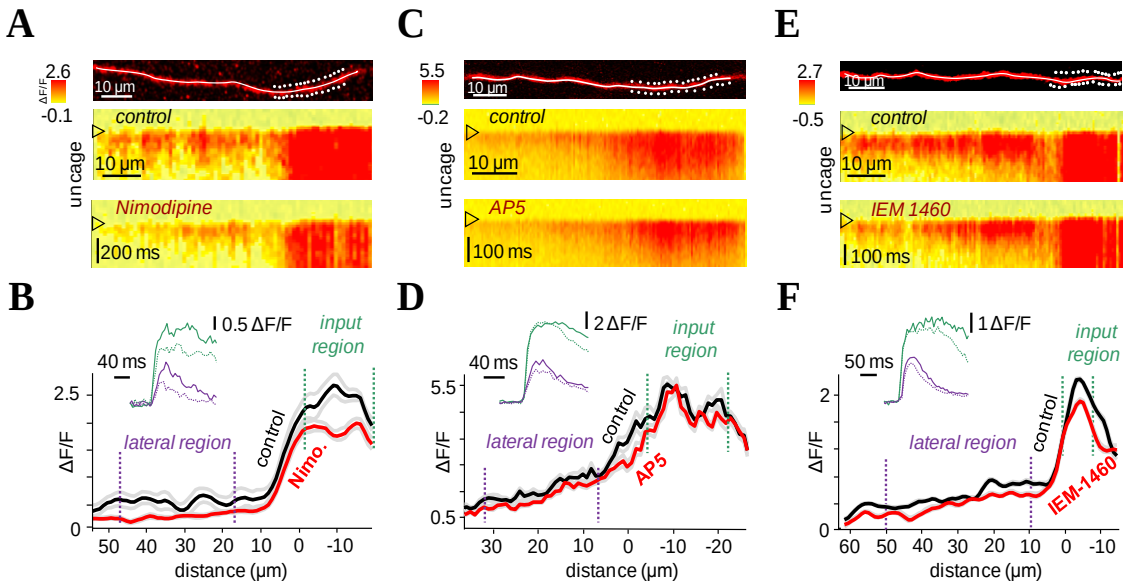

Figure 41. Role of L-type VGCC, NMDA, and Ca^{2+}-permeable AMPA receptors in dendritic spikes. A, Top: Maximum intensity z-projection image of a dendritic segment of an FS-PV IN filled with Fluo-4 and Alexa 594. White points are input locations used for patterned two-photon glutamate uncaging in the presence of 2.5 mM DNI-Glu•TFA. White line indicates the scanning path. Average uncaging-evoked Ca^{2+} responses following activation of all input locations shown in control conditions (middle) and in the presence of nimodipine (bottom). **B:** Spatial distribution of the peak dendritic Ca^{2+} response measured along the white line in A under control conditions (black) and in the presence of nimodipine (red). Gray traces are mean±s.e.m. (n=14) Inset: mean Ca^{2+} transients derived at the input (green) and lateral dendritic (magenta) regions from the Ca^{2+} responses before (solid line) and after (dashed line) nimodipine perfusion. **C-D:** The same as A-B, but for the NMDA-receptor blocker AP5. **E-F:** The same as A-B, but for the Ca^{2+}-permeable AMPA channel blocker IEM-1460.

DOI:10.14753/SE.2015.2055

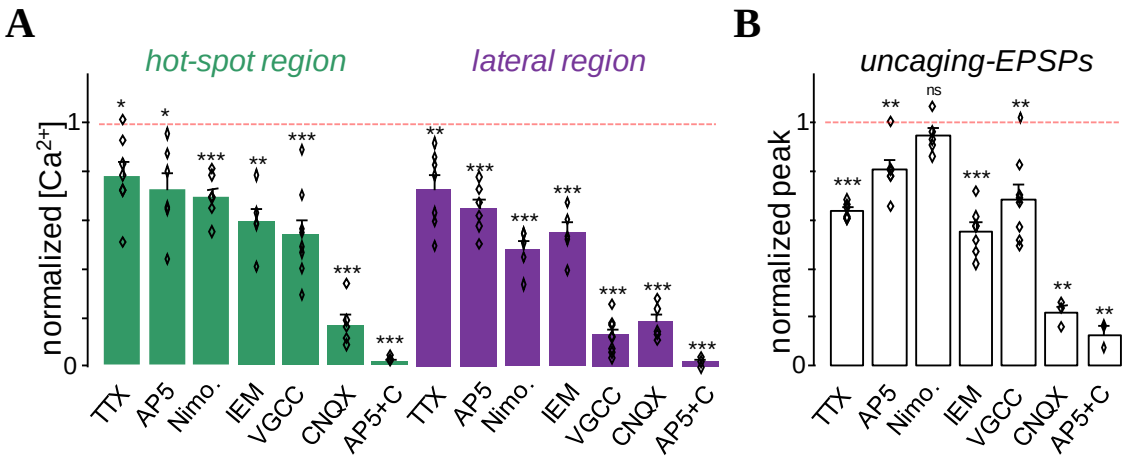

Figure 42. Summary of the phamacological experiments. A: Effect of different ion channel blockers on the peak amplitude of [Ca^{2+}]. Nimo. and AP5+C indicate nimodipine and AP5+CNQX, respectively. **B:** The same as A, but for simultaneously recorded EPSPs. All values are normalized to mean control values.

DOI:10.14753/SE.2015.2055

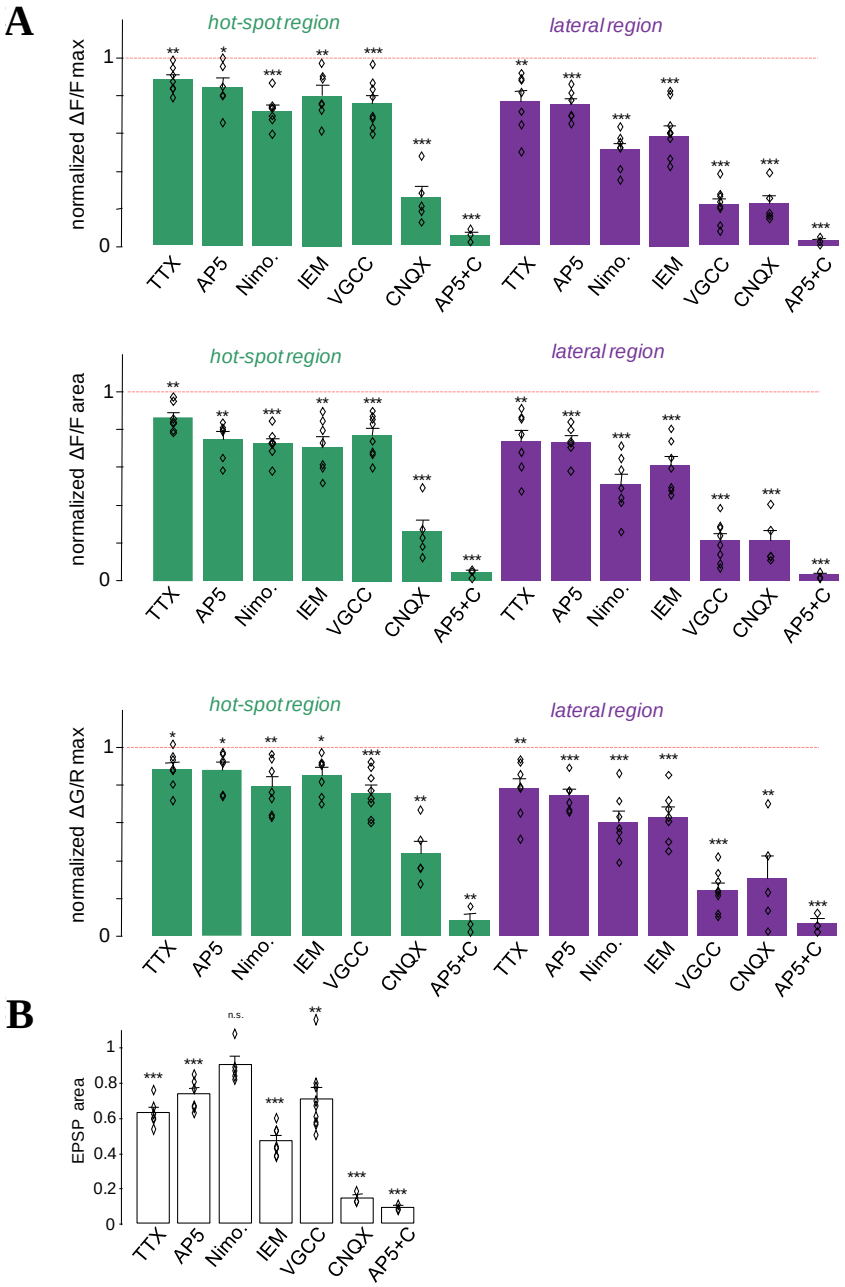

Figure 43. Summary of the role of VGCC, voltage-gated Na^+ channel, NMDA and Ca^{2+}-permeable AMPA receptors in the generation and propagation of the dendritic Ca^{2+} spikes. A: Amplitude of uncaging-evoked dendritic Ca^{2+} responses in the presence of TTX, AP5, nimodipine, IEM-1460, a cocktail of VGCC blockers and AP5+CNQX were spatially and temporally integrated and compared to their control values in individual cells (rhomboids). Bars show mean ± s.e.m. values. Spatially averaged Ca^{2+} response amplitudes were calculated either using the temporal integral (area) or the peak (max) of ΔF/F or ΔG/R values as indicated. **B:** Corresponding EPSPs. The same as in Figure 42B, but calculated for EPSP areas. All values are normalized to mean control values.

DOI:10.14753/SE.2015.2055

4.9. Interneuronal ripple oscillations are mediated by dendritic Na^+ channels

All the ion-channel blockers which were tested significantly decreased the amplitude and area of the uncaging evoked EPSPs (**Figures 42B and 43B**). This change could reflect the changes in local dendritic voltages as well, thus it can affect the generation of the interneuronal ripple oscillations which is riding on top of the EPSPs. I compensated the EPSP amplitude drop by increasing the uncaging laser intensity when oscillations disappeard until the amplitude of the uncaging-evoked EPSPs reached the control value again, or interneuronal ripple oscillations reappeared. The oscillations recovered or remained stable for all drugs except during TTX application (**Figures 44 and 45**). The Na^+ channel blocker totally abolished the interneuronal ripple oscillations, indicating the crucial role of these channels to create this phenomenon (**Figure 44A-B**). Application of AP5, nimodipine, IEM-1460 or the cocktail of VGCC blockers did not change significantly the frequency of the oscillations.

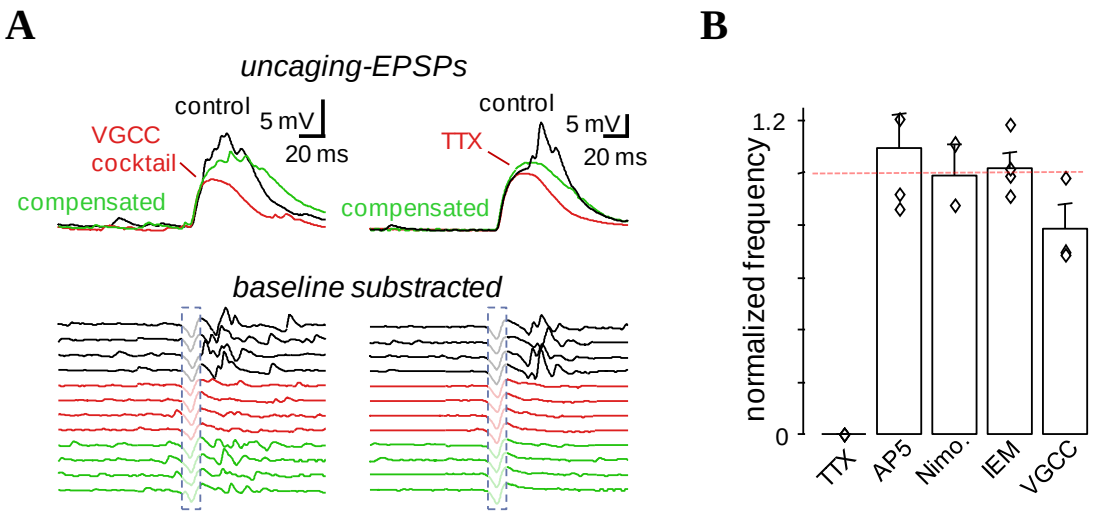

Figure 44. Pharmacological experiments on evoked interneuronal ripple activities. A: Subthreshold EPSPs showing interneuronal ripple oscillations with (bottom) and without (top) baseline subtraction in control conditions (black), but not in the presence of TTX or the VGCC cocktail (red traces left and right respectively). When the uncaging laser intensity was increased (compensated), interneuronal ripple oscillations were restored in the presence of VGCC blockers, but not when TTX was present. **B:** The effect of ion-channel blockers on interneuronal ripple oscillations. Ripple oscillations were only abolished by TTX.

DOI:10.14753/SE.2015.2055

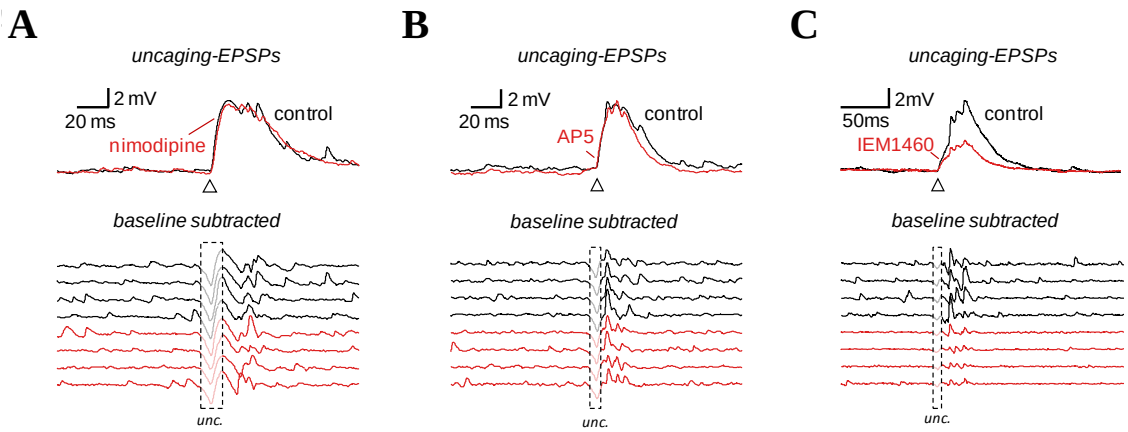

Figure 45. Role of L-type VGCC, NMDA, and Ca^{2+}-permeable AMPA receptors in interneuronal ripple oscillations. A: Simultaneously recorded representative EPSPs showing ripple oscillations before (top) and after (bottom) the use of the baseline-subtraction method under control conditions (black) and in the presence nimodipine (red). **B-C:** The same as A, but for the NMDA-receptor blocker AP5. **C:** The same as A, but for the Ca^{2+}-permeable AMPA channel blocker IEM-1460.

In order to validate more the dendritic origin of interneuronal ripple oscillations, TTX (10 µM) was injected onto the axosomatic region of the FS-PV INs, while clustered glutamate uncaging was evoked on the distal dendritic area as previously described (**Figure 46A**). The tip of the pipette and the laminar flow of the chamber were oriented in a way to increase red fluorescence in the axosomatic, but not in the distal dendritic region of inputs during the simultaneous injection of TTX and Alexa 594. As it was expected the somatically evoked APs were eliminated (**Figure 46B**), but the interneuronal ripple oscillations were not abolished which were evoked by glutamate uncaging (**Figure 46C-D**). Somatic current steps were used throughout the experiments to monitor the blocking efficiency of TTX. The frequency of the interneuronal ripple activities which was evoked by spatiotemporally clustered glutamate uncaging did not change significantly (control 212.83±24.18 Hz; TTX puff 182.72±18.72 Hz, paired t-test, p=0.156) (**Figure 46E**), indicating that the oscillations had indeed dendritic origin.

DOI:10.14753/SE.2015.2055

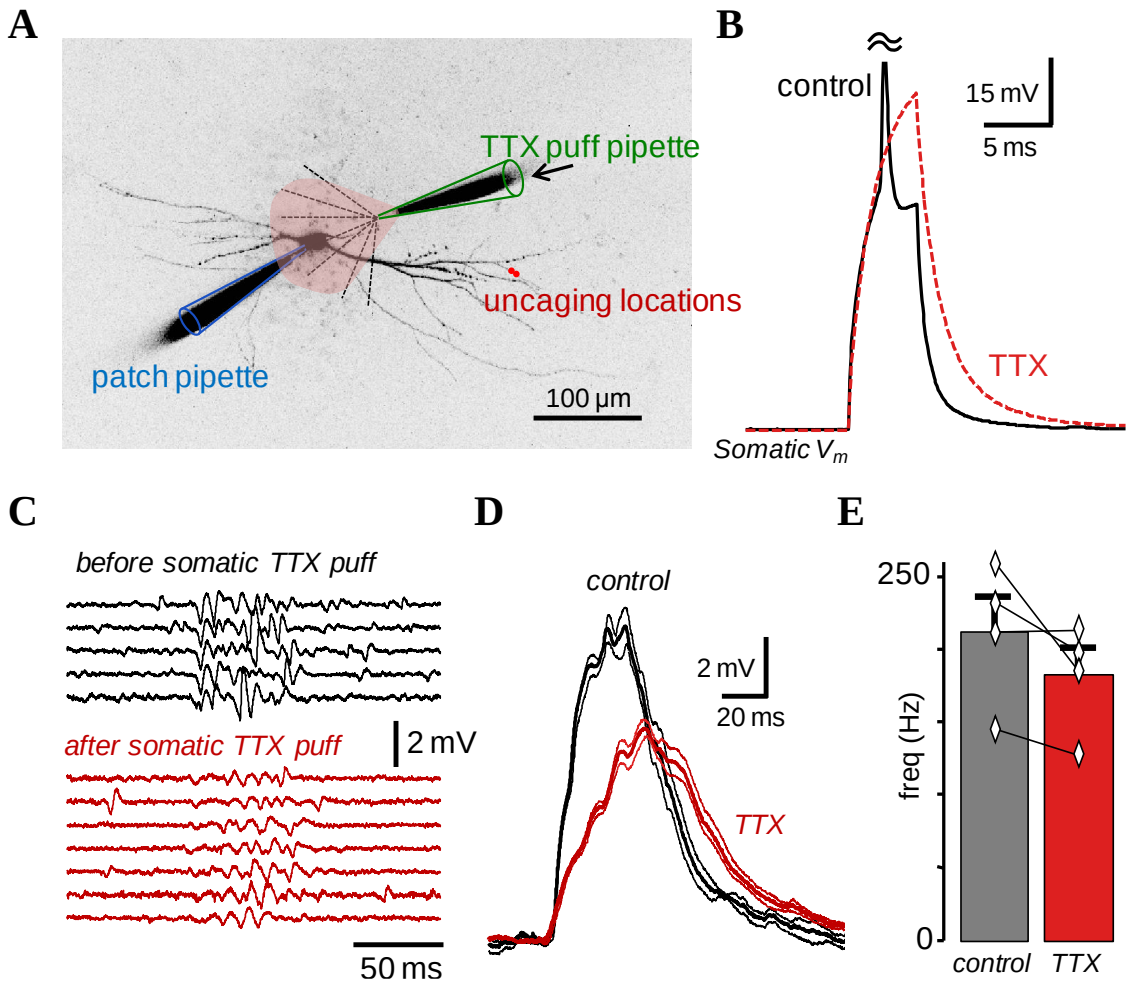

Figure 46. Local TTX injection to the axosomatic domain blocks somatic APs, but interneuronal ripple oscillations were maintained. A: Maximum intensity z-projection image of an FS-PV IN with the somatic recording and local TTX injection pipettes. Red points indicate the locations of glutamate uncaging. **B:** Fast injection of 10 µM TTX to the somatic region eliminated APs induced by brief somatic current steps. **C:** Somatic EPSPs after baseline sbtraction with interneuronal ripple activity in control (black, n=5 traces) and after TTX (red, n=7 traces) injection. **D:** Average somatic EPSPs (mean ± s.e.m.) from the same cell in C in control and after TTX injection. **E:** Oscillation frequencies in the control case and after local TTX injection represent in bar graph.

To detect dendritic local membrane potential oscillations more directly, whole cell patch clamp and dendritic juxtacellular recordings were combined (**Figure 47**). Transmitted gradient contrast images were simultaneously measured and overlapped and used to guide the calibrated recording patch pipette to a juxta-dendritic position

using an automatic software algorithm. Oscillations were evoked by spatiotemporally clustered input pattern using glutamate uncaging, and at the same position juxtacellular recording was performed (266.37±67.05 µm, mean±s.d.) (**Figure 47A**). Interneuronal ripple oscillations could be recorded simultaneously using both somatic whole cell and juxtacellular recordings (**Figure 47B**). The somatically evoked APs could not appear at the site of the juxtacellular recording which remained under the detection threshold (**Figure 47F**). To test whether the evoked interneuron ripple activity has an affect only in the well-localized area around the dendritic arbor or not, I recorded LFP with the pipette used juxtacellular recording by gradually moving away from the dendrite (**Figure 47C-E**). The same inputs in the same dendritic region were activated as shown in **Figure 47A** to induce interneuronal ripple oscillations. The stability of the oscillations were monitored by somatic whole-cell recording during the experiments. The juxtacellular recording interneuron ripple oscillation amplitude was totally diminished in 40 µm (spatial decay constant 15.6±4.9 µm, n=4) (**Figure 47E**) from the uncaging evoked dendritic area, which means that the activation site have remained localized.

In the next set of experiments the membrane potential thresholds of interneuronal ripple oscillations on an exemplified uncaging-evoked EPSPs were measured at the soma. Interneuron ripple oscillations were generated by two-photon DNI-glutamate uncaging, using spatiotemporally clustered input patterns as above. The relative threshold was defined as the difference between the oscillation threshold and the somatic membrane potential (**Figure 48A**). During the comparison of the somatic membrane potential threshold of interneuronal ripple oscillations and APs we found that the membrane potential dependence of APs was less steep (**Figure 48B**). These data demonstrated the membrane potential dependence of interneuronal ripple oscillation threshold with this method (**Figure 48C-F**). The somatic membrane potential values were subtracted from the threshold of interneuronal ripple oscillations (relative threshold) then measurement points were averaged in equally distributed membrane potential intervals. Finally, mean ± s.e.m. data were plotted against somatic membrane potential. Note that the relative threshold of interneuronal ripple oscillations varies only slightly with somatic membrane potential, suggesting that the region where the oscillation is generated is not clamped (**Figure 48G**). Thus I can say that in contrast to

DOI:10.14753/SE.2015.2055

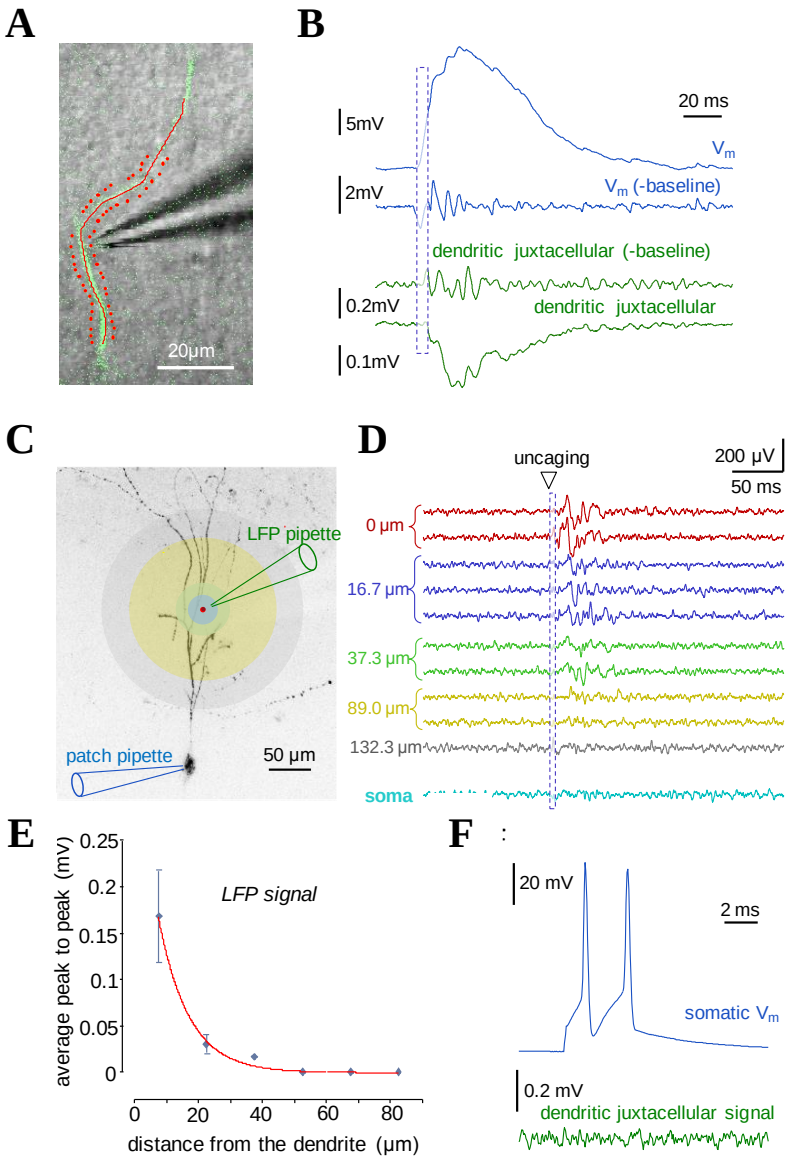

Figure 47. Two-photon targeted juxtacellular and LFP measurement of interneuronal ripple oscillations. A: Two-photon fluorescence image and overlapped transmitted gradient contrast image of a dendritic segment with the juxtacellular pipette with the representation of scanning trajectory (red line) and uncaging locations (red dots). **B:** The juxtacellular signal (green) from the dendritic location in A and the simultaneously recorded somatic membrane potentials (blue) are shown with and without baseline substraction. **C:** Experimental arrangement. Red dot indicates the uncaging location. **D:** Individual LFP signals as a function of distance from the activated interneuronal dendritic segment and the somatic region (cyan). **E:** Average amplitude (mean ± s.e.m., n=4) of the oscillations in the LFP signal as a function of distance. Red line is an exponential fit to the data. **F:** The somatic membrane potential (blue) and the dendritic juxtacellular signal (green).

DOI:10.14753/SE.2015.2055

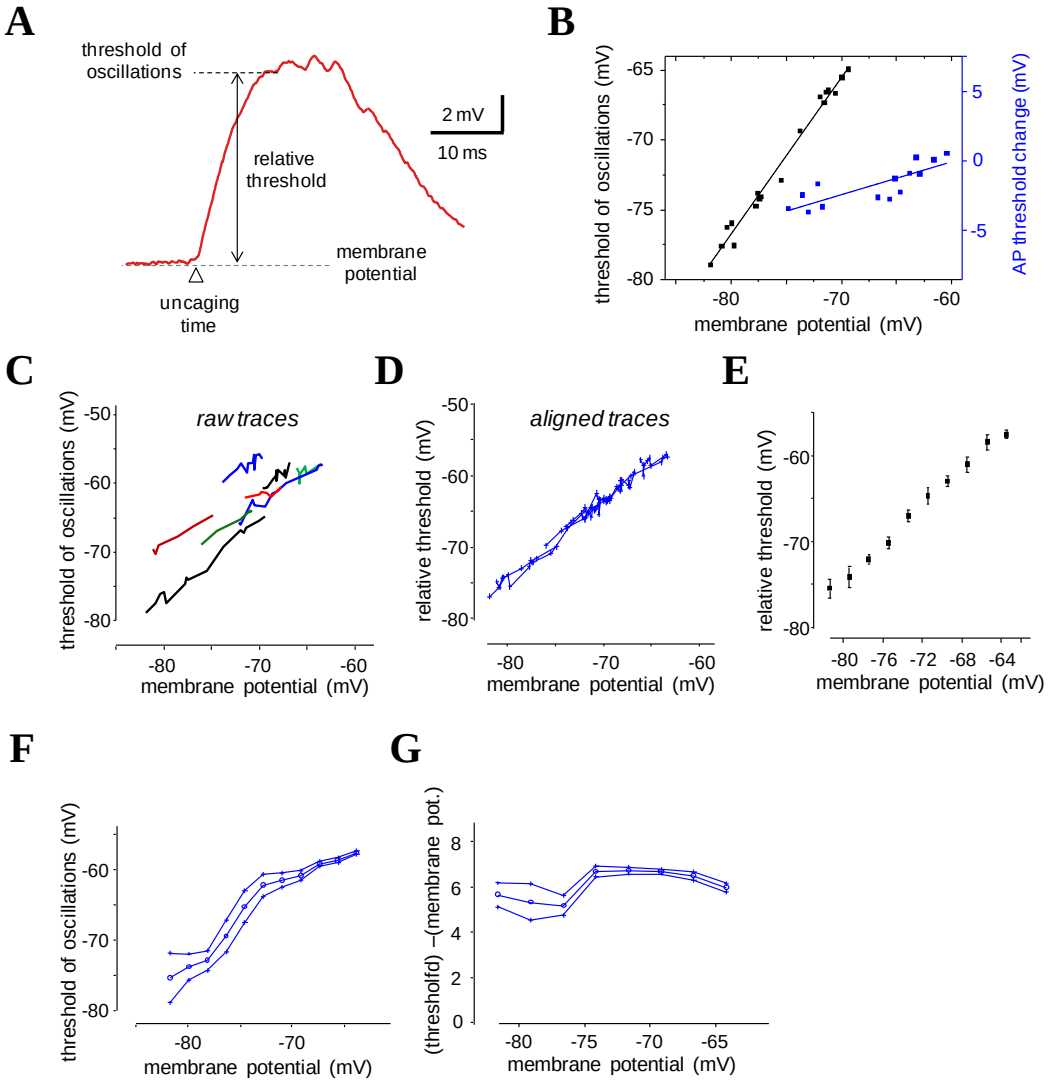

Figure 48. Dependence of the membrane potential threshold of interneuronal ripple oscillations on somatic membrane potential indicates the distal origin of the oscillations A: The main parameters of evoked EPSPs with interneuronal ripple oscillations. **B:** Somatic membrane potential threshold of interneuronal ripple oscillations (black) and APs (blue) shown in the same y-axis range (16 mV) and plotted against the somatic membrane potential in a representative FS-PV IN. **C:** Membrane potential threshold of interneuronal ripple oscillations as a function of somatic membrane potential (n=8 cells). **D:** As in C, but responses of individual interneurons were shifted relative to each other along the y-axis in order to increase the overlap between the traces. **E:** Traces in D were averaged (mean ± s.e.m.) **F:** Data in C were averaged (mean ± s.e.m.) in equally distributed membrane potential intervals. In contrast to D and E, measurement data were not shifted. **G:** The somatic membrane potential value was subtracted from the threshold of interneuronal ripple oscillations (relative threshold).

somatic AP, the threshold of interneuronal ripple oscillations changed in proportion to the somatic membrane potential (**Figure 48**), which reflects the weak control over the oscillations by the somatic membrane potential. These data, together with the local uncaging experiments and propagation measurements strongly support the dendritic origin of the interneuronal ripple oscillations.

These results show that the propagating dendritic Ca^{2+} spikes are predominantly mediated by L-type Ca^{2+} channels, while the related interneuronal ripple oscillations are determined by voltage-gated Na^{+} channels. In summary, I can conclude that dendritic spikes exist in FS-PV INs, as the observed events satisfied all five of the criteria defined initially.

DOI:10.14753/SE.2015.2055

5. Discussion

5.1. FS-PV INs show dynamic switch in dendritic integration properties during SPW-Rs

The presence of Ca^{2+}-permeable AMPA-, NMDA receptors, as well as voltage-gated Na^{+}, Ca^{2+}, and K^{+} channels in FS-PV IN dendrites has been demonstrated in earlier studies. It has been proposed that the fast electrical and Ca^{2+} signals provided by these channels are spatially and temporally attenuated and well-compartmentalized (Goldberg et al., 2003c, Goldberg and Yuste, 2005, Hu et al., 2010). Such functional dampening and spatial segregation are thought to endow these interneurons with prompt and effective signal integration in the sublinear range. In contrast to the widely accepted view, this work supports the idea that FS-PV IN dendrites are more active and that their functionality can dynamically change during SPW-Rs. Experiments based on caged-glutamate compound and 3D imaging methods, challenge the classic hypothesis of functional role of interneurons.

Here I demonstrate a network-activity dependent dynamic switch in dendritic integration mode in hippocampal CA1 FS-PV INs.

The passive, well-dampened FS-PV IN dendrite can be transiently activated by a high number of spatially and temporally clustered excitatory inputs during SPW-Rs. In this active state, several physiological properties of FS-PV INs change (**Table2**).

Our main findings of active FS-PV INs during SPW-R activities are the following:

I. AP-associated Ca^{2+} responses are not compartmentalized to the proximal dendritic regions but also invade distal dendritic segments.
II. Dendritic spikes occur, in contrast to the low-activity baseline state (Hu et al., 2010).
III. Supralinear dendritic integration with a dual-integration threshold replaces linear or sublinear summation.
IV. Compartmentalized synaptic Ca^{2+} signals are replaced by broadly propagating Ca^{2+} waves which are generated at dendritic hot-spots.

DOI:10.14753/SE.2015.2055

V. Dendritic voltage-gated Na^+ channels, which are functionally inactive in low activity conditions (Hu et al., 2010), start to generate interneuronal ripple oscillations, which are associated with dendritic Ca^{2+} spikes.

VI. The integration mode of FS-PV INs changes, AP outputs are tightly coupled to the phase of interneuronal ripple oscillations, and the total time-window of AP outputs becomes broader compared to the submillisecond precision in EPSP-AP coupling that characterizes the low activity state.

Table 2. SPW-R activity generates a dynamic switch from a ground state of passive integration to an active state. The properties of the two states are compared and summarized in the table.

	'ground' state	'excited' state during SPW-Rs
dendritic activity	passive dendrites inactivated by a high K^+ / Na^+ ratio	active
dendritic Ca^{2+} spikes	no	yes
Ca^{2+} signaling	compartmentalized, (~1 µm long dendritic microdomains)	large Ca^{2+} spikes
AP back-propagation	passive, < 100-150 µm from the soma	active, > 350 µm
dendritic integration: EPSPs	sublinear or linear	supralinear
dendritic integration: dendritic Ca^{2+}	sublinear or linear	supralinear
EPSP-AP coupling	fast, submillisecond timescale	slow, AP output is synchronized to the peaks of the interneuronal ripple oscillations
membrane ripple oscillations	no	yes
dendritic Na^+ channels are activated	no	yes, and generate interneuron ripple oscillation
dendritic hot-spots	no	yes, can be multiple

DOI:10.14753/SE.2015.2055

5.2. New techniques help to reveal and simulate SPW-R associated dendritic hot-spots and Ca^{2+} spikes in FS-PV INs

To study the physiological properties of FS-PV INs in their active state during SPW-Rs, we had to develop new recording, imaging and uncaging techniques. First, the activity patterns of distal apical dendrites of CA1 FS-PV INs are hard to be measured *in vivo*, because these structures are located deep from the surface of the brain. The recent imaging techniques could not solve this problem even with special surgery procedure and newly developed objectives. The *in vitro* experiments could offer great perspectives to study long and thin apical dendritic arbor of FS-PV INs, but in submerged conditions conventionally used thickness of the slices do not maintain spontaneous SPW-R activity. Thus I used a special type of submerged chamber which is a modified version of previously developed dual-superfusion chamber (Hajos et al., 2009). In this chamber-type the slices get higher oxygen level, which helps to keep the functionally working networks. Thus spontaneous neuronal activities such as SPW-Rs can be recorded. Besides this, I exchanged the materials of the chamber which enhanced the two-photon imaging as well.

Second, I used 3D scanning methods which provide high temporal resolution up to tens of microseconds – temporal super-resolution microscopy. With this new technique, imaging hot-spot activity in complex dendritic arbors with high spatio-temporal resolution is feasible. This new system operates at video-rate time resolution and is constrained to two-dimensional image acquisition in order to maintain an appropriate signal-to-noise ratio. Thus I can simultaneously measure the fastest regenerative events with high spatial discretization on the size scale of dendritic hot-spots during SPW-Rs (~4 μm) in multiple dendritic segments of a thin distal arbour of FS-PV INs.

Third, I used a new glutamate uncaging material DNI-Glu•TFA, in order to simulate what happened in the dendrites during spontaneous SPW-Rs. This was essential to determine the dendritic active input patterns and underlying ion channel mechanisms which are capable of the generation of hot-spots and the associated dendritic spikes during SPW-Rs. With this new compound up to 60 active inputs within a short time period (less than one cycle of the ripple oscillations) can be activated in complex spatiotemporal patterns. As phototoxicity increases rapidly and nonlinearly (Ji

et al., 2008) as a function of the required laser intensity, the increased uncaging efficiency of DNI-Glu•TFA provides a significant advantage in neurophysiological experiments compared to the widely used MNI-Glu.

These novel methods yielded several new insights into the fine spatiotemporal structure of dendritic hot-spot activities. Here I have shown that in double-perfused acute slices, the network activities are better preserved and provides spatially and temporally clustered synaptic input patterns to FS-PV INs that activate dendritic hot-spots. Moreover these signals can be simulated by glutamate uncaging to reveal the background ion channel contributions.

5.3. Mechanisms of SPW-R associated dendritic Ca^{2+} hot-spots and Ca^{2+} spikes

Previous studies indicate that hot-spot activity does not exist in cell culture FS-PV INs (Takahashi et al., 2012). Here I showed that dendritic hot-spots can be intense in FS-PV INs during SPW-R acitivities. I demonstrated that well-defined high active input number (the second threshold) in the distal apical dendrite of the FS-PV INs dendritic Ca^{2+} spikes can emerge from local hot-spot and can activate long dendritic segments in multiple branches. Clustered input patterns can activate hot-spots via the activation of calcium-permeable (~40%) and non permeable (~35%) AMPA-, and NMDA receptors (~ 25%). This activity triggers the initial Ca^{2+} signal in the hot-spot regions. Then, as a second step, voltage gated ion channels are open such as Ca^{2+} and Na^{+} channels, and evoke propagating dendritic spikes laterally to the hot-spot regions. These spikes emerge with a significant delay compared to the hot-spot signal and propagate centripetally and centrifugally along the dendrite. I found that these Ca^{2+} spikes are engaged to the VGCCs, dominantly to L-type VGCCs.

The activation of the voltage gated Ca^{2+} and Na^{+} channels in the second step contributes by 35% to the evoked EPSP amplitude and further increases the Ca^{2+} responses in the central hot-spot regions as well. The propagation speed of dendritic Ca^{2+} spikes is relatively low, much slower than the typical AP backpropagation speed, creating dendritic ‘delay lines’ for signal integration. This could provide a relatively broad temporal window for dendritic integration both between and within hot-spots, which may play a crucial role in coincidence detection and synaptic plasticity.

DOI:10.14753/SE.2015.2055

5.4. Interneuronal ripple oscillations revealed in FS-PV INs

There are two components of intrinsic membrane resonance, namely resonating and resonance-amplifying conductances. Resonating conductances are mediated by HCN-channels or M-type K^+ channels, while resonance amplifying conductances are dominantly dependent on persistent Na^+ channels or NMDA resceptors. These were observed in the relatively low-frequency theta band, with rapid decrease in amplitude at higher frequencies (Narayanan and Johnston, 2007, Johnston and Narayanan, 2008, Hu et al., 2009, Zemankovics et al., 2010). Earlier studies found that there are no resonances or resonance at beta-gamma frequencies in fast-spiking hippocampal interneurons (Carnevale, 2006, Zemankovics et al., 2010) only at 40 Hz (Pike et al., 2000). I found that Ca^{2+} spikes are associated with intrinsically generated membrane potential oscillations in a much higher, ripple frequency band in FS-PV INs during SPW-Rs. These results could be revealed by the baseline subtraction method which, in contrast to traditional frequency-based approaches (such as band-pass filtering), better preserved the amplitude and the phase of individual oscillation cycles. Clustered input patterns were able to induce interneuronal ripple oscillations in short dendritic segments. Na^+ channels had a relatively high impact on somatic EPSPs compared to the VGCCs, but contributed less to the generation of Ca^{2+} transients. Though the Na^+ channels contribute to the generation of the interneuronal ripple activity, the perisomatic Na^+ channels do not play a role in the generation of the interneuronal ripple oscillations rather the Na^+ channels located at distal dendritic regions. The dendritic origin of interneuronal ripple oscillations were further supported by the presence of oscillations in dendritic, but not in axosomatic, juxtacellular recordings, and by the weak dependence of the relative oscillation threshold on somatic membrane potential.

Therefore our experimental results suggest that dendritic voltage-gated Ca^{2+} and Na^+ channels may be primarily responsible for the supralinear responses and the accompanying fast interneuronal ripple oscillations. The feasibility of this scenario was further investigated by constructing a detailed compartmental model of a CA1 basket cell, based on a morphological reconstruction (Gulyas et al., 1999). The model suggested that the slow spike was mediated mainly by dendritic voltage-gated Ca^{2+} channels, while the fast spikes were generated by dendritic voltage-gated Na^+ and K^+ channels. The dendritic spikes were observable at the soma as a sudden increase in

EPSP amplitude and duration, and a fast (ripple-frequency) oscillation riding on top of the slower depolarizing component. Thus, the modeling results confirm that dendritic spikes evoked in FS-PV INs by strong excitatory synaptic input provide an explanation for our experimental observations (data are not shown in this thesis).

5.5. Interneuronal ripple activities determine outputs of FS-PV INs

I demonstrated the presence of high frequency, ripple oscillations recorded in the membrane voltage in FS-PV INs. These signals are mediated by Na^+ channels and may reflect the generation of high frequency trains of APs. Interneuronal ripple oscillations and synaptic inputs are related to spike output of FS-PV INs. Ongoing, clustered active inputs are integrated and hot-spots are generated. The membrane ripple oscillations start to form in few millisencond-long time windows for signal integration and then AP output is generated after some oscillation periods. The AP output is synchronized to these interneuronal ripple oscillations, i.e. EPSPs which are in phase synchrony with the oscillations will be amplified and contribute to trigger APs. Moreover, an ongoing input assembly (or its failure), may shift the AP phase in a positive or negative direction relative to the interneuronal ripple oscillations, forming the firing pattern of individual FS-PV INs in the SPW-R associated cell assembly.

Our working hypothesis indicates a bidirectional relationship between dendritic mechanisms and cell assembly firing. In this paradigm, cell assemblies activate dendritic segments, where hot-spots are generated. The hot-spots activate oscillations at ripple frequencies in the dendrite which determines the neuronal outputs of individual neurons within the cell assemblies. According to this assumption, memory information which is strongly captured in the hippocampus during SPW-Rs as a temporal pattern of cell assembly discharges (Buzsaki and Silva, 2012) should also be present as dendritic active input patterns with a certain phase relative to the interneuronal ripple oscillations.

5.6. The model of SPW-R generation

Here, I demonstrate a novel, dendritic hot-spot related mechanism to be integrated into the currently accepted network model of SPW-R activities (Buzsaki and Silva, 2012). Synchronized firing of CA3 cell assemblies are responsible for the

generation of SPW events recorded in the CA1 region (Buzsaki and Silva, 2012). These cell assemblies cause strong depolarising events in the dendrities of CA1 FS-PV INs which are followed by membrane potential oscillations in ripple frequency range. Ellender et al. showed in 2010 that smaller cell assemblies can also provide the required depolarization in CA3 subfield. According to this in CA1 and CA3 minisclices have also been demonstrated to be capable of generating SPW-Rs (Maier et al., 2003, Nimmrich et al., 2005, Maier et al., 2011). In 2005, Nimmrich et al presented that they can reproduce SPW events and could also generate the associated network ripple oscillations in CA1 minislices by local application of KCl to the dendritic layers, while GABAergic and glutamatergic synaptic transmissions were completely blocked. These data also suggest that a single depolarization event in the dendrites without any internal pattern is capable of activating intrinsic membrane mechanisms which then generate the ripple oscillations. In the recently accepted view fast GABAa receptor mediated inhibition is critical to the generation of ripple oscillations. The model proposes a SPW induced excitation of pyramidal cells, combined with the timing ability of interneuron interaction (Stark et al., 2014). Firings of PV interneurons become phase locked and coherent because of their reciprocal inhibition. This phase locked ripple frequency range activity reaches the pyramidal cell assemblies and promotes their phase-modulated firing (Schlingloff et al., 2014).

I demonstrated that activation of clustered glutamaterg inputs can generate a depolarizing hump and thus reproduce the hot-spot associated SPW-R event and also capable of generating secondary membrane osciallations in the ripple frequency range in distal apical dendrite of the CA1 FS-PV IN. In summary, I can say that the phase-locked firing during SPW-Rs is not a simple reflection of the discharge pattern of presynaptic cell assemblies, but oscillations can be formed actively and intrinsically by the dendritic membrane.

DOI:10.14753/SE.2015.2055

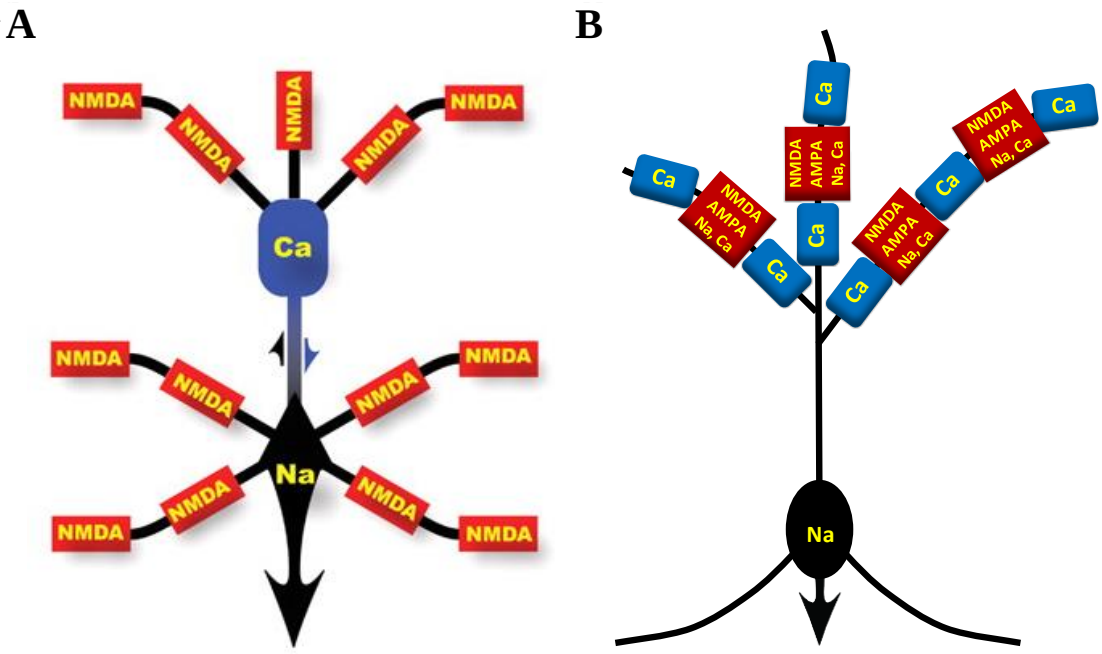

Figure 49. Comparison of the working hypothesis of pyramidal neurons and FS-PV INs. Schematic drawing represents the multiple local spike zones of the previously described L5 pyramidal neuron (A) (Larkum et al., 2009) and CA1 FS-PV IN (B) based on our data.

Ripples have been considered as a network phenomena, although smaller and smaller parts of the hippocampal formation have recently been demonstrated to be possible sources of ripple oscillations (Maier et al., 2003, Nimmrich et al., 2005, Ellender et al., 2010, Buzsaki and Silva, 2012, Schlingloff et al., 2014, Stark et al., 2014). I found that the smallest functional unit which can generate fast oscillation in the ripple frequency range by activation of approximately 30 coincident inputs is a short, approximately 20 μm segment of a dendrite, named hot-spot. Our working hypothesis suggests a model of the local NMDA Ca^{2+} and Na^{+} spike along FS-PV INs. In this model, compared to the previously described model for pyramidal neurons (Larkum et al., 2009), the initial spike zone was triggered by the activation of the NMDA receptor with the contribution of AMPA and Ca^{2+} permeable AMPA receptor. These spikes show a multi-site localization along the FS-PV thin apical dendrite (hot-spot). The Ca^{2+} spike zones are localized between these initial spike zones along the dendritic segments indicating multiple-site distribution (propagating Ca^{2+} spikes centifugally and centripetally). The Na^{+} spike zone as Larkum's model is localized to the perisomatic

DOI:10.14753/SE.2015.2055

domain of the cell (**Figure 49)**. Although the duration of the interneuronal ripple oscillations increased upon increasing active input number, and the onset latency decreased, the oscillation frequency remained stable, suggesting that these dendritic ripple generators are the integrated circuit elements which provide the stable ripple frequency of the network oscillation during SPWs. Interneuronal ripple oscillations could be detected in the local field potential at distances up to a few micrometers from the activated dendritic segments, but how and why these independent dendritic oscillators interact within the dendritic arbor of the same neuron, and throughout the gap-junction-connected dendritic network of interneurons, and how they finally give rise to the local field potential, still needs to be investigated.

DOI:10.14753/SE.2015.2055

Conclusion

Hippocampal FS-PV INs and their crucial role in the generation of SPW-Rs are intensively studied mainly in electrophysiological measurements. Moreover, with confocal and two-photon imaging techniques the mechanism of dendritic integration in FS-PV INs' dendrites is also an important and studied area of neuroscience. But the relationship between the two important topics couldn't have been examined. To achieve this, recently developed 3D and 2D two-photon imaging techniques and new glutamate uncaging material were used. In my thesis I challenge the classical view of FS-PV INs dendritic integration mode and function during the presence of spontaneous SPW-Rs.

First, AP-associated Ca^{2+} responses are not compartmentalized to the proximal dendritic regions but also invade distal dendritic segments during SPW-Rs. Dendritic spikes occur, in contrast to the low-activity baseline state (Hu et al., 2010).

Second, I found that supralinear dendritic integration with a dual-integration threshold replaces linear or sublinear summation. Compartmentalized synaptic Ca^{2+} signals are replaced by broadly propagating Ca^{2+} waves which are generated at dendritic hot-spots. Dendritic voltage-gated Na^{+} channels, which are functionally inactive in low activity conditions (Hu et al., 2010), start to generate interneuronal ripple oscillations, which are associated with the dendritic Ca^{2+} spikes.

Third, I found that the integration mode of FS-PV INs changes, AP outputs are tightly coupled to the phase of interneuronal ripple oscillations, and the total time-window of AP outputs becomes broader compared to the submillisecond precision in EPSP-AP coupling that characterizes the low activity state.

Fourth, my findings indicate that propagating Ca^{2+} spikes are mainly dependent on L-type VGCC, while interneuronal ripple activities are related to non-perisomatic Na^{+} channels.

I demonstrate a novel ingredient in the generation of population ripple oscillations. Synchronized inputs arrive to the CA1 FS-PV INs from CA3 and local CA1 cell assemblies which generate hot-spots and associated intrinsic ripple oscillations in distal apical dendrites of FS-PV INs. The membrane ripple oscillations start to form few millisencond-long time windows for signal integration, than AP output is generated after some oscillation period. Our working hypothesis supports the idea that the AP

DOI:10.14753/SE.2015.2055

output is synchronized to these interneuronal ripple oscillations, i.e. EPSPs which are in phase synchrony with the oscillations, which will amplifiy and contribute to the APs.

These findings support the idea that FS-PV INs during SPW-R activities switch to an excited state where regenerative, active dendritic properties can exist. These intrinsic properties of the cells have an effect on the SPW-R generation at a level of a dendritic segment. These data challenge the classical view of the dendritic and cellular properties of FS-PV INs, which held the paradigm that these neurons are passive and provide fast integration in these oscillatory circuits by suppressing regenerative activities in their dendrites.

DOI:10.14753/SE.2015.2055

Összefoglalás

A hippokampális gyorstüzelő, parvalbumin tartalmú interneuronok (FS-PV IN) jelentős szerepet játszanak az agyi információ feldolgozásában, a sejtek aktivitásának szinkronizációjában éles hullámok alatt (SPW-R). Újonnan kifejlesztett 3D két-foton mikroszkópiai technikával és új uncaged glutamát molekulával a jelen tudományos munkámban a korábban leírt tulajdonságokat egészítem ki, miszerint ezek a sejtek képesek egy passzív állapotból aktív állapotba kerülni, ahol a dendritikus szublineáris jelfeldolgozás és a sejtek kimeneti jelei megváltoznak.

Az akciós potenciálhoz (AP) kapcsolt Ca^{2+} jelek nem korlátozódnak a szóma közeli dendritekhez FS-PV IN-ban, hanem a távoli nyúlványokban is megjelennek SPW-R aktivitás alatt.

A sejt passzív, alap állapotával ellentétben, az aktív állapotban léteznek aktívan terjedő Ca^{2+} regeneratív folyamatok (Ca^{2+} spike) a távoli dendriteken. Aktív állapotban a FS-PV IN dendritjeiben a jelfeldolgozás főleg szupralineáris, nem szublineáris. A dendrit két irányába szétterjedő, Ca^{2+} spike-okat meghatározott mintázatban ideérkező aktív bemenetek hoznak létre SPW-R alatt. A dendritikus Ca^{2+} spike-ok kísérleteinkben összefüggésben álltak a Na^{+} csatorna-függő magas frekvenciás membrán potenciál oszcillációval, amelyet ’interneuronális ripple oszcillációnak’ neveztünk el. Ezek fiziológiai tulajdonságaiban megegyeztek az éles hullámok alatt elvezetett ripple aktivitásokkal. A szomatikus AP-k kisülései fáziskapcsoltak az interneuronális ripple aktivitással, amely meghatározza a sejtek kimeneteli jeleit gyors, szubmilliszekundumos időablakban.

A legkisebb funkcionális egység, amely képes ripple frekvencia tartományban oszcillációt kialakítani a FS-PV IN-ban az egy szegmense a dendritnek. Az idegsejt hálózat állapota és a dendritikus folyamatok szabályozása reciprok kapcsolatot mutat: az aktív hálózat képes dinamikusan változtatni a dendritikus jelfeldolgozás természetét, ugyanakkor a változó dendritikus dinamika szinkronizálja az idegsejtek aktivitását az oszcilláló hálózatban.

DOI:10.14753/SE.2015.2055

Summary

Hippocampal fast-spiking, parvalbumin-expressing interneurons (FS-PV INs) play important roles in synchronized oscillations and information processing during SPW-R activities. Using recently developed fast, 3D two-photon microscopy and a novel glutamate-uncaging material, I hereby challenge the classical view by demonstrating that FS-PV INs can implement a dynamic switch in the mode of dendritic integration and output generation from the ground state of passive, sublinear integration to an active state during SPW-Rs.

I found that AP-associated Ca^{2+} responses are not compartmentalized to the proximal dendritic regions in FS-PV INs but also invade distal dendritic segments during SPW-Rs.

Dendritic spikes occur, in contrast to the low-activity baseline state. In the active state, dendritic integration is supralinear and Ca^{2+} spikes are generated. These Ca^{2+} spikes originate from multiple dendritic hot-spots, propagate both centripetally and centrifugally. Notably, Ca^{2+} spikes are associated with membrane potential oscillations, which we call ‘interneuronal ripple oscillations’. The interneuronal ripple oscillations are Na^{+} channel-mediated and have the same frequency as field potential oscillations associated with SPW-Rs. The appearance of interneuronal ripple oscillations interferes with the fast, submillisecond input-output integration of FS-PV INs by coupling AP outputs to the phase of the interneuronal ripple oscillations.

According to our data, the smallest functional unit that can generate ripple-frequency oscillations in the brain is a short segment of a dendrite. These results indicate that neuronal network states and dendritic integration rules show a reciprocal interaction: active network states can dynamically change the nature of dendritic integration rules and, conversely, the altered dendritic dynamics can synchronize the neurons of the oscillating network.

Bibliography

Abrahamsson T, Cathala L, Matsui K, Shigemoto R, Digregorio DA (2012) Thin dendrites of cerebellar interneurons confer sublinear synaptic integration and a gradient of short-term plasticity. Neuron 73:1159-1172.

Ali AB, Deuchars J, Pawelzik H, Thomson AM (1998) CA1 pyramidal to basket and bistratified cell EPSPs: dual intracellular recordings in rat hippocampal slices. J Physiol 507 (Pt 1):201-217.

Andersen PM, R; Amaral, D; Bliss, T; O'Keefe, J (2006) The Hippocampus Book.

Aponte Y, Bischofberger J, Jonas P (2008) Efficient Ca2+ buffering in fast-spiking basket cells of rat hippocampus. J Physiol 586:2061-2075.

Ariav G, Polsky A, Schiller J (2003) Submillisecond precision of the input-output transformation function mediated by fast sodium dendritic spikes in basal dendrites of CA1 pyramidal neurons. J Neurosci 23:7750-7758.

Ascoli GA, Alonso-Nanclares L, Anderson SA, Barrionuevo G, Benavides-Piccione R, Burkhalter A, Buzsaki G, Cauli B, Defelipe J, Fairen A, Feldmeyer D, Fishell G, Fregnac Y, Freund TF, Gardner D, Gardner EP, Goldberg JH, Helmstaedter M, Hestrin S, Karube F, Kisvarday ZF, Lambolez B, Lewis DA, Marin O, Markram H, Munoz A, Packer A, Petersen CC, Rockland KS, Rossier J, Rudy B, Somogyi P, Staiger JF, Tamas G, Thomson AM, Toledo-Rodriguez M, Wang Y, West DC, Yuste R (2008) Petilla terminology: nomenclature of features of GABAergic interneurons of the cerebral cortex. Nat Rev Neurosci 9:557-568.

Avermann M, Tomm C, Mateo C, Gerstner W, Petersen CC (2012) Microcircuits of excitatory and inhibitory neurons in layer 2/3 of mouse barrel cortex. J Neurophysiol 107:3116-3134.

Bahner F, Weiss EK, Birke G, Maier N, Schmitz D, Rudolph U, Frotscher M, Traub RD, Both M, Draguhn A (2011) Cellular correlate of assembly formation in oscillating hippocampal networks in vitro. Proc Natl Acad Sci U S A 108:E607-616.

Bezaire MJ, Soltesz I (2013) Quantitative assessment of CA1 local circuits: knowledge base for interneuron-pyramidal cell connectivity. Hippocampus 23:751-785.

Both M, Bahner F, von Bohlen und Halbach O, Draguhn A (2008) Propagation of specific network patterns through the mouse hippocampus. Hippocampus 18:899-908.

Brunel N, Hakim V (1999) Fast global oscillations in networks of integrate-and-fire neurons with low firing rates. Neural Comput 11:1621-1671.

Buhl EH, Han ZS, Lorinczi Z, Stezhka VV, Karnup SV, Somogyi P (1994) Physiological properties of anatomically identified axo-axonic cells in the rat hippocampus. J Neurophysiol 71:1289-1307.

Buhl EH, Szilagyi T, Halasy K, Somogyi P (1996) Physiological properties of anatomically identified basket and bistratified cells in the CA1 area of the rat hippocampus in vitro. Hippocampus 6:294-305.

Buzsaki G (1986) Hippocampal sharp waves: their origin and significance. Brain Res 398:242-252.

Buzsaki G (1989) Two-stage model of memory trace formation: a role for "noisy" brain states. Neuroscience 31:551-570.

Buzsaki G (2010) Neural syntax: cell assemblies, synapsembles, and readers. Neuron 68:362-385.

Buzsáki G (2006) Rhythms of the brain. New York: Oxford Univ. Press.

Buzsaki G, Chrobak JJ (1995) Temporal structure in spatially organized neuronal ensembles: a role for interneuronal networks. Curr Opin Neurobiol 5:504-510.

Buzsaki G, Diba K (2010) Oscillation-supported Information Processing and Transfer at the Hippocampus–Entorhinal–Neocortical Interface. In: Dynamic Coordination in the Brain: From Neurons to Mind, vol. 5 (Christoph von von der Malsburg, W. A. P., Wolf Singer, ed), pp 101-113 Cambridge: MA: The MIT Press.

Buzsaki G, Horvath Z, Urioste R, Hetke J, Wise K (1992) High-frequency network oscillation in the hippocampus. Science 256:1025-1027.

Buzsaki G, Silva FL (2012) High frequency oscillations in the intact brain. Prog Neurobiol 98:241-249.

Cajal Ry (1909) Histologie du système nerveux de l'homme & des vertébrés. A Maloine, Paris.

Camire O, Topolnik L (2014) Dendritic calcium nonlinearities switch the direction of synaptic plasticity in fast-spiking interneurons. J Neurosci 34:3864-3877.

Carnevale TH, M. (2006) The NEURON Book. vol. 7.1 Cambridge: Cambridge University Press.

Celio MR (1986) Parvalbumin in most gamma-aminobutyric acid-containing neurons of the rat cerebral cortex. Science 231:995-997.

Csicsvari J, Hirase H, Czurko A, Mamiya A, Buzsaki G (1999) Oscillatory coupling of hippocampal pyramidal cells and interneurons in the behaving Rat. J Neurosci 19:274-287.

Csicsvari J, Hirase H, Mamiya A, Buzsaki G (2000) Ensemble patterns of hippocampal CA3-CA1 neurons during sharp wave-associated population events. Neuron 28:585-594.

de Almeida L, Idiart M, Lisman JE (2009) A second function of gamma frequency oscillations: an E%-max winner-take-all mechanism selects which cells fire. J Neurosci 29:7497-7503.

de la Prida LM, Huberfeld G, Cohen I, Miles R (2006) Threshold behavior in the initiation of hippocampal population bursts. Neuron 49:131-142.

Diba K, Buzsaki G (2007) Forward and reverse hippocampal place-cell sequences during ripples. Nat Neurosci 10:1241-1242.

Draguhn A, Traub RD, Schmitz D, Jefferys JG (1998) Electrical coupling underlies high-frequency oscillations in the hippocampus in vitro. Nature 394:189-192.

Eggermann E, Jonas P (2012) How the 'slow' Ca(2+) buffer parvalbumin affects transmitter release in nanodomain-coupling regimes. Nat Neurosci 15:20-22.

Ego-Stengel V, Wilson MA (2010) Disruption of ripple-associated hippocampal activity during rest impairs spatial learning in the rat. Hippocampus 20:1-10.

Ellender TJ, Nissen W, Colgin LL, Mann EO, Paulsen O (2010) Priming of hippocampal population bursts by individual perisomatic-targeting interneurons. J Neurosci 30:5979-5991.

English DF, Peyrache A, Stark E, Roux L, Vallentin D, Long MA, Buzsaki G (2014) Excitation and Inhibition Compete to Control Spiking during Hippocampal Ripples: Intracellular Study in Behaving Mice. J Neurosci 34:16509-16517.

Foffani G, Uzcategui YG, Gal B, Menendez de la Prida L (2007) Reduced spike-timing reliability correlates with the emergence of fast ripples in the rat epileptic hippocampus. Neuron 55:930-941.

Freund TF, Buzsaki G (1996) Interneurons of the hippocampus. Hippocampus 6:347-470.

Freund TF, Katona I (2007) Perisomatic inhibition. Neuron 56:33-42.

Fricker D, Miles R (2000) EPSP amplification and the precision of spike timing in hippocampal neurons. Neuron 28:559-569.

Gasparini S, Migliore M, Magee JC (2004) On the initiation and propagation of dendritic spikes in CA1 pyramidal neurons. J Neurosci 24:11046-11056.

Geiger JR, Lubke J, Roth A, Frotscher M, Jonas P (1997) Submillisecond AMPA receptor-mediated signaling at a principal neuron-interneuron synapse. Neuron 18:1009-1023.

Geisler C, Brunel N, Wang XJ (2005) Contributions of intrinsic membrane dynamics to fast network oscillations with irregular neuronal discharges. J Neurophysiol 94:4344-4361.

Girardeau G, Benchenane K, Wiener SI, Buzsaki G, Zugaro MB (2009) Selective suppression of hippocampal ripples impairs spatial memory. Nat Neurosci 12:1222-1223.

Glickfeld LL, Scanziani M (2006) Distinct timing in the activity of cannabinoid-sensitive and cannabinoid-insensitive basket cells. Nat Neurosci 9:807-815.

Gloveli T, Dugladze T, Saha S, Monyer H, Heinemann U, Traub RD, Whittington MA, Buhl EH (2005) Differential involvement of oriens/pyramidale interneurones in hippocampal network oscillations in vitro. J Physiol 562:131-147.

Goldberg JH, Tamas G, Aronov D, Yuste R (2003a) Calcium microdomains in aspiny dendrites. Neuron 40:807-821.

Goldberg JH, Tamas G, Yuste R (2003b) Ca2+ imaging of mouse neocortical interneurone dendrites: Ia-type K+ channels control action potential backpropagation. J Physiol 551:49-65.

Goldberg JH, Yuste R (2005) Space matters: local and global dendritic Ca2+ compartmentalization in cortical interneurons. Trends Neurosci 28:158-167.

Goldberg JH, Yuste R, Tamas G (2003c) Ca2+ imaging of mouse neocortical interneurone dendrites: contribution of Ca2+-permeable AMPA and NMDA receptors to subthreshold Ca2+dynamics. J Physiol 551:67-78.

Golding NL, Jung HY, Mickus T, Spruston N (1999) Dendritic calcium spike initiation and repolarization are controlled by distinct potassium channel subtypes in CA1 pyramidal neurons. J Neurosci 19:8789-8798.

Golding NL, Spruston N (1998) Dendritic sodium spikes are variable triggers of axonal action potentials in hippocampal CA1 pyramidal neurons. Neuron 21:1189-1200.

Golding NL, Staff NP, Spruston N (2002) Dendritic spikes as a mechanism for cooperative long-term potentiation. Nature 418:326-331.

Gulyas AI, Megias M, Emri Z, Freund TF (1999) Total number and ratio of excitatory and inhibitory synapses converging onto single interneurons of different types in the CA1 area of the rat hippocampus. J Neurosci 19:10082-10097.

Gulyas AI, Miles R, Sik A, Toth K, Tamamaki N, Freund TF (1993) Hippocampal pyramidal cells excite inhibitory neurons through a single release site. Nature 366:683-687.

Hafting T, Fyhn M, Molden S, Moser MB, Moser EI (2005) Microstructure of a spatial map in the entorhinal cortex. Nature 436:801-806.

Hajos N, Ellender TJ, Zemankovics R, Mann EO, Exley R, Cragg SJ, Freund TF, Paulsen O (2009) Maintaining network activity in submerged hippocampal slices: importance of oxygen supply. Eur J Neurosci 29:319-327.

Hajos N, Karlocai MR, Nemeth B, Ulbert I, Monyer H, Szabo G, Erdelyi F, Freund TF, Gulyas AI (2013) Input-output features of anatomically identified CA3 neurons during hippocampal sharp wave/ripple oscillation in vitro. J Neurosci 33:11677-11691.

Hartwich K, Pollak T, Klausberger T (2009) Distinct firing patterns of identified basket and dendrite-targeting interneurons in the prefrontal cortex during hippocampal theta and local spindle oscillations. J Neurosci 29:9563-9574.

Hebb DO (1949) The organization of behavior. New York: Wiley & Sons.

Hefft S, Jonas P (2005) Asynchronous GABA release generates long-lasting inhibition at a hippocampal interneuron-principal neuron synapse. Nat Neurosci 8:1319-1328.

Hu H, Gan J, Jonas P (2014) Interneurons. Fast-spiking, parvalbumin(+) GABAergic interneurons: from cellular design to microcircuit function. Science 345:1255263.

Hu H, Martina M, Jonas P (2010) Dendritic mechanisms underlying rapid synaptic activation of fast-spiking hippocampal interneurons. Science 327:52-58.

Hu H, Vervaeke K, Graham LJ, Storm JF (2009) Complementary theta resonance filtering by two spatially segregated mechanisms in CA1 hippocampal pyramidal neurons. J Neurosci 29:14472-14483.

Isomura Y, Sirota A, Ozen S, Montgomery S, Mizuseki K, Henze DA, Buzsaki G (2006) Integration and segregation of activity in entorhinal-hippocampal subregions by neocortical slow oscillations. Neuron 52:871-882.

Jadhav SP, Kemere C, German PW, Frank LM (2012) Awake hippocampal sharp-wave ripples support spatial memory. Science 336:1454-1458.

Jefferys JG, Menendez de la Prida L, Wendling F, Bragin A, Avoli M, Timofeev I, Lopes da Silva FH (2012) Mechanisms of physiological and epileptic HFO generation. Prog Neurobiol 98:250-264.

Ji N, Magee JC, Betzig E (2008) High-speed, low-photodamage nonlinear imaging using passive pulse splitters. Nat Methods 5:197-202.

Johnston D, Narayanan R (2008) Active dendrites: colorful wings of the mysterious butterflies. Trends Neurosci 31:309-316.

Kamondi A, Acsady L, Buzsaki G (1998) Dendritic spikes are enhanced by cooperative network activity in the intact hippocampus. J Neurosci 18:3919-3928.

Kandel ER, Schwartz, J.H. and Jessel, T.M. (1991) Principles of Neural Science. Elsevier, New York.

Katona G, Kaszas A, Turi GF, Hajos N, Tamas G, Vizi ES, Rozsa B (2011) Roller Coaster Scanning reveals spontaneous triggering of dendritic spikes in CA1 interneurons. Proc Natl Acad Sci U S A 108:2148-2153.

Katona G, Szalay G, Maak P, Kaszas A, Veress M, Hillier D, Chiovini B, Vizi ES, Roska B, Rozsa B (2012) Fast two-photon in vivo imaging with three-dimensional random-access scanning in large tissue volumes. Nat Methods 9:201-208.

Klausberger T, Magill PJ, Marton LF, Roberts JD, Cobden PM, Buzsaki G, Somogyi P (2003) Brain-state- and cell-type-specific firing of hippocampal interneurons in vivo. Nature 421:844-848.

Klausberger T, Somogyi P (2008) Neuronal diversity and temporal dynamics: the unity of hippocampal circuit operations. Science 321:53-57.

Kleindienst T, Winnubst J, Roth-Alpermann C, Bonhoeffer T, Lohmann C (2011) Activity-dependent clustering of functional synaptic inputs on developing hippocampal dendrites. Neuron 72:1012-1024.

Lamsa KP, Heeroma JH, Somogyi P, Rusakov DA, Kullmann DM (2007) Anti-Hebbian long-term potentiation in the hippocampal feedback inhibitory circuit. Science 315:1262-1266.

Lapray D, Lasztoczi B, Lagler M, Viney TJ, Katona L, Valenti O, Hartwich K, Borhegyi Z, Somogyi P, Klausberger T (2012) Behavior-dependent specialization of identified hippocampal interneurons. Nat Neurosci 15:1265-1271.

Larkum ME, Nevian T, Sandler M, Polsky A, Schiller J (2009) Synaptic integration in tuft dendrites of layer 5 pyramidal neurons: a new unifying principle. Science 325:756-760.

Larkum ME, Zhu JJ, Sakmann B (1999) A new cellular mechanism for coupling inputs arriving at different cortical layers. Nature 398:338-341.

Lee SH, Marchionni I, Bezaire M, Varga C, Danielson N, Lovett-Barron M, Losonczy A, Soltesz I (2014) Parvalbumin-positive basket cells differentiate among hippocampal pyramidal cells. Neuron 82:1129-1144.

Leutgeb JK, Leutgeb S, Moser MB, Moser EI (2007) Pattern separation in the dentate gyrus and CA3 of the hippocampus. Science 315:961-966.

Llinas R, Nicholson C, Freeman JA, Hillman DE (1968) Dendritic spikes and their inhibition in alligator Purkinje cells. Science 160:1132-1135.

Llinas R, Sugimori M (1980) Electrophysiological properties of in vitro Purkinje cell somata in mammalian cerebellar slices. J Physiol 305:171-195.

Logothetis NK, Eschenko O, Murayama Y, Augath M, Steudel T, Evrard HC, Besserve M, Oeltermann A (2012) Hippocampal-cortical interaction during periods of subcortical silence. Nature 491:547-553.

Lømo T (1966) Frequency potentiation of excitatory synaptic activity in the dentate area of the hippocampal formation. Acta Physiologica Scandinavica 68.

Lorenz A, Osman F, Sun W, Nandi S, Steinacher R, Whitby MC (2012) The fission yeast FANCM ortholog directs non-crossover recombination during meiosis. Science 336:1585-1588.

Lorincz A, Nusser Z (2008) Cell-type-dependent molecular composition of the axon initial segment. J Neurosci 28:14329-14340.

Losonczy A, Magee JC (2006) Integrative properties of radial oblique dendrites in hippocampal CA1 pyramidal neurons. Neuron 50:291-307.

Magee JC, Johnston D (2005) Plasticity of dendritic function. Curr Opin Neurobiol 15:334-342.

Mahut H, Zola-Morgan S, Moss M (1982) Hippocampal resections impair associative learning and recognition memory in the monkey. J Neurosci 2:1214-1220.

Maier N, Nimmrich V, Draguhn A (2003) Cellular and network mechanisms underlying spontaneous sharp wave-ripple complexes in mouse hippocampal slices. J Physiol 550:873-887.

Maier N, Tejero-Cantero A, Dorrn AL, Winterer J, Beed PS, Morris G, Kempter R, Poulet JF, Leibold C, Schmitz D (2011) Coherent phasic excitation during hippocampal ripples. Neuron 72:137-152.

Makino H, Malinow R (2011) Compartmentalized versus global synaptic plasticity on dendrites controlled by experience. Neuron 72:1001-1011.

Maravall M, Mainen ZF, Sabatini BL, Svoboda K (2000) Estimating intracellular calcium concentrations and buffering without wavelength ratioing. Biophys J 78:2655-2667.

Martina M, Vida I, Jonas P (2000) Distal initiation and active propagation of action potentials in interneuron dendrites. Science 287:295-300.

McLachlan GJ, Peel D (2000) Finite Mixture Models.

Memmesheimer RM (2010) Quantitative prediction of intermittent high-frequency oscillations in neural networks with supralinear dendritic interactions. Proc Natl Acad Sci U S A 107:11092-11097.

Meyer AH, Katona I, Blatow M, Rozov A, Monyer H (2002) In vivo labeling of parvalbumin-positive interneurons and analysis of electrical coupling in identified neurons. J Neurosci 22:7055-7064.

Miles R, Toth K, Gulyas AI, Hajos N, Freund TF (1996) Differences between somatic and dendritic inhibition in the hippocampus. Neuron 16:815-823.

Nadasdy Z, Hirase H, Czurko A, Csicsvari J, Buzsaki G (1999) Replay and time compression of recurring spike sequences in the hippocampus. J Neurosci 19:9497-9507.

Narayanan R, Johnston D (2007) Long-term potentiation in rat hippocampal neurons is accompanied by spatially widespread changes in intrinsic oscillatory dynamics and excitability. Neuron 56:1061-1075.

Nimmrich V, Maier N, Schmitz D, Draguhn A (2005) Induced sharp wave-ripple complexes in the absence of synaptic inhibition in mouse hippocampal slices. J Physiol 563:663-670.

Norenberg A, Hu H, Vida I, Bartos M, Jonas P (2010) Distinct nonuniform cable properties optimize rapid and efficient activation of fast-spiking GABAergic interneurons. Proc Natl Acad Sci U S A 107:894-899.

O'Keefe J, Dostrovsky J (1971) The hippocampus as a spatial map. Preliminary evidence from unit activity in the freely-moving rat. Brain Res 34:171-175.

O'Keefe J NL (1978) The hippocampus as a cognitive map. Clarendon Press, Oxford.

Papatheodoropoulos C (2008) A possible role of ectopic action potentials in the in vitro hippocampal sharp wave-ripple complexes. Neuroscience 157:495-501.

Patel J, Schomburg EW, Berenyi A, Fujisawa S, Buzsaki G (2013) Local generation and propagation of ripples along the septotemporal axis of the hippocampus. J Neurosci 33:17029-17041.

Pike FG, Goddard RS, Suckling JM, Ganter P, Kasthuri N, Paulsen O (2000) Distinct frequency preferences of different types of rat hippocampal neurones in response to oscillatory input currents. J Physiol 529 Pt 1:205-213.

Polsky A, Mel BW, Schiller J (2004) Computational subunits in thin dendrites of pyramidal cells. Nat Neurosci 7:621-627.

Pouille F, Scanziani M (2001) Enforcement of temporal fidelity in pyramidal cells by somatic feed-forward inhibition. Science 293:1159-1163.

Pouille F, Scanziani M (2004) Routing of spike series by dynamic circuits in the hippocampus. Nature 429:717-723.

Proctor B, Wise F (1992) Quartz prism sequence for reduction of cubic phase in a mode-locked Ti:Al(2)O(3) laser. Opt Lett 17:1295-1297.

Racz A, Ponomarenko AA, Fuchs EC, Monyer H (2009) Augmented hippocampal ripple oscillations in mice with reduced fast excitation onto parvalbumin-positive cells. J Neurosci 29:2563-2568.

Rall W, Shepherd GM, Reese TS, Brightman MW (1966) Dendrodendritic synaptic pathway for inhibition in the olfactory bulb. Exp Neurol 14:44-56.

Rozsa B, Katona G, Kaszas A, Szipocs R, Vizi ES (2008) Dendritic nicotinic receptors modulate backpropagating action potentials and long-term plasticity of interneurons. Eur J Neurosci 27:364-377.

Rozsa B, Katona G, Vizi ES, Varallyay Z, Saghy A, Valenta L, Maak P, Fekete J, Banyasz A, Szipocs R (2007) Random access three-dimensional two-photon microscopy. Appl Opt 46:1860-1865.

Rozsa B, Zelles T, Vizi ES, Lendvai B (2004) Distance-dependent scaling of calcium transients evoked by backpropagating spikes and synaptic activity in dendrites of hippocampal interneurons. J Neurosci 24:661-670.

Rudy B, McBain CJ (2001) Kv3 channels: voltage-gated K+ channels designed for high-frequency repetitive firing. Trends Neurosci 24:517-526.

Schiller J, Major G, Koester HJ, Schiller Y (2000) NMDA spikes in basal dendrites of cortical pyramidal neurons. Nature 404:285-289.

Schiller J, Schiller Y, Stuart G, Sakmann B (1997) Calcium action potentials restricted to distal apical dendrites of rat neocortical pyramidal neurons. J Physiol 505 (Pt 3):605-616.

Schlingloff D, Kali S, Freund TF, Hajos N, Gulyas AI (2014) Mechanisms of sharp wave initiation and ripple generation. J Neurosci 34:11385-11398.

Schmitz D, Schuchmann S, Fisahn A, Draguhn A, Buhl EH, Petrasch-Parwez E, Dermietzel R, Heinemann U, Traub RD (2001) Axo-axonal coupling. a novel mechanism for ultrafast neuronal communication. Neuron 31:831-840.

Schonberger J, Draguhn A, Both M (2014) Lamina-specific contribution of glutamatergic and GABAergic potentials to hippocampal sharp wave-ripple complexes. Front Neural Circuits 8:103.

Schwarz G (1978) Estimating the Dimension of a Model. Annals of Statistics 6:461-464.

Sirota A, Csicsvari J, Buhl D, Buzsaki G (2003) Communication between neocortex and hippocampus during sleep in rodents. Proc Natl Acad Sci U S A 100:2065-2069.

Sohal VS, Zhang F, Yizhar O, Deisseroth K (2009) Parvalbumin neurons and gamma rhythms enhance cortical circuit performance. Nature 459:698-702.

Somogyi P, Katona L, Klausberger T, Lasztoczi B, Viney TJ (2014) Temporal redistribution of inhibition over neuronal subcellular domains underlies state-dependent rhythmic change of excitability in the hippocampus. Philos Trans R Soc Lond B Biol Sci 369:20120518.

Somogyi P, Kisvarday ZF, Martin KA, Whitteridge D (1983) Synaptic connections of morphologically identified and physiologically characterized large basket cells in the striate cortex of cat. Neuroscience 10:261-294.

Squire LR, Stark CE, Clark RE (2004) The medial temporal lobe. Annu Rev Neurosci 27:279-306.

Stark E, Roux L, Eichler R, Senzai Y, Royer S, Buzsaki G (2014) Pyramidal cell-interneuron interactions underlie hippocampal ripple oscillations. Neuron 83:467-480.

Stuart G, Spruston, N., and Hausser, M. (1999) Dendrites. Oxford: Oxford University Press.

Stuart GJ, Sakmann B (1994) Active propagation of somatic action potentials into neocortical pyramidal cell dendrites. Nature 367:69-72.

Sullivan D, Csicsvari J, Mizuseki K, Montgomery S, Diba K, Buzsaki G (2011) Relationships between hippocampal sharp waves, ripples, and fast gamma oscillation: influence of dentate and entorhinal cortical activity. J Neurosci 31:8605-8616.

Takahashi N, Kitamura K, Matsuo N, Mayford M, Kano M, Matsuki N, Ikegaya Y (2012) Locally synchronized synaptic inputs. Science 335:353-356.

Taxidis J, Coombes S, Mason R, Owen MR (2012) Modeling sharp wave-ripple complexes through a CA3-CA1 network model with chemical synapses. Hippocampus 22:995-1017.

Topolnik L (2012) Dendritic calcium mechanisms and long-term potentiation in cortical inhibitory interneurons. Eur J Neurosci 35:496-506.

Traub RD, Bibbig A (2000) A model of high-frequency ripples in the hippocampus based on synaptic coupling plus axon-axon gap junctions between pyramidal neurons. J Neurosci 20:2086-2093.

Traub RD, Schmitz D, Maier N, Whittington MA, Draguhn A (2012) Axonal properties determine somatic firing in a model of in vitro CA1 hippocampal sharp wave/ripples and persistent gamma oscillations. Eur J Neurosci 36:2650-2660.

Traub RD, Whittington MA, Stanford IM, Jefferys JG (1996) A mechanism for generation of long-range synchronous fast oscillations in the cortex. Nature 383:621-624.

Tukker JJ, Lasztoczi B, Katona L, Roberts JD, Pissadaki EK, Dalezios Y, Marton L, Zhang L, Klausberger T, Somogyi P (2013) Distinct dendritic arborization and in vivo firing patterns of parvalbumin-expressing basket cells in the hippocampal area CA3. J Neurosci 33:6809-6825.

Varga C, Golshani P, Soltesz I (2012) Frequency-invariant temporal ordering of interneuronal discharges during hippocampal oscillations in awake mice. Proc Natl Acad Sci U S A 109:E2726-2734.

Vervaeke K, Lorincz A, Nusser Z, Silver RA (2012) Gap junctions compensate for sublinear dendritic integration in an inhibitory network. Science 335:1624-1628.

Vinet J, Sik A (2006) Expression pattern of voltage-dependent calcium channel subunits in hippocampal inhibitory neurons in mice. Neuroscience 143:189-212.

Waters J, Larkum M, Sakmann B, Helmchen F (2003) Supralinear Ca2+ influx into dendritic tufts of layer 2/3 neocortical pyramidal neurons in vitro and in vivo. J Neurosci 23:8558-8567.

Whittington MA, Traub RD, Jefferys JG (1995) Synchronized oscillations in interneuron networks driven by metabotropic glutamate receptor activation. Nature 373:612-615.

Wilson MA, McNaughton BL (1994) Reactivation of hippocampal ensemble memories during sleep. Science 265:676-679.

Ylinen A, Bragin A, Nadasdy Z, Jando G, Szabo I, Sik A, Buzsaki G (1995) Sharp wave-associated high-frequency oscillation (200 Hz) in the intact hippocampus: network and intracellular mechanisms. J Neurosci 15:30-46.

Zaitsev AV, Povysheva NV, Lewis DA, Krimer LS (2007) P/Q-type, but not N-type, calcium channels mediate GABA release from fast-spiking interneurons to pyramidal cells in rat prefrontal cortex. J Neurophysiol 97:3567-3573.

Zemankovics R, Kali S, Paulsen O, Freund TF, Hajos N (2010) Differences in subthreshold resonance of hippocampal pyramidal cells and interneurons: the role of h-current and passive membrane characteristics. J Physiol 588:2109-2132.

DOI:10.14753/SE.2015.2055

List of the Author's Publication

Publications related to thesis

Chiovini B*, Turi GF*, Katona G, Kaszás A, Pálfi D, Maák P, Szalay G, Szabó MF, Szabó G, Szadai Z, Káli S, Rózsa B (2014) Dendritic spikes induce ripples in PV interneurons during hippocampal sharp waves. Neuron 21;82(4):908-24.
* *These authors contributed equally to this work.*

Chiovini B, Turi GF, Katona G, Kaszás A, Erdélyi F, Szabó G, Monyer H, Csákányi A, Vizi ES, Rózsa B (2010) Enhanced dendritic AP backpropagation in PV-positive basket cells during sharp wave activity. Neurochem Res 35(12):2086-95.

Other publications

Katona G*, Szalay G*, Maák P*, Kaszás A*, Veress M, Hillier D, Chiovini B, Vizi ES, Roska B, Rózsa B (2012) Fast two-photon in vivo imaging with three-dimensional random-access scanning in large tissue volumes. Nat Methods 8;9(2):201-8.
* *These authors contributed equally to this work.*

Kerekes PB, Tóth K, Kaszás A, Chiovini B, Szadai Z, Szalay G, Pálfi D, Bagó A, Spitzer K, Rózsa B, Ulbert I, Wittner L (2014) Combined two-photon imaging, electrophysiological, and anatomical investigation of the human neocortex in vitro Neurophoton 1(1): 011013

Patents

Csizmadia IGy, Mucsi Z, Szalay G, Kaszás A, Lukácsné Haveland Cs, Majercsik O, Potor A, Katona G, Rózsa B, Gündisch D, Chiovini B, Pálfi D. Use of Photocleavable compounds. WO2012HU00100 20121003

Csizmadia IGy, Rozsa JB, Mucsi Z, Lukácsné Haveland Cs, Katona G, Majercsik O, Potor A, Kaszas A, Gündisch D, Chiovini B, Szalay G, Palfi D. Use of Photocehmically celavable compounds HU20120000574 20121003

Rozsa B, Katona G, Veress M, Maak P, Szalay G, Kaszas A, Chiovini B, Matyas P. Method for scanning along a continous scanning trajectory with a scanner system WO2012HU00001 20120105

DOI:10.14753/SE.2015.2055

Appendix Movie Legends

Movie 1. 3D acousto-optical scanning of an FS-PV IN dendrite reveals dendritic spikes during SPW-Rs (related to **Figures 18 and 19**). This movie shows a single 3D recording of Ca^{2+} signals at multiple dendritic sites, which is also used in **Figures 18 and 19**. The corresponding somatic membrane potential (green) and LFP signal (red) are shown at the bottom. Spheres represent the 98 pre-selected locations scanned in 3D with a 301 Hz repetition rate, and their color and size varies with the change in relative fluorescence ($\Delta F/F$). Three SPW-R-associated somatically subthreshold events (SPW-EPSPs) and two suprathreshold events (SPW-APs) spontaneously occurred during the 7 s total measurement period. Time is slowed down by a factor of two for clarity.

Movie 2. 3D acousto-optical scanning of a bAP event (related to **Figures 18-21**). This movie shows five bAP-induced Ca^{2+} signals recorded in the same 98 pre-selected dendritic locations as in **Movie 1**. The AP event is marked with a white diamond. Note the reciprocal pattern in the spatial distribution of Ca^{2+} signals compared to the SPW-EPSP (**Movie 4**) and SPW-AP (**Movie 3**) events.

Movie 3. 3D acousto-optical scanning of an SPW-AP event (related to **Figures 18-21**). This movie shows a temporal expansion of the sixth event shown in Movie 1. The incoming SPW-AP event is marked with a white diamond.

Movie 4. 3D acousto-optical scanning of an SPW-EPSP event (related to **Figures 18-21**). This movie shows a temporal expansion of the first event shown in **Movie 1**. The incoming SPW-EPSP event is marked with a white diamond.

DOI:10.14753/SE.2015.2055

Author Contribution

Optical design was performed by Pál Maák, Gergely Szalay, and Balázs Rózsa. Software was written by Gergely Katona. *In vitro* measurements were performed by **Balázs Chiovini (~67%)**, Gergely F. Turi, Dénes Pálfi, Zoltán Szaday and Attila Kaszás. Analysis was carried out by **Balázs Chiovini (~67%),** Balázs Rózsa, Gergely F. Turi, and Dénes Pálfi. Animals were provided by Gábor Szabó. Caged compound was synthesized by Csilla Lukácsné Haveland and Orsolya Frigyesi.

DOI:10.14753/SE.2015.2055

Acknowledgement

First of all, I would like to thank my supervisor, Dr. Balázs J. Rózsa for guiding me through this period of my scientific life. It was a great opportunity to join his group and start to learn two-photon microscopic techniques and patch-clamp methodology. Without his help and instructions I could not have finished my work.

I would also like to thank my collegue, Gergely F. Turi. I could always turn to him with confidence, he always listened carefully and gave me advice and great help like a real supervisor.

I would like to give special thanks to Dénes Pálfi, with whom I have been working for four years and finished my first great project.

My thesis would have been much more disorganized and would have lacked many of the well-placed references without the constructive criticism of Dr. Norbert Hájos, who has thoroughly read my thesis to help in bettering it.

Furthermore, many thanks to my co-authors and my other colleagues in our research group for their friendship and/or for the knowledge and the wonderful time we spent together: Alexandra Bojdán, Attila Kaszás, Csilla Lukácsné Haveland, Dorina Gündisch, Ferenc Csikor, Ferenc Erdélyi, Gábor Szabó, Gergely Katona, Gergely Szalay, Imre Csizmadia, Klaudia Sptizer, Linda Judák, Máté Veress, Miklós Madarász, Orsolya Frigyesi, Pál Maák, Szabolcs Káli, Zoltán Mucsi, Zoltán Szadai and the whole Femtonics group.

And finally, but most importantly, I would like to say thank you to my family, Kata and Konrád for their support and patience that they have shown during this elongated period of our life.

This work was supported by the grants OM-00131/2007, OM-00132/2007, GOP-1.1.1-08/1-2008-0085, NK 72959, Grant of Hungarian Academy of Sciences, French grant (TÉT_0389), Swiss-Hungarian grant SH/7/2/8, KMR_0214, FP7-ICT-2011-C 323945.